UNIVERSIDAD NACIONAL AUTÓNOMA DE MÉXICO
POSGRADO EN CIENCIAS FÍSICAS
INSTITUTO DE CIENCIAS NUCLEARES
ASTROPARTÍCULAS

NEUTRINOS DE ALTAS ENERGÍAS Y SU ORIGEN ASTROFÍSICO

TESIS
QUE PARA OPTAR POR EL GRADO DE
DOCTOR EN CIENCIAS FÍSICAS

PRESENTA:
LUIS SALVADOR MIRANDA PALACIOS

TUTOR O TUTORES PRINCIPALES
DR. SARIRA SAHU (INSTITUTO DE CIENCIAS NUCLEARES)

MIEMBROS DEL COMITÉ TUTOR
DR. SARIRA SAHU (INSTITUTO DE CIENCIAS NUCLEARES, UNAM)
DRA. MYRIAM MONDRAGÓN CEBALLOS (INSTITUTO DE FÍSICA, UNAM)
DR. GENARO TOLEDO SANCHÉZ (INSTITUTO DE FÍSICA, UNAM)

CD. DE MÉXICO, MÉXICO, FEBRERO 2017

UNIVERSIDAD NACIONAL AUTÓNOMA DE MÉXICO

Doctorado en Ciencias (Física)
Instituto de Ciencias Nucleares

Title

High Energy Neutrinos and their Astrophysical Origin

Thesis
to obtain the degree of
Doctor of Philosophy in Science (Physics)

Presents

Luis Salvador Miranda Palacios

Adviser

Dr. Sarira Sahu

Tutorial Committee Members
Dr. Sarira Sahu (ICN, UNAM)
Dra. Myriam Mondragón Ceballos (IF, UNAM)
Dr. Genaro Toledo Sánchez (IF, UNAM)

México City, México, **February 2017**

Acknowledgments

First I would like to thank my adviser, Sarira Sahu, for his constant inspiration, support, honesty and ability to direct me in right direction. My association with him is very fruitful and productive for me. I sincerely thank him for giving me the opportunity to be part of his team. I thank to my father Luis, for all his love, time, ethics and education which made to stand here proudly. I love you "Dad". My love to my mother Lucrecia (you left before), brother Ivan, sister Idum and nephew Kevin for their love, support and all the funny and emotional moments spent with me. I am thankful to my tutorial committee members Dra. Myriam Mondragón Ceballos and Dr. Genaro Toledo Sanchéz for their advices and suggestions. I sincerely thank To Dr. Rafael Pérez Pascual and Esther Hacyan Dultzin for giving me chance to keep going. Thanks to my friends Marisol Rodríguez, Antonio Velázquez, Omar Jesús Franca, Eddie Palacios and Adrián Mauricio Escobar who are my partners in this travel and thanks for all the advices, support, discussions and good food during this long journey. Sincere thanks to my collaborators Alberto Rosales de León for the work involve in this thesis, to Marco Vladimir Lemus Yáñez for collaborating with me and Dr. Subhash Rajpoot for collaborating in the second paper of this work, and the jury of this thesis doctors Manuel Torres Labansat, Omar Gustavo Miranda Romagnoli, Luis Gustavo Cabral Rosetti, Ricardo Gaitán Lozano and my adviser.

Finally I would like to thank CONACYT and PAPIIT (UNAM) (Project No IN110815) for financial support.

Abstract

The IceCube Collaboration has observed 37 neutrino events in the energy range 30TeV$\leq$ $E_\nu \leq$ 2PeV and the sources of these neutrinos are unknown. In our first paper we show that the positions of 12 high energy blazars of the TeVCat catalogue and the position of the FR-I galaxy Centaurus A coincide within the error circles of ten IceCube events, the latter being in the error circle of the highest energy event so far observed by IceCube. In the last work we found that the ANTARES collaboration presented a time dependent analysis of a selected number of flaring blazars to look for upward going muon events produced from the charge current interaction of the muon neutrinos. We use the same list of flaring blazars (of ANTARES) to look for a possible positional correlation with the IceCube neutrino events.

In the context of the photohadronic model we propose that the neutrinos are produced within the nuclear region of the blazar where Fermi accelerated high energy protons interact with the background synchrotron/SSC photons, giving arguments that AGN are probably responsible for some of the observed IceCube events, but the statistical analysis shows that none of these sources have a significant correlation.

The TeV blazar Markarian 421 underwent multi-TeV flaring during April 2004 and simultaneous observations in the X-ray and TeV energies were made. It was observed that the TeV outbursts had no counterparts in the lower energy range. One implication of this is that it might be an orphan flare. We show that Fermi-accelerated protons of energy $\leq$168 TeV can interact with the low energy tail of the background synchrotron self-Compton photons in the inner region of the blazar to produce the multi-TeV flare and our results fit very well with the observed spectrum. Future possible candidates for this scenario are the HBLs Mrk 501 and PG 1553 + 113 objects.

Resumen

La colaboración IceCube ha observado 37 eventos de neutrinos en el rango de energías 30TeV$\leq E_\nu \leq$ 2PeV y las fuentes de estos neutrinos son desconocidas. En nuestro primer artículo nosotros mostramos que las posiciones de 12 blazares de alta energiá del catálogo TeVCat y la posición de la FR-I galaxy Centaurus A coinciden dentro de los errores circulares de diez eventos de IceCube, el último dentro del error circular de el evento de más alta energía jamás observado. En el último trabajo tomamos como base el trabajo de la colaboración ANTARES donde llevaron a cabo un análisis dependiente del tiempo con un nḿuero selecto de blazares; para buscar relación con neutrinos muonicos tipo upward producidos por corrientes cargadas de neutrinos muónicos.

En el contexto de el modelo fotohadrónico nosotros proponemos que los neutrinos producidos dentro de la región nuclear del blazar donde la aceleración de Fermi de protones interactuán con los fotones de background synchrotron/SSC, dando argumentos de que los AGN son probables responsables de algunos de los eventos observados en IceCube, pero el análisis estadístico muestra que ninguna de estas fuentes tiene una correlación significativa.

EL TeV blazar Markarian 421 tuvo una erupción multi-TeV durante abril del 2014, con observaciones simultáneas en los rayos X y TeV. Se observó que la erupción no tuvo contraparte en el rango de bajas energías. Una implicación de esto es que podría ser una erupción huerfána. Nosotros mostramos que la aceleración de Fermi de los protones de energía $\leq$168 TeV pueden interactuar con la cola de energía de los fotones del background synchrotron self-Compton en la región del blazar para producir un flare Multi-TeV y como resultado el modelo ajusta muy bien al espectro observado. Futuros posibles candidatos para este escenario son los HBLs Mrk 501 y PG 1553+113.

Index

Chapter 1

Basics

How can we know information about the astrophysical objects and the processes involved?, What is an Active Galactic Nuclei?, What is the atmospheric background? How can we detect the neutrinos?, and explore the amazing Icecube detector. This chapter has the goal to be an introduction of the astroparticle physics: the messengers of the astrophysical objects, the particle processes involved in this work, an exhaustive description of the Active Galactic Nuclei, Atmospheric background and the IceCube Neutrino Detector. These are the basics for understand the content of the rest of the thesis.

1.1 Cosmic Rays

Particle physics forms a basic framework for far-reaching excursions of the human mind into the structure of matter and of the universe. This physics area will improve the horizon of our understanding further, by pushing the energy limit and the sensitivity limit of the particle accelerators and by interacting more closely with other fields. But increasing the energy limit and the sensitivity of the accelerators depends on the modern technology, which is not always feasible to go for such requirements. On the other hand "heavenly laboratories" are complementary to accelerator and non-accelerator experiments, which are much more powerful. By now, Particle astrophysics (or astroparticle physics) which is a fusion of particle physics and astrophysics has been one of the most successful fields out of many multidisciplinary ventures and presents to particle physics extraordinary opportunities. Astrophysical and cosmological arguments and observations have become part of the main-stream methodology to obtain information on existing or hypothetical

elementary particles, their interactions and the observable effects produced by them. The marriage of particle physics and astrophysics is even more intimate, when it comes to instrumentation: for example, the construction of dark matter detectors, Earth- and space-based gamma ray telescopes, underground giant neutrino detectors and state-of-the-art air shower detectors. All these are full of technology developed for accelerator experiments. The search for the particle nature of the dark matter, neutrino mass and the look for the origin of the ultra high energy cosmic rays are few examples of many common intellectual endeavors of particle physics and particle astrophysics which can be probed in non-accelerator experiments using heavenly laboratories as sources. Doing particle physics beyond the boundaries of the accelerator laboratories, for instance, in space, at South Pole, deep sea, under ground, under ice or in the desert, will inspire future generations of scientists and the public at large. It is needless to say that, astroparticle physics is and will be the frontline area of research in the coming years.

The Cosmic Rays are heavenly messengers to study the astrophysical objects as well as high energy phenomena which is impossible to achieve in terristerial experiments. The cosmic rays consist of charged particles mainly protons and nucleus and were discovered by Victor Hess via a series of ballon experiments in 1911 [1]. These experiments showed that the rate of radiation increases as we go higher in altitude, meaning that the origin of the radiation is extraterrestrial. Their spectrum extends over 11 orders of magnitude and follows approximately a single power-law as $E^{-2.7}$ [2]. A break around energy 3×10^6 GeV is referred as the knee and a spectral hardening at energy $\sim 10^9$ eV is known as the ankle. These breaks are explained due to change in the composition and origin of cosmic rays. At energies above the knee the gyroradius of the proton is larger than the size of the Galaxy, creating a softer spectrum as higher energy particles are more likely to escape. So the shape of the knee is likely caused by a change in composition towards heavier nuclei, since higher charged particles require higher energies to escape. For energies above the ankle, Galactic sources are not believed to have the required magnetic field strength and size to accelerate the cosmic rays. A final spectral cutoff occurs at $\sim 4 \times 10^{19}$ eV and is supposed to be evidence of the Greisen-Zatsepin-Kuzmin (GZK) mechanism, in which cosmic rays are absorbed on cosmic microwave background (CMB) photons via the Δ resonance. This energy loss process limits the propagation of high-energy protons to ~ 50 Mpc (the GZK Horizon) [3]. A graph of the flux is showed in fig.(1.1). The mechanism of production and propagation as well as the source of high to very high energy cosmic

rays are not understood well and are subject of current research.

It is believed that these particles are accelerated by the Fermi mechanism [4]. In this scenario particles bounce back and forth across a shock or a cloud as it expands, gaining energy with each crossing. Assuming that the particles gain a fractional amount of energy with each crossing and escape from the shock probabilistically, this particle follows a power law spectrum. In strong shocks, where the shock speed is much faster than the speed of the sound in the medium, an E^{-2} energy spectrum is predicted. If this process happens for enough time to reach the necessary energy, for a source of size R and magnetic field strength B, it can accelerate a particle with charge Z to a maximum energy E_{max}, given by [5]

$$E_{max} \sim 10^{18} eV \beta_S Z \left(\frac{B}{\mu G}\right)\left(\frac{R}{kpc}\right), \tag{1.1}$$

where β_S is the relative velocity of the shock wave with respect to the speed of light.

1.2 High Energy Messengers

Charged cosmic rays (protons, nucleus etc.) are deflected by the magnetic fields on their way to Earth. So their arrival directions are expected to be randomized due to inter-galactic and Galactic magnetic fields. However, at higher energies, the deflection in the magnetic field is very small (only a few degrees). Cosmic rays interact with background matter or radiation within the source or outside the source to produce secondary particles mostly charged and neutral pions. Decay of neutral pions produce gamma rays and the neutrinos are produced from the decay of charged pions. So the principal messengers of the astrophysical sources are the **cosmic rays, photons and neutrinos**.

As mentioned above, while cosmic rays are deflected by magnetic fields and the high energy photons are absorbed by the extragalactic background light (EBL) to produce electron positron pairs, neutrinos are the only heavenly messengers that come straight from the production point to the detector, which is why neutrinos are considered as ideal cosmic messengers.

The processes through which the high energy cosmic ray (mostly proton) interact with the background photons and hydrogen cloud are given as

$$p\gamma \longrightarrow \Delta^+ \longrightarrow \begin{cases} p + \pi^0 \\ n + \pi^+ \end{cases}, \tag{1.2}$$

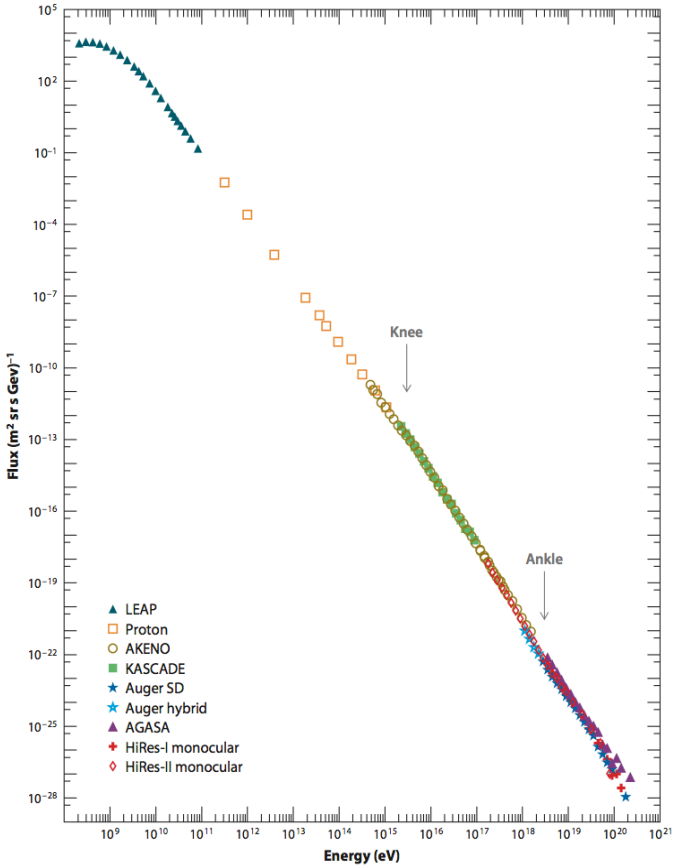

Figure 1.1: Cosmic Ray Flux taken of [2]

$$pp \longrightarrow \begin{cases} p + p + \pi^0 \\ p + n + \pi^+ \end{cases} . \tag{1.3}$$

For $n\gamma$ or pn interactions, π^- particles are created instead of π^+. Successively the decay of charged and neutral pions decay are given as

$$\begin{aligned} \pi^+ \longrightarrow \quad & \mu^+ + \nu_\mu \\ & \mu^+ \longrightarrow e^+ + \nu_e + \bar{\nu}_\mu, \end{aligned} \tag{1.4}$$

$$\begin{aligned} \pi^- \longrightarrow \quad & \mu^- + \bar{\nu}_\mu \\ & \mu^- \longrightarrow e^- + \bar{\nu}_e + \nu_\mu. \end{aligned} \tag{1.5}$$

$$\pi^0 \longrightarrow \gamma\gamma. \tag{1.6}$$

In the decay $\pi^{\pm}$, the secondary neutrino has energy $E_\nu \sim 1/4E_\pi \sim 1/20E_p$ and the photon has energy $E_\gamma \sim 1/2E_\pi \sim 1/10E_p$, where E_p is the energy of the cosmic ray. Counting neutrino and antineutrino flavors in the final state results in a flavor ratio at the source: $\nu_e : \nu_\mu : \nu_\tau = 1 : 2 : 0$. However, due to neutrino oscillation, the resulting flavor ratio on Earth is: $\nu_e : \nu_\mu : \nu_\tau = 1 : 1 : 1$. Detection of these neutrinos and photons are signatures of hadronic CRs, since there is no equivalent leptonic processes to produce these high energy counter parts.

1.3 Atmospheric Background

The Earth's atmosphere is continuously bombarded by high energy cosmic rays which interact with the air molecules generating secondary particles: pions, kaons and charmed mesons that finally produce electrons, positrons, muons and neutrinos as showers, which are called *atmospheric background*. The difference with the external particles is that the atmosphere is generally denser than astrophysical environments where shock acceleration takes place. Because of this increased density, the kinematics of interaction and decay plays an important role in the flux of electrons, muons and neutrinos from these showers. In the case of neutrinos (similarly for the rest) depending on the parent mesons two classes of backgrounds are distinguished [4] . Those originating from decays of pions and kaons are called conventional atmospheric neutrinos. Their parent mesons lifetimes are long enough for some of them to reinteract with another air nuclei instead of decaying. The spectrum of conventional atmospheric background results from this competition between decaying or reinteracting. The second class consists of neutrinos produced in the decay of charmed mesons. These mesons are short lived and decay immediately, and are called *called prompt neutrinos background*. The flux of this background in general depends on the neutrino energy and the zenith angle. Also is proportional to the cosmic ray spectrum $dN/dE \propto E^{-\alpha}$ with $\alpha \sim 2.7$. The atmospheric neutrino flux at Earth surface as a function of the neutrino energy and zenith angle is given by:

$$\frac{dN_\nu(E_\nu)}{dE} \propto E_\nu^\alpha \times \left\{ \frac{A_{\pi\nu}}{1 + B_{\pi\nu} cos\theta E_\nu/\epsilon_\pi} + \frac{A_{K\nu}}{1 + B_{K\nu} cos\theta E_\nu/\epsilon_K} + \frac{A_{D\nu}}{1 + B_{D\nu} cos\theta E_\nu/\epsilon_D} \right\} \tag{1.7}$$

The above three sums describe the contribution of pions, kaons and charm mesons respectively. The factors $A_{i\nu}$ and $B_{i\nu}$ contain the information about the physics of meson production and decay and do not depend of energy; where ϵ_i: $\epsilon_\pi = 115$GeV, $\epsilon_K = 850$

GeV and $\epsilon_D \sim 5 \times 10^7$ GeV respectively. For $B_{i\nu} cos\theta \, E_\nu >> \epsilon_i$ is observed that each individual term in the curly bracket in Eq.(1.7) is proportional to E_ν^{-1}. When the last inequality is not met (at lower energies) the neutrino spectrum follows the cosmic ray spectrum E_ν^α and at higher energies the spectrum becomes steeper by an additional factor of E_ν^{-1}. The fluxes of conventional and prompt neutrinos also depend differently on the zenith angle. The distance between the cosmic ray interaction height and a detector increases with zenith angle and consequently longer distance available to decay. So the flux of conventional neutrinos is enhanced. But with prompt neutrinos this phenomena does not happen as their parent mesons decay immediately.
A general panorama of particle messengers are shown in fig.(1.2).

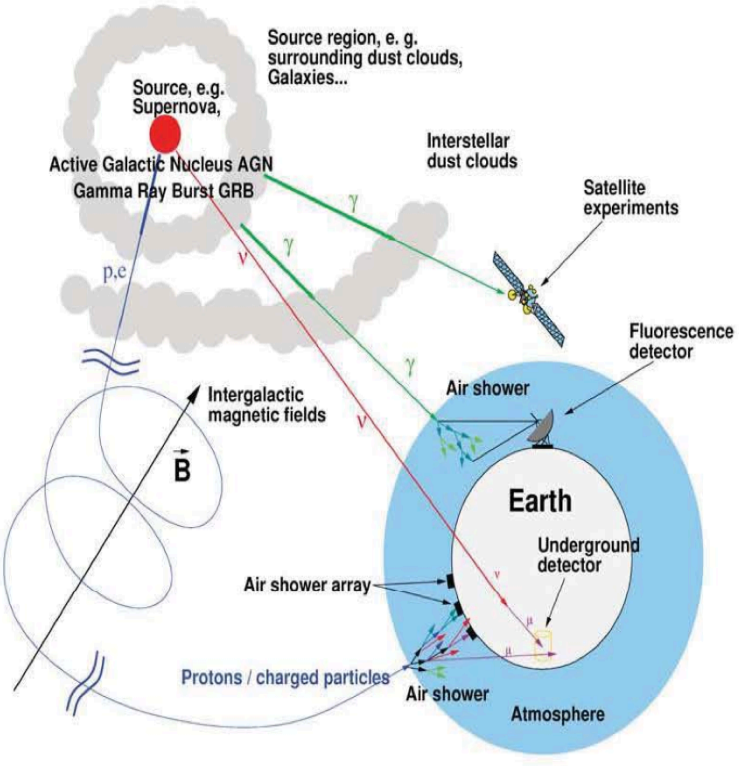

Figure 1.2: Multimessenger Astronomy, figure credit by Wolfwang Rhode

1.4 Sources of high energy particles

Based on Eq.(1.1), the Hillas diagram in fig.(1.3) shows that only some objects are capable of accelerate cosmic rays to high energies. In this thesis we consider in detail the galactic and extragalactic objects which can accelerate the particles up to the desire energies.

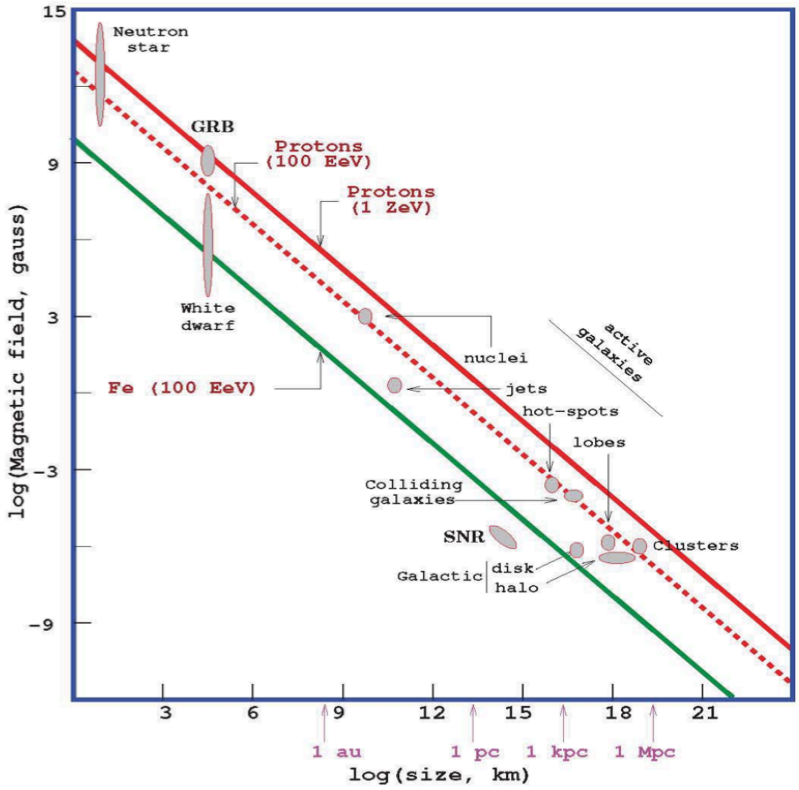

Figure 1.3: Hillas diagram that shows the sources that produce high energy cosmic rays with magnetic field and size required to accelerate particles to a maximum energy [5]

1.4.1 Galactic Sources

a) **Supernova Remnants (SNRs):** After the stellar explosion of a star the shells of matter form a shock wave that expands in the space at velocities of thousands of kilometers per second for a time of tens to thousands of years. As is known, the electrons are accelerated in the shock producing radio and x-ray radiations via synchrotron radiation. The photons with energies $\geq$ MeV could be produced by inverse Compton scattering, bremsstrahlung or neutral pion decay. While SNRs were one of the first

proposed sources of cosmic rays, the hadronic origin of the gamma-ray emission in most SNRs is ambiguous at the moment. The exception are Fermi observations of SNRs interacting with molecular clouds.

b) **Pulsars and Pulsars Wind Nebulae (PWN):** Pulsars are rapidly rotating highly magnetized neutron stars. They emit radiation along their spin axis in beamed form, producing a "pulsed" emission patterns when are observed on Earth. They are observed in radio, X-rays and gamma rays. These rotating neutron stars interact with surrounding material to produce a shock front. Also a cosmic ray flux is predicted due to this phenomena, and the extra galactic population of pulsars also generate an observable flux.

c)**Microquasars:** Microquasars are binary systems in which a compact object accretes matter from a donor star. They often have relativistic jets and are characterized by luminous X-ray emission, which is often time-dependent or periodic, some have been observed in TeV gamma rays. They are named microquasars by similarity with quasars but the compact objet is feed with a neighboring star and the scale is much smaller.

d)**Diffuse Galactic Emission:** This can be produced by the passage of cosmic rays through the Galactic disk. These passing cosmic rays can interact with this stellar medium within $\pm 2.5^o$ of the galactic latitude $b = 0$, or by interaction generated by star formation activity in the region of the galaxy. These emissions are still unclear.

e)**Dark Matter:** The existence of dark matter is supported by the galaxy rotation curves, gravitational lensing and observations of the CMB. Dark matter has not been detected yet and could be present everywhere including the Milky Way. Many dark matter models predict TeV-PeV particles that could produce neutrinos via decay or annihilation processes.

1.4.2 Extragalactic Sources

a)**Starburst Galaxy:** The property of these objects is the intense star formation activity and is thought to be produced due to galaxy mergers. In general the star formation endures for millions of years leading to higher average supernova rates and

consequently more process of acceleration. Also the cosmic ray population could interact with the interstellar medium, leading to neutrino production via *pp* interactions. The maximum flux could have a cutoff in PeV energy due to the maximum energy of the SNRs.

b)**Galaxy Clusters:** These are believed to accelerate cosmic rays in Mpc-scale shocks formed by accretion of matter onto the cluster or in termination shocks of galactic winds. Then, such cosmic rays could create neutrinos and gamma rays after interacting with the inter-cluster medium or background photon population. While some galaxy clusters could be observed as point sources, many of the closest clusters have extension of a few degrees.

c)**Gamma-Ray Bursts (GRBs):** These objects emit gamma rays ($\sim$100keV-2MeV) in the time interval of milliseconds to hundred of seconds. The origin of GRB is thought to be caused by massive star collapse or compact objects collision, giving the most luminosity known in the Universe after the Big Bang. The explanation of this phenomena is interpreted in the context of fireball model: a relativistic fireball with electrons, gamma-rays and baryons. As the fireball expands cosmic rays can be accelerated in strong shocks formed by colliding shells of plasma.

d)**GZK Neutrinos:** The cosmic ray absorption of the Cosmic Microwave Background via the GZK mechanism consist of the energy lose of the cosmic rays via $p\gamma$ interactions at the Δ^+ resonance, and the cutoff energy for this process is 4×10^{19} eV. If the cosmic rays creating these neutrinos are energetic enough and in consequence not be deflected by intergalactic magnetic fields, GZK neutrinos point back to cosmic ray sources. GZK neutrino fluxes depend on the cosmic ray flux, composition and the CMB spectrum.

e)**Active Galactic Nuclei (AGN):** are extremely luminous galaxies with accretion disk surrounding the supermassive black hole at their centers. Many are observed to have relativistic collimated outflows call *jets*. They are observed across the whole electromagnetic spectrum and many have time-dependent emission with periods of enhanced activity lasting for days or weeks. Cosmic rays are hypothesized to be accelerated up to EeV energies in shocks formed either by in falling matter near the AGN core or by colliding matter in the jets. This thesis focuses in a subclass of AGN called blazars.

1.5 AGN

As the name says these objects are located in the center of the galaxies, and are "active". Their activity makes them the most luminous persistent objects in the Universe. Huge amounts of material are being devoured by supermassive black hole, gas is ionized, turbulent electromagnetic fields of gigantic size are formed, and particles are accelerated to relativistic velocities and the emissions covers all the wavelengths.

1.5.1 History

Up to the seventeenth century, the humanity only used the eye to observe the Universe through light.The invention of the telescope amplified the sensitivity of the human eye and its angular resolution. This let humanity to discover, less than a century ago, that other galaxies exist, far beyond the Milky Way. Also it was observed that these galaxies are moving apart: the Universe expands. However, with the optical telescopes only a tiny part of the electromagnetic spectrum is observed. As soon as technology enabled humanity to open new windows we discovered other phenomena, other objects, and could push our knowledge farther out in space and time.

The opening of the radio window made the sixties the golden decade for astronomy, with the discovery of the microwave background and of the pulsars. The third great discovery made in that decade was the quasars. The term "quasar" originally stood for "quasi-stellar radio source" and refers to the fact that when an optical telescope is pointed towards the direction of this radio source, which can be as extended to arc minutes in radio maps, the resulting optical plate shows a source which looks like a star, i.e. not extended, a "point like" object. This apparently innocuous point is instead a gigantic energy plant, able to produce much more power that an entire galaxy like our own, in volume which is ridiculously small, if comparable with our Solar System. The process that powers the stars, thermonuclear reactions is not enough to power quasars. For this reason we believe that at the core of these sources there is a massive black hole, with a mass between few millions to a billion times the mass of the Sun. Matter around is attracted by the black hole gravity, it is compressed, heated and then radiates. Another major advance came with the opening of the X-ray window, first in the sixties with rocket experiments pioneered by Riccardo Giacconi, Bruno Rossi and others, and then with the first X-ray satellites, in the early seventies. The Uhuru, Ariel 5, HEAO-1 and the Einstein

satellites made clear that all kinds of quasars were strong X-ray emitters: at the same time, people started to believe that quasars were the major contributors to the cosmic diffuse X-ray background, already discovered in 1962 [6].

A third qualitative jump was the improvements of the interferometric technique in the radio band, in the early seventies. Radio telescopes in different continents, looking at the same source, can resolve details as close as a few tenth of a millisecond of arc. This enabled us to discover that some radio emitting quasars have spots of radio emission which are observed to move fast, this superluminal motion was even predicted before it was observed (by Martin Rees in 1966) and corresponds to real fast motion at an angle close to our line of sight.

1.5.2 Basic Components of AGN

The basic structure of AGN includes:
a)**A black hole** with $10^6 M_\odot < M < 10^{10} M_\odot$ which is probably spinning at some level.
b)**An accretion disk** Matter with even a small amount of angular momentum, attracted by the black hole gravity, spirals in and forms a disk. This is the major source of power.
c)**An X-ray corona** sandwiching the accretion disk. It is supposed to be a hot layer, or an ensemble of clumpy regions particularly active in the inner parts of the disk.
d)**An obscuring torus** located at several parsecs away from the black hole, intercepting some fraction of the radiation produced by the disk and re-emitting it in the infrared band.
e)**Broad Line Region** clouds at a distance of $\sim 10^{17} - 10^{18}$ cm from the hole (i.e. less than a parsec) moving rapidly ($\sim 3000 kms^{-1}$). They intercept $\sim 10\%$ of the ionizing radiation of the disk, and reemit it in the form of lines. Doppler shifts broaden the observed lines. This is why this region is called Broad Line Region (BLR).
f)**Narrow Line Region** at larger distances (~ 100 pc) there is another region where less dense clouds are moving less rapidly. This is called Narrow Line Region (NLR).
g)**Jets** . About 10% of AGNs, besides accreting matter, are able to expel it in two oppositely directed jets. Their direction likely traces the rotational axis of a spinning black hole. The material inside these jets is moving at relativistic speeds. Therefore the jet emission is highly beamed.

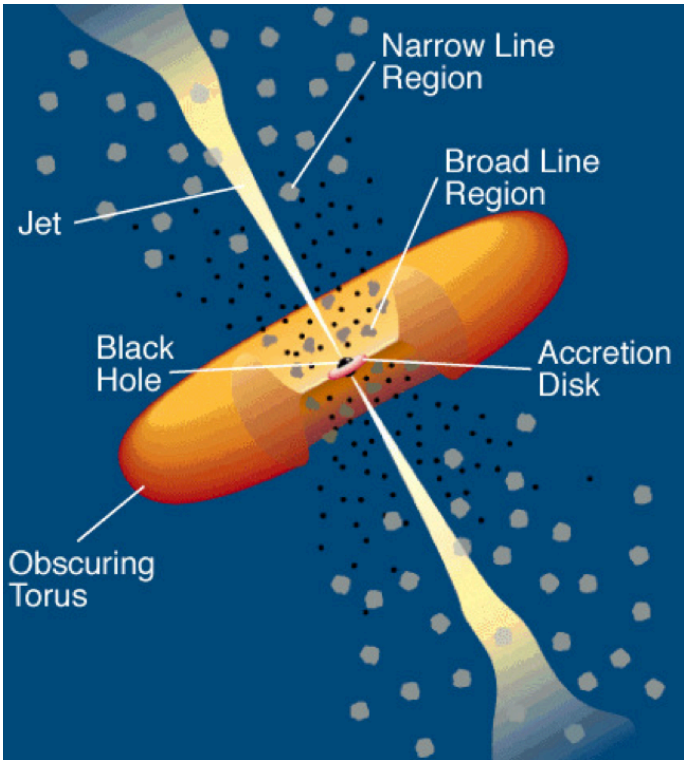

Figure 1.4: The figure shows the components of an AGN

1.5.3 AGN classification

Historically, a large variety of AGN are named due to their appearance from an Earth-based telescope. Most of the differences among various AGN can be explained with a geometrical axisymmetric model in which different appearances of AGN are the result of different angles of the observers line of sight to the AGN rotation axis (angle α).

Typically an AGN spectra are composed of a thermal part, the so called blue bump with the maximum at optical-UV frequencies, and a non thermal part extending over up to 20 orders of magnitude in frequency. Within the thermal spectrum, some emission lines are found (in the optical range), which are classified according to their width as broad lines and as narrow lines produced in BLR and NLR respectively. Depending on α, the broad line emission from the clouds at the center may or may not be hidden by the torus.

Also the luminosity of the disk and the jets is correlated within the AGN classes. The luminosity of the jet and the disk are both fractions of the total energy available, which is given by the mass accretion rate $Q_{accr} = \dot{M}_{disk}c^2$. The disk luminosity, which is dominated

by the blue bump is $L_{disk} = q_l Q_{accr}$ and for the jet it is $Q_{jet} = q_j Q_{accr}$. The observed correlations between q_l and q_j justify the concept that AGN are a coupled jet-disk system.

The radio emission of AGN is assumed to originate mostly in relativistic jets due to the synchrotron radiation of electrons gyrating along the jet. AGN are classified as radio loud if the ratio to the radio flux at 5GHz to the optical flux is larger than 10; in contrast AGN with a smaller value of this ratio are classified as radio weak. According to this classification, 10% of the observed AGN are radio loud and in general elliptical galaxies, while 90% are radio weak and mostly spiral galaxies.

Observations and jet models show a flat radio spectrum for the inner part of the jet, i.e., for the radio core. The radio spectrum is called flat, if the flux density F_γ as a function of the frequency ν is described by a power law $F \propto \nu^\alpha$ with a spectral index $\alpha > -0.5$. In contrast radio lobes and hot spots located at the outer end of the jet typically show steeper spectrum with spectral indices from -0.5 to -0.6 in hot spots and from -0.8 to -1 in lobes. Two different jet morphologies have been observed for radio-loud AGN correlated with the radio luminosity at low frequencies. Historically, this correlation was found by Fanaroff and Riley for sources observed under a large inclination angle. The luminosity is classified according to L_{178}, the luminosity at 178 MHz. AGN with high luminosity are characterized by powerful jets extending far outside the host galaxy. The increasing jet luminosity at the outer edge produces extended radio lobes and the so called hot spots. Less powerful AGN have fainter jets. They show decreasing radio emission with growing distance from the central hole and do not have hot spots, seem to be fading out. The critical value was found at $L_{178} = 2.5 \times 10^{26}$W/Hz, and in contrast to the jet morphology, the radio luminosity can be observed under a large range of inclination angles. It is preferred as criterion because it provides a more general classification of AGN based on their intrinsic properties. In addition to the last classification there are 1/3 of the radio loud sources showing a steep radio spectrum from the compact radio core for frequencies above a certain turnover frequency. If the turnover is in the range of MHz, the object is classified as Compact Steep Spectrum source (CSS), and if it is in the range of GHz, the object is a GHz Peaked Source (GPS). These sources are significantly smaller than usual AGN. The linear of GPS is below 1 kpc, and the size of CSS is usually in 1-5 kpc. For comparison the size of radio loud

AGN is typically in the range of hundred of kpc, while the largest AGN jets are several Mpc. The compactness of the sources can be explained by the assumption that the jets get stopped by the interaction with dense matter. One proposal in this context is that GPS/CSS are just the young states of radio-loud AGN evolving into the larger radio sources.

The observation of extended radio loud AGN under different inclination angles results in different appearances of the source type due to the relativistic Doppler boost of the emission from the jet and the possibility of the obscuration of the inner core by the torus. Of the fig. (1.5) we can define three criteria:

a)$\alpha > \alpha_{torus}$: the inclination angle is larger than the opening angle of the torus. The

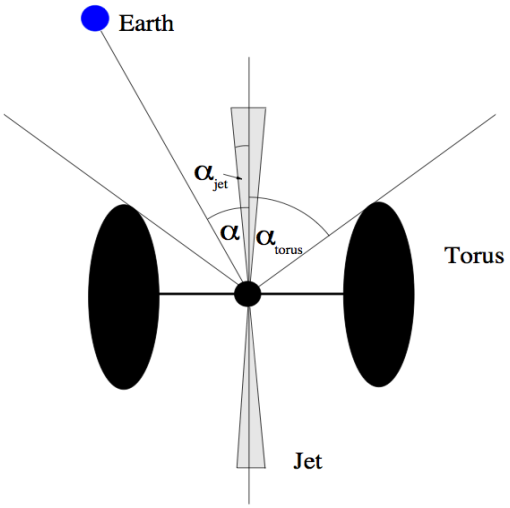

Figure 1.5: Geometrical axisymmetric model in base to the α rotation angle

inner core of the AGN is obscured.

b)$\alpha_{jet} < \alpha < \alpha_{torus}$ the inclination angle is large enough that emissions from the jet are not enhanced, but we could see the accretion disk.

c)$\alpha < \alpha_{jet}$ the inclination angle is small and the observer looks directly into the jet. Any emission from the jet is relativistically boosted towards the observer.

For $\alpha > \alpha_{torus}$ the broad line region and the thermal continuum radiation of the accretion disk cannot be seen and the AGN is called a radio galaxy. Low luminosity objects with weaker jets are classified as FR-I (Fanaroff and Riley) radio galaxy with the above definition and the ones with high luminosity as FR-II radio galaxies. In the second

case the AGN spectrum is dominated by the blue bump from the inner accretion disk and broad emission lines from fast moving dust clouds. The radio spectrum of these objects is still steep and lobe-dominated. Only high luminosity objects show this morphology, referred to as Steep Spectrum Radio Quasars (SSRQ) with a bright optical core and strong broad emission lines. The lack of similar low luminosity objects is still a matter of debate. In the third case $\alpha < \alpha_{jet} \sim 12^o$, the observer is looking into the jet under a very small inclination angle so that the radiation from the jet is Doppler boosted due to relativistic motion of the bulk outflow towards the observer. The Flat Spectrum Radio Quasars (FSRQ) are interpreted as the high luminosity objects with the FR-II type jet seen from small inclination angles, and for low luminosity BL Lac with FR-I. The BL Lac objects are commonly divided into high energy cutoff BL Lac (HBL) and low energy cutoff LaC (LBL) referring to the maximum energy of the electron synchrotron spectrum. The radio emission of HBL is relatively weak, while they are strong X-ray emitters. The total luminosity of HBL is significally smaller than of LBL. A distinction between these classes is usually made by taking into account whether the radio to X-ray spectral index α_{rx} is greater (LBL) or less (HBL) than -0.75.
Radio weak AGN are classified too, in base to luminosity and the inclination angle. The luminosity at optical wavelengths is used for the classification. Optically strong objects are called radio-weak quasars and radio Intermediate Quasars (RIQ). Weaker objects are named Seyfert galaxies. As for the radio-loud AGN, the inclination angle determines the relativistic beaming of emission from the jet and the obscuration of central emission by the torus. RIQ are seen at angles between $20^o - 60^o$ while the radio weak quasars at small angles. The radio emission of RIQ is relativistically beamed analogously to blazars. Seyfert galaxies are classified as Seyfert I galaxies, if the core including the broad line region are visible, or Seyfert 2 if the core is obscured by the torus. Up to now, no Seyfert like objects with beamed emission have been observed.

1.5.4 Spectral Energy Distribution of Blazars

The spectral energy distribution (SED) of the AGN has a double peak structure in the $\nu - \nu F_\nu$ plane. Here the SED is modelled by single zone synchrotron and synchrotron self Compton (SSC) model where the emission region is a spherical blob of radius R'_b and is expanding with a bulk Lorentz factor Γ. The emission region has a magnetic field B' measured in Gauss. The low energy peak corresponds to the synchrotron radiation

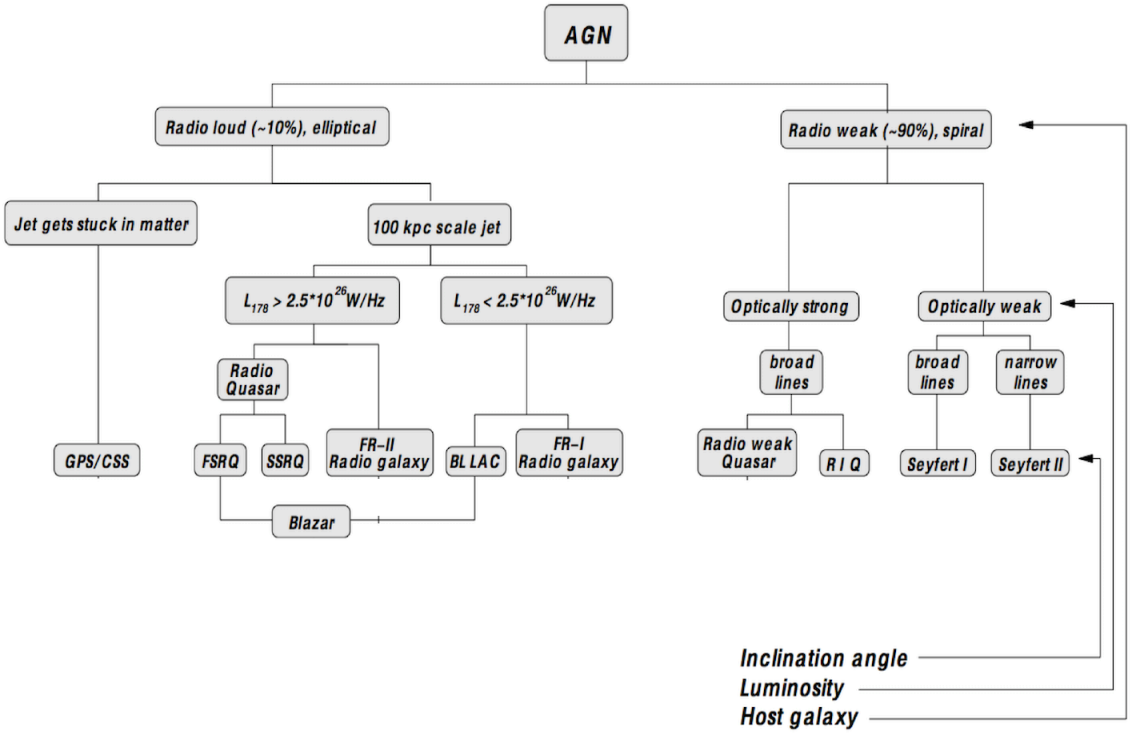

Figure 1.6: AGN classification scheme

from a population of relativistic electrons in the blob. The general consensus is that the high energy peak corresponds to the SSC scattering of the high energy electrons with their self-produced synchrotron photons in the blob. This implies a direct correlation of the two bumps. The multi zone model is also used to explain the SED. Depending on the energy range of the second bump in the SED, Blazar objects can be further divided into subclasses: High-peaked BL Lacs(HBLs), Low-peaked BL Lacs (LBLs) and Flat Spectrum Radio Quasars (FSRQs). If the peak occurs at TeV energies, sources are called HBLs, while they are referred to as LBLs at peak energies in the GeV range. The source is called FSRQ for lower peak energies than the LBL class. The sample of fig.(1.7) is further divided into five sub-samples, selected via their radio luminosity at 5 Ghz, $\log(L_{radio}/erg) = (< 41, 42-43, 43-44, 44-45, > 45)$. The explanation of both these peaks through the synchrotron and SSC processes are called *leptonic model* as leptons (electrons and positrons) only play the important role. This model is very successful in explaining the multi wavelength emission from blazars and FR I galaxies such as NGC 1275 and M87 [7, 8] and also Centaurus A [9, 10].

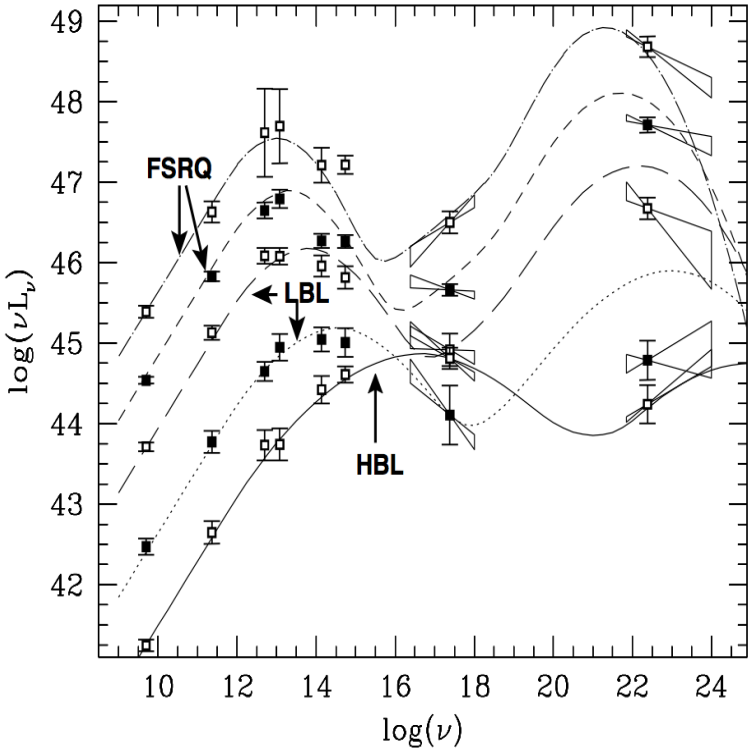

Figure 1.7: The blazar sequence. As the bolometric luminosity increases, the peak of the two broad peaks shifts to smaller frequencies, and the high energy hump becomes more important.

1.5.5 Flaring of Blazars

Flaring or outburst seems to be the major activity of the blazars which is unpredictable and switches between quiescent and active states involving different time scales. During the flaring the blazar flux can go up by more than an order of magnitude than the average baseline flux in few minutes and also there can be a third peak in the multi-TeV energy range. While in some blazars a strong temporal correlation between X-ray and multi-TeV γ-rays has been observed, flaring in some cases have not low energy counterparts, and in this case are called "orphan flares". Explanation of the third peak in the multi-TeV energy range is challenging where normally one zone leptonic model fails. Multi zone leptonic model with more parameters can explain this. Explanation of such extreme activities call for different mechanisms. Also simultaneous multiwavelength observation of the flaring period is necessary to constraint different theoretical models of emission in different energy regimes.

1.6 IceCube detector

The idea of a large scale cubic kilometer neutrino detector dates back to 1960s. In the 1980s, the (Deep Underwater Muon And Neutrino Detector Project) DUMAND collaboration began the construction of prototype strings for such a detector, to be located in the deep ocean near Hawaii. A prototype string of optical sensors was deployed, which took data for a short time, before failing. The collaboration pursued these efforts into the early 1990s before this pioneering project was unfortunately cancelled. Around the same time, other teams were exploring a similar idea. Two experiments were eventually constructed, one in the large fresh water lake in Siberia, Lake Baikal, and one in the deep ice at the South Pole, AMANDA (Antarctic Muon And Neutrino Detector Array). Ice and water each have advantages and disadvantages, ice has a shorter scattering length (less optical for particle directional reconstruction as the Cherenkov cone is degraded) but a longer absorption length (more optimal for energy reconstruction as photons survive longer and travel further from their emission points). The South Pole has the advantage over water of having a solid surface to work, accessible for construction, operations during the southern hemisphere summer. During the 1990s and early 2000s AMANDA and Baikal were constructed and operated. Also in the Mediterranean the water detector ANTARES (Astronomy with a Neutrino Telescope and Abyss environmental RESearch) was deployed. These detectors explored the full range of energy in their possibilities, but it was clear that a bigger detector was needed, and that is why the IceCube detector was conceived and constructed. The core element of the IceCube detector is the digital optical module (DOM) a glass pressure sphere containing a 10 inch photomultiplier tube, and digital processing electronics. The DOMs, with nanosecond accuracy, can record the arrival time distribution of thousand of photons arriving over microsecond scales. IceCube was constructed over seven summer seasons at the South Pole where 86 vertical strings of 60 DOMs per string were deployed into hot water drilled holes. The DOMs were installed from depths 1450 meters to 2450 meters, with a string spacing of 125 metros, giving an instrumented volume of a one cubic kilometer. Eight of the strings were deployed near the centre of the array, to make a more densely instrumented region, known as DeepCore. This enhances the sensitivity to low energy neutrinos. On the surface, two frozen water tanks containing optical sensors were deployed per string, for cosmic ray air shower studies (the IceTop air shower array). All the photon timing information from the ice in the DOMs surface is digitized and analyzed by a cluster of computers in the IceCube

laboratory at the surface. Further event processing and filtering in the IceCube laboratory at the surface leaves a total data volume sent out over satellite of approximately 100 GB per day. The detector was operational from the time of the single first string, and data were taken with sub detectors IC1, IC9, IC22, IC40, IC59, IC79 and finally, IC86 is operational, with nearly four years of data taken in the final configuration up to the end of 2014. In fig (1.8) we have shown the schematic diagram of the IceCube Detector in South Pole.

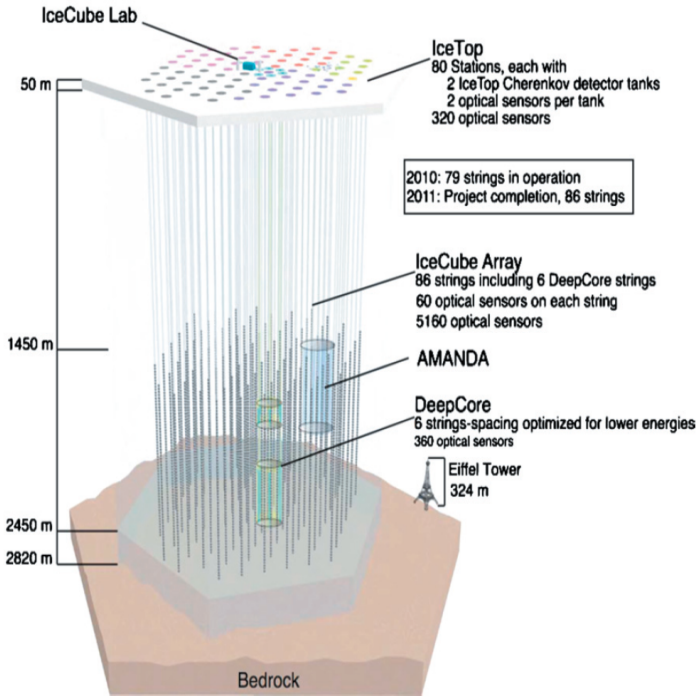

Figure 1.8: Schematic figure of IceCube detector

1.6.1 Detection

A neutrino detector, like IceCube, detect high energy neutrinos by observing the Cherenkov radiation emitted by the secondary charged particles produced when high energy neutrinos interact with the surrounding rock and ice [11]. These secondaries produce showers events and/or tracks events depending on the primary neutrino flavor. The neutrino interaction with rock and ice takes place through neutral current (NC) and/or charge current (CC) weak processes:

$$\begin{aligned} \nu_l + N \rightarrow l + X \quad (CC) \\ \nu_l + N \rightarrow \nu_l + X \quad (NC) \end{aligned} \tag{1.8}$$

In the NC case, since there is a neutrino in the final state, the only signature of the interaction will be through the hadronic shower, independent of the neutrino flavor. In the CC case the end-result depends on neutrino flavor. If the interacting neutrino is an electron type, the resulting electron will quickly interact with the medium, producing an electromagnetic shower, which will overlap with the hadronic shower. If the neutrino is of muon type, the resulting muon will produce a long track that emerges from the shower. Finally, if the neutrino is tau type, the resulting tau lepton may or may not produce a track depending on its energy. But when the tau decays into muon, $\tau \rightarrow \nu_\mu \, \mu \, \nu_\tau$ the later will produce a long track, just like in the case of a muon-neutrino CC interaction, this modifies the number of track events, which has to be accounted for. Neutrinos coming from underneath the detector, those with energies above 1 PeV will be drastically suppressed, and therefore the *lollipop* and *double-bang* events that are associated with very energetic ν_τ will also be suppressed [12].

The High energy neutrinos events observed by IceCube have two different topologies: **shower** topology (also known as cascade), that includes NC interactions of all neutrino flavors and CC interactions of ν_e and ν_τ; **track** topology produced by CC interactions of ν_μ. The electromagnetic and hadronic cascades contain charged particles, which can emit Cherenkov radiation. This shower will be absorbed soon in the ice and can't travel longer distance. However, when ν_μ interacts with the rocks near the Icecube detector, it will produce μ in the CC interaction. The muon can travel longer distance in the ice producing a longer trail of Cherenkov photons producing a track. The IceCube detector can differentiate the shower and the track events.

1.6.2 Cherenkov Radiation

High energy neutrinos are detected via the charged particles they produce. These charged particles travel faster than the speed of light in the medium, generating radiation via the Cherenkov Process, producing a coherent shockwave of electromagnetic radiation. This effect is similar to the sonic boom created by an airplane traveling faster then the speed of sound and the wake created by a boat moving faster than the speed of water waves.

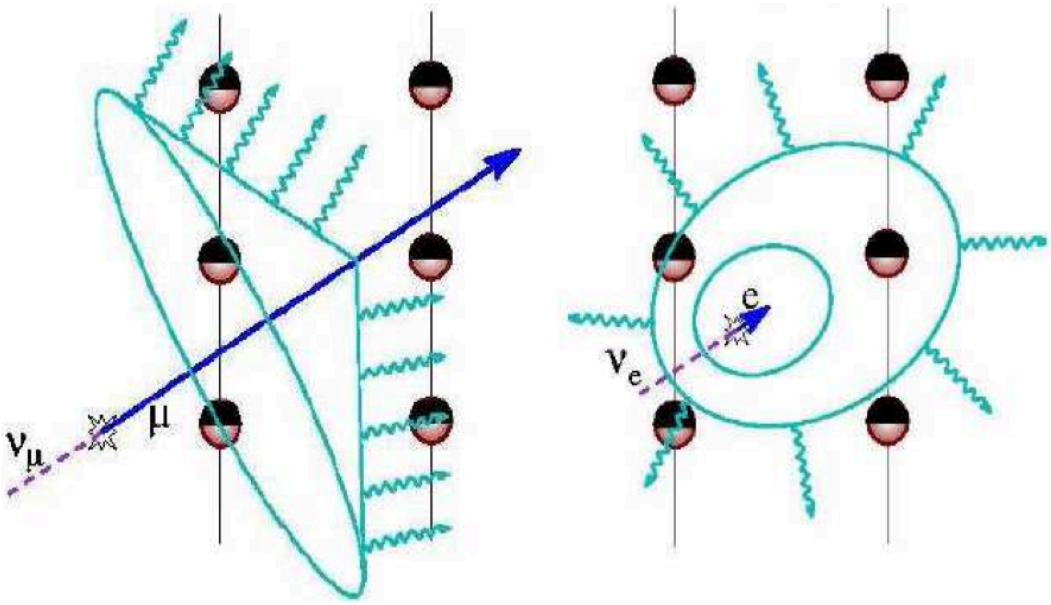

Figure 1.9: Shower and Track events

Cherenkov light is emitted along a cone, with a characteristic angle

$$cos\theta_c = \frac{1}{\beta n(\lambda)} \tag{1.9}$$

where $\beta = v/c$ is the relative velocity of the particle and n is the index of refraction of the medium. For a relativistic charged particle traveling through ice $\theta_c \propto 41^o$. The photon yield as a function of wavelength is given by the Frank-Tamm formula [13]:

$$\frac{d^2N}{dxd\lambda} = \frac{2\pi\alpha}{\lambda^2}\left(1 - \frac{1}{\beta^2 n^2(\lambda)}\right), \tag{1.10}$$

where α is the fine structure constant. The emission is peaked at shorter wavelengths, making Cherenkov light appear blue. The IceCube neutrino detector detect Cherenkov light from leptons to estimate the energy and the direction of the primary neutrino.

Chapter 2

Concepts

There are four topics very useful in the develop of this thesis. The first one has its origin in the problem of the leptonic model in orphan flares; basically if the leptonic model produces the multi-TeV emissions in blazars we have to observe simultaneously a counterpart in low energies (in the range of X-rays) but is not always the case. One solution is based in the hadronic models and in this work we use and simplify the model of Sahu et al. which will be explained in detail.
The second one is to obtain a simplified version of the muon neutrino atmospheric flux; finally one of the ways to distinguish between the muon neutrinos that come form the space and the atmosphere is due to the form of the fluxes, these are like their fingerprints. And the third and fourth are the maximum likelihood method and the effective areas for muon neutrinos; together are a very powerful tool to evaluate a significant correlation for a neutrino event detected and a possible extraterresterial object. Below they will be reviewed the concepts.

2.1 Limitations of leptonic model

The leptonic model is very successful in explaining the multi wavelength emission from blazars and FR I galaxies. The essential outcome of the leptonic models is that, outburst/flaring at multi-TeV energy should be accompanied by a simultaneous enhance emission in low energies. Unfortunately the enhanced synchrotron emission was not observed in the flaring of 1ES 1959+650 in June 2002 [14] and also probably in the flaring of Mrk 421 in April 2004 [15], which implies that the SSC model may not be efficient

enough to contribute in the multi-TeV regime. Also multi zone leptonic models are used to explain the third peak where more free parameters are needed to explain the peak.

Alternative models are proposed to explain the multi-TeV emission from AGN. In the hadronic model, the high energy peak is produced due to proton synchrotron emission or decay of neutral pions formed in cascades from the interaction of high energy proton beam with the radiation or gas clouds surrounding the source [16]. In this scenario, a strong correlation between the gamma-ray and the neutrino fluxes is expected [17–19].

Recently in a series of papers, Sahu et al. [20,21] have explained the multi-TeV flaring from many blazars by using a modified version of hadronic model. The analysis of the production of high energy neutrinos from blazars as well as the multi-TeV emission from the HBL Markarian 421 is based on this model. In the next section we discuss in detail about this model.

2.2 Photohadronic Model of Sahu et al.

The photohadronic model of Sahu et al. rely on the standard interpretation of the leptonic model to explain both, low and high energy peaks by synchrotron and SSC photons respectively as in the case of any other AGNs and Blazars. Thereafter, it is proposed that the flaring occurs within a compact and confined volume of radius R'_f inside the blob of radius R'_b ($R'_f < R'_b$). In this picture the internal and the external jets are moving with the same bulk Lorentz factor Γ and the Doppler factor $\mathcal{D}$ as the blob. The geometrical structure of the model is shown in fig. (2.1). Within the confined volume, the injected spectrum of the Fermi accelerated charged particles has a power-law with an exponential cut-off [20, 22], and for the protons with energy E_p it is given as

$$\frac{dN_p}{dE_p} \propto E_p^{-\alpha} e^{-E_p/E_{p,c}}, \tag{2.1}$$

where the high energy proton has the cut-off energy $E_{p,c}$ and the spectral index $\alpha > 2$. Also in this small volume, the commoving photon number density $n'_{\gamma,f}$ (flaring) is much higher than in the rest of the blob n'_γ (non-flaring), which can be due to the copious annihilation of electron positron pairs, splitting of photons in the magnetic field, enhance IC photons in this region and Poynting flux dominated flow which can form, from the magnetic reconnection in the strongly magnetized plasma around the base of the jet [23, 24]. This relation can be expressed as $n'_{\gamma,f}(\epsilon_\gamma) = \lambda n'_\gamma(\epsilon_\gamma)$, where $\lambda \gg 1$. Unfortunately, it is

unknown exactly the properties of the inner jet except that the photon density, the energy density of photons and the magnetic field are higher than in the outer jet and that multi-TeV γ-rays and neutrinos can be produced through intermediate Δ-resonance. For this reason the scaling behavior of the photon densities in flaring and non-flaring region is assumed and is given by

$$\frac{n'_{\gamma,f}(\epsilon_{\gamma_1})}{n'_{\gamma,f}(\epsilon_{\gamma_2})} \simeq \frac{n'_{\gamma}(\epsilon_{\gamma_1})}{n'_{\gamma}(\epsilon_{\gamma_2})}, \tag{2.2}$$

which implies that, the ratio of photon densities at two different background energies ϵ_{γ_1} and ϵ_{γ_2} in flaring and non-flaring states remains almost the same. For a self consistent treatment, in principle one should use the photon density $n'_{\gamma,f}$ in the hidden internal jet and solve the coupled transport equations for leptons and photons along the jet by taking into account their respective cooling mechanisms as well as the injection spectrum of the primary particles [25]. To avoid this complication the scaling behavior of the photon densities in different background energies as shown in Eq. (2.2) is assumed.

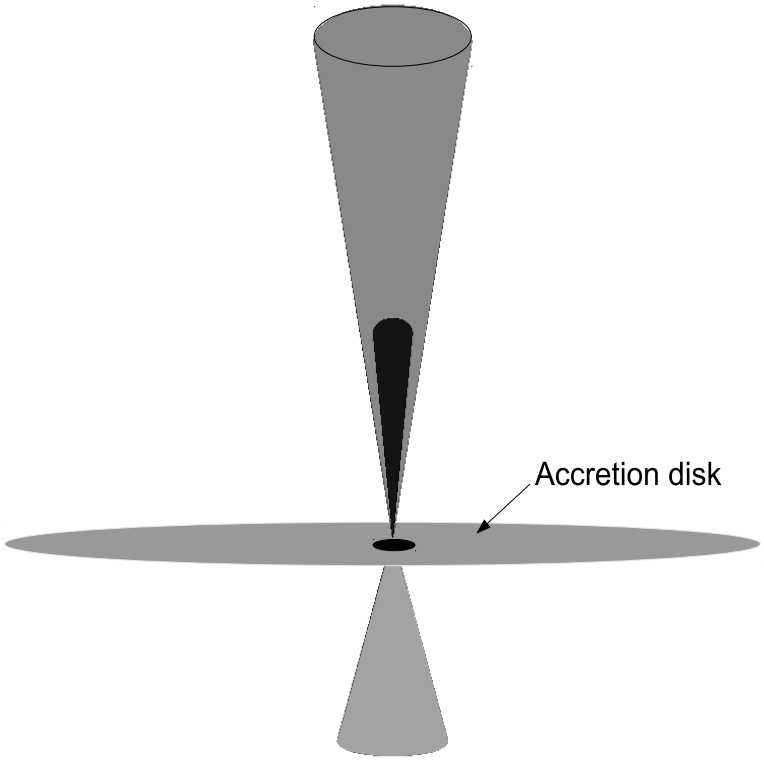

Figure 2.1: Geometrical structure of the internal and the external jet regions: the interior compact cone is responsible for the multi-TeV flaring and the exterior cone corresponds to the normal jet.

Fermi-accelerated high energy protons interact with the SSC photons in the compact

region of the jet to produce the Δ-resonance. Subsequently the Δ-resonance decays to charged and neutral pions as follows:

$$p + \gamma \rightarrow \Delta^+ \rightarrow \begin{cases} p\,\pi^0, & \text{fraction } 2/3 \\ n\,\pi^+, & \text{fraction } 1/3 \end{cases}, \tag{2.3}$$

which has a cross section of $\sigma_\Delta \sim 5 \times 10^{-28}\,\mathrm{cm}^2$. Subsequently, the charged and neutral pions will decay through $\pi^+ \rightarrow \mu^+ + \nu_\mu \rightarrow e^+\nu_e\nu_\mu\bar{\nu}_\mu$ and $\pi^0 \rightarrow \gamma\gamma$ respectively. The produced neutrinos and photons are in the GeV-TeV range energy. For the production of Δ-resonance, the kinematical condition is

$$E'_p\epsilon'_\gamma = \frac{(m_\Delta^2 - m_p^2)}{2(1 - \beta_p \cos\theta)}, \tag{2.4}$$

where E'_p and ϵ'_γ are respectively the proton and the background photon energies in the commoving frame of the jet. We define the quantities with a prime in the commoving frame and without prime in the observer frame. For high energy protons we assume $\beta_p \simeq 1$. Since in the commoving frame the protons collide with the SSC photons from all directions, in our calculation we consider an average value $(1 - \cos\theta) \sim 1$ (θ in the range of 0 and π). Going from commoving frame to observer frame, the proton and photons energies can be written as

$$E_p = \frac{\Gamma E'_p}{(1+z)}, \tag{2.5}$$

$$\epsilon_\gamma = \frac{\mathcal{D}\epsilon'_\gamma}{(1+z)} \tag{2.6}$$

where $\Gamma, \mathcal{D}$ are the Lorentz and Doppler factors respectively and the kinematical condition given in Eq.(2.4) can be written in the observer frame as

$$E_p\epsilon_\gamma \simeq 0.32\ \frac{\Gamma\mathcal{D}}{(1+z)^2}\ \mathrm{GeV}^2. \tag{2.7}$$

In the jet commoving frame, each pion carries ~ 0.2 of the proton energy while 50% of the π^0 energy will be given to each γ. So the relationship between high energy γ-ray and the E_p is $E_\gamma = \mathcal{D}E_p/10$. From these relations we can express the Δ-resonance kinematical condition in terms of photon energies (target photon energy ϵ_γ and the observed photon energy E_γ) as

$$E_\gamma\epsilon_\gamma \simeq 0.032\ \frac{\mathcal{D}^2}{(1+z)^2}\ \mathrm{GeV}^2. \tag{2.8}$$

A similar relation could be obtained if we change the final photon for a neutrino:

$$E_\nu \epsilon_\gamma \simeq 0.016 \ \frac{\Gamma \mathcal{D}}{(1+z)^2} \ \mathrm{GeV}^2. \tag{2.9}$$

The number of π^0-decay photons at a given energy is proportional to both the number of high energy protons and the density of the SSC background photons in the jet, i.e. $N(E_\gamma) \propto N(E_p) n'_\gamma$. For the flaring case, n'_γ is replaced by the photon density in the flaring region given by $n'_{\gamma,f}$. The γ-ray flux from the π^0 decay is then given by

$$F_\gamma(E_\gamma) \equiv E_\gamma^2 \frac{dN(E_\gamma)}{dE_\gamma} \propto E_p^2 \frac{dN(E_p)}{dE_p} n'_{\gamma,f}. \tag{2.10}$$

Using the scaling behavior of Eq.(2.2), the observed multi-TeV photon flux from π^0-decay at two different observed photon energies $E_{\gamma 1}$ and $E_{\gamma 2}$ can be expressed as

$$\begin{aligned} \frac{F_\gamma(E_{\gamma_1})}{F_\gamma(E_{\gamma_2})} &= \frac{n'_{\gamma,f}(\epsilon_{\gamma_1})}{n'_{\gamma,f}(\epsilon_{\gamma_2})} \left(\frac{E_{\gamma_1}}{E_{\gamma_2}}\right)^{-\alpha+2} e^{-(E_{\gamma_1}-E_{\gamma_2})/E_c} \\ &= \frac{n'_{\gamma}(\epsilon_{\gamma_1})}{n'_{\gamma}(\epsilon_{\gamma_2})} \left(\frac{E_{\gamma_1}}{E_{\gamma_2}}\right)^{-\alpha+2} e^{-(E_{\gamma_1}-E_{\gamma_2})/E_c} , \end{aligned} \tag{2.11}$$

where $E_{\gamma_{1,2}}$ are two different γ-ray energies and correspondingly the proton energies are $E_{p_{1,2}}$. In the above equation (2.11) we have used the relations

$$\frac{E_{p_1}}{E_{p_2}} = \frac{E_{\gamma_1}}{E_{\gamma_2}}. \tag{2.12}$$

In terms of SSC photon energy and its luminosity, the photon number density n'_γ is expressed as

$$n'_\gamma(\epsilon_\gamma) = \eta \frac{L_{\gamma,SSC}(1+z)}{\mathcal{D}^{2+\kappa} 4\pi R'^2_b \epsilon_\gamma}, \tag{2.13}$$

where η is the efficiency of SSC process and κ describes whether the jet is continuous ($\kappa = 0$) or discrete ($\kappa = 1$). In this model we take $\eta = 1$ for full efficiency. The SSC photon luminosity is expressed in terms of the observed flux ($\phi_{SSC}(\epsilon_\gamma) = \epsilon_\gamma^2 dN_\gamma/d\epsilon_\gamma$) and is given by

$$L_{\gamma,SSC} = \frac{4\pi d_L^2 \phi_{SSC}(\epsilon_\gamma)}{(1+z)^2} \tag{2.14}$$

Furthermore, by using Eq.(2.13) we can simplify the ratio of the photon densities

$$\frac{n'_\gamma(\epsilon_{\gamma 1})}{n'_\gamma(\epsilon_{\gamma 2})} = \frac{\phi_{SSC}(\epsilon_{\gamma 1})}{\phi_{SSC}(\epsilon_{\gamma 2})} \frac{E_{\gamma 1}}{E_{\gamma 2}}. \tag{2.15}$$

Here we take $\kappa = 0$ as representative value for the calculation of $n_{\gamma}^{'}$. We note that $\kappa = 1$ will only lead to the suppression of the photon number density for the outer enveloping jet without changing the main conclusions. By taking the ratio we get rid of the common factors and the proportionality constant. The ratio between the fluxes in Eq. (2.11) takes the form

$$\frac{F_\gamma(E_{\gamma 1})}{F_\gamma(E_{\gamma 2})} = \frac{\phi_{SSC}(\epsilon_{\gamma 1})}{\phi_{SSC}(\epsilon_{\gamma 2})} \left(\frac{E_{\gamma 1}}{E_{\gamma 2}}\right)^{-\alpha+3} e^{-(E_{\gamma 1}-E_{\gamma 2})/E_c}. \tag{2.16}$$

The Φ_{SSC} at different energies are calculated using the leptonic model. Here the multi-TeV flux is proportional to $E_\gamma^{-\alpha+3}$ and $\Phi_{SSC}(\epsilon_\gamma)$. Finally in the photohadronic process $(p\gamma)$, the multi-TeV photon flux is expressed as

$$F(E_\gamma) = A_\gamma \Phi_{SSC}(\epsilon_\gamma) \left(\frac{E_\gamma}{TeV}\right)^{-\alpha+3} e^{-E_\gamma/E_c}. \tag{2.17}$$

Both ϵ_γ and E_γ satisfy the condition given in Eq.(2.8) and the dimensionless constant A_γ is given by

$$A_\gamma = \left(\frac{F(E_{\gamma_2})}{\Phi_{SSC}(\epsilon_{\gamma 2})}\right) \left(\frac{TeV}{E_{\gamma_2}}\right)^{-\alpha+3} e^{E_{\gamma_2}/E_c}. \tag{2.18}$$

A_γ can be fixed from the observed flare data.

The optical depth of the Δ-resonance process in the inner jet region is given by

$$\tau_{p\gamma} = n'_{\gamma,f} \sigma_\Delta R'_f. \tag{2.19}$$

The efficiency of the $p\gamma$ process depends on the physical conditions of the interaction region, such as the size, distance from the base of the jet, photon density and their distribution in the region. Most of these parameters are unknown in the hidden inner jet region. In this region we compare the dynamical time scale $t'_d = R'_f$ (expansion of the blob) with the $p\gamma$ interaction time scale $t'_{p\gamma} = (n'_{\gamma,f}\sigma_\Delta K_{p\gamma})^{-1}$ to constrain the seed photon density so that multi-TeV photons can be produced. For a moderate efficiency of this process, we can assume $t'_{p\gamma} > t'_d$ and this gives $\tau_{p\gamma} < 2$, where we take the inelasticity parameter $K_{p\gamma} = 0.5$. And by assuming the Eddington luminosity is equally shared by the jet and the counter jet, the luminosity within the inner region for a seed photon energy ϵ'_γ will satisfy $(4\pi n'_{\gamma,f} R'_f \epsilon'_\gamma) \ll L_{Edd}/2$. This puts an upper limit on the seed photon density as

$$n'_{\gamma,f} \ll \frac{L_{Edd}}{8\pi R'^2_f \epsilon'_\gamma}. \tag{2.20}$$

From Eq.(2.20) we can estimate the photon density in this region.

In this picture, in $\tau_{p\gamma}^{-1}$ many protons can interact with the SSC background to produce photons and neutrinos as shown in Eq.(2.3). So the fluxes of the TeV photons and the Fermi accelerated high energy protons F_p, are related through

$$F_p(E_p) = 5 \times \frac{3}{2} \frac{1}{\tau_{p\gamma}(E_p)} F_\gamma(E_\gamma), \tag{2.21}$$

where the factor 5 corresponds to 20% of the proton energy taken by each π^0 and 3/2 is due to the 2/3 probability of Δ-resonance decaying to $p\pi^0$. Like photons, the proton fluxes at different energies $E_{p,1}$ and $E_{p,2}$, scale as

$$\frac{F_p(E_{p1})}{F_p(E_{p2})} = \frac{\tau_{p\gamma}(E_\gamma 2)}{\tau_{p\gamma}(E_\gamma 1)} \frac{\phi_{SSC}(\epsilon_{\gamma 1})}{\phi_{SSC}(\epsilon_{\gamma 2})} \left(\frac{E_{\gamma 1}}{E_{\gamma 2}}\right)^{-\alpha+3} e^{-(E_{\gamma 1}-E_{\gamma 2})/E_c}. \tag{2.22}$$

The fluxes of π^+ and π^0 are related, because each pion carries 20% of the proton energy, while each neutrino and each e^+ carries 1/4 of the π^+ energy, from the π^0 decay the photon carries 1/2 of the π^0 energy. The neutrino and e^+, each has energy $E_\nu = E_{e^+} = E_\gamma/2$ and the neutrino flux can be calculated from the GeV-TeV photon flux, through [21]

$$F_\nu = \frac{3}{8} F_\gamma, \tag{2.23}$$

where we assume that the TeV photon flux in the flaring state is mainly due to the hadronic process. For the observed highest energy γ-ray E_γ corresponding to a proton energy E_p, the proton flux $F_p(E_p)$ will be always smaller than the Eddington flux F_{Edd}. This condition puts a lower limit on the optical depth of the process and is given by

$$\tau_{p\gamma}(E_p) > 7.5 \times \frac{F_\gamma(E_\gamma)}{F_{Edd}}. \tag{2.24}$$

From the comparison of different times scales and from Eq.(2.24) we will be able to constrain the seed photon density in the inner jet region.

2.3 Muon atmospheric neutrino flux

The equations of an air shower in slant depth X in g/cm^2 are called the cascade equations. Under some assumptions, these are solved analytically for the flux of muons and neutrinos (from 2-body decay of charged pions and kaons). For a complete analysis please refer

to [4]. First we begin with the cascade equations of the parent mesons produced in the air shower. For a hadron species i the differential number of particles N_i per unit of energy is given by:

$$\frac{dN_i(E,X)}{dX} = -\left(\frac{1}{\lambda_i} + \frac{1}{d_i}\right) N_i(E,X) + \sum_j \int \frac{F_{ji}(E_i,E_j)}{E_i} \frac{N_j(E_j,X)}{\lambda_j} dE_j. \tag{2.25}$$

The term λ_i is the interaction length and the decay length d_i describes the loss of particles due to collisions and decays. The second term refers to the gain of particles from interaction of other hadron species. $F_{ji}(E_i,E_j)$ is the dimensionless total cross section for a hadron of specie j and energy E_j to produce an outgoing hadron of species i, with the form:

$$F_{ji} = E_i \frac{dn_i(E_i,E_j)}{dE_i}, \tag{2.26}$$

where dn_i is the number of hadrons of type i produced in the energy range $E_i \pm dE_i$ The equations are solved for the fluxes of pions and kaons as a function of energy and slant depth under the following assumptions:

1. The primary cosmic ray spectrum can be described as a power law flux of protons and neutrons over all energies.
2. Interaction lengths are independent of energy.
3. All differential cross-sections follow Feynman scaling, i.e. can be written as:

$$F_{ji}(E_i/E_j) = F_{ji}(x_L). \tag{2.27}$$

4. The atmosphere is isothermal, i.e. its density decreases exponentially with altitude, and has no curvature.

The first assumption allows all fluxes to be factorized into parts which depend only on the energy or slant depth. The second and third points rewrite the cascade equation in terms of $x_L = E_i/E_j$

$$\frac{dN_i(E,X)}{dX} = -\left(\frac{1}{\lambda_i} + \frac{1}{d_i}\right) N_i(E,X) + \sum_j \int_0^1 \frac{F_{ji}(E,E/x_L) N_j(E/x_L,X)}{\lambda_j} \frac{dx_L}{x_L^2}. \tag{2.28}$$

The last point implies that the local density is a function of the slant depth X and zenith angle θ:

$$\rho = \frac{X cos\theta}{h_0}, \tag{2.29}$$

where h_0 is the scale height of the atmosphere, approximately 6.4 km. Since the decay length in g/cm^2 is proportional to the local density

$$d_i = c\beta\tau_i \frac{E_i}{m_i}\phi = \frac{c\tau_i}{h_0 m_i c^2} E_i X cos\theta = \frac{E_i}{\epsilon_i} X cos\theta, \tag{2.30}$$

where

$$\epsilon_i = \frac{h_0 m_i c^2}{c\tau_i}, \tag{2.31}$$

is called the critical energy. The ratio E/ϵ defines the relative importance of the decay term and interaction term in 2.28. If $E >> \epsilon$, the decay can be neglected and if $E << \epsilon$ it dominates. In the high energy limit, the pion flux is:

$$\Pi(E,X)_{E>>\epsilon} = N(E,0)\frac{Z_{N\pi}}{1-Z_{NN}}\frac{\Lambda_\pi}{\Lambda_\pi - \lambda_N}\left(e^{-X/\Lambda_\pi} - e^{-X/\Lambda_N}\right). \tag{2.32}$$

The Z_{ij} are the spectrum weighted moments of the inclusive cross-sections:

$$Z_{ij} = \int_0^1 (x_L)^{\gamma-1} F_{ij}(x_L) dx_L, \tag{2.33}$$

where γ is the integral spectral index of the primary cosmic rays. The Λ_i are the attenuation lengths $\Lambda = \lambda_i/1 - Z_{ii}$. In the opposite limit, where $E << \epsilon$, the pion flux gets a zenith dependence through the decay length, and the spectrum becomes harder than the primary spectrum by one power of E.

$$\Pi(E,X)_{E<<\epsilon} = N(E,0)\frac{Z_{N\pi}}{\lambda_N} e^{-X/\lambda_N}\frac{XEcos\theta}{\epsilon_\pi}. \tag{2.34}$$

Given the meson fluxes we can obtain the muons and neutrinos produced in their decays. The spectrum of the secondaries of species i is given by

$$\frac{dN_i(E,X)}{dX} = \sum_j Br(j \longrightarrow i)\int_{E_{min}}^{E_{max}} \frac{dn_{ij}(E,E')}{dE}\frac{N_j(E',X)}{d_i} dE', \tag{2.35}$$

where $Br(j \longrightarrow i)$ is the branching ratio of decay of particle j to final states that contain a particle i, $dn_{ij}(E,E')/dE$ is the spectrum of secondaries per decay. For 2-body decays $M \longrightarrow \mu\nu$, in the relativistic limit, this term is a constant:

$$\frac{dn}{dE_\nu} = \frac{dn}{dE_\mu} = \frac{1}{E_M(1-r_M)}, \tag{2.36}$$

where E_M is the lab frame energy of the parent meson M and $r_M = m_\mu^2/m_M^2$ is the squared ratio of the μ and the parents meson masses. The laboratory frame energies of

the secondary muons and neutrinos are limited by $0 \leq E_\nu \leq (1-r_M)E_M$ and $r_M E_M \leq E_\mu \leq E_M$. Inserting these limits and decay spectrum in Eq.(2.35), the spectrum of muon neutrinos from charged pion and kaons decays is

$$\begin{aligned}\frac{dN_\nu(E,X)}{dX} &= \frac{\epsilon_\pi}{Xcos\theta(1-r_\pi)}\int_{E_\nu/(1-r_\pi)}^{\infty}\frac{\Pi(E,X)}{E}\frac{dE}{E} \\ &+ \frac{0.635\epsilon_K}{Xcos\theta I(1-r_K)}\int_{E_\nu/(1-r_K)}^{\infty}\frac{K(E,X)}{E}\frac{dE}{E},\end{aligned} \tag{2.37}$$

where the Π and K are the fluxes of charged pions and kaons respectively, and we use the branching ratios $Br\,(\pi^\pm \longrightarrow \nu_\mu) = 1$ and $Br\,(K^\pm \longrightarrow \nu_\mu) = 0.635$. The neutrino flux at depth X can be obtained by integrating Eq. (2.37) from the top of the atmosphere. Taking the limit of large X and changing variables from E to $z = E/E_\nu$.

$$N_\nu = N_N(E_\nu)\left[\frac{Z_{N\pi}}{1-r_\pi}\xi_\pi(E_\nu)I_\pi(E_\nu) + 0.635\frac{Z_{NK}}{1-r_K}\xi_K(E_\nu)I_K(E_\nu)\right], \tag{2.38}$$

where $N_N(E_\nu)$ is the primary nucleon flux evaluated at E_ν, $\xi_i(E_\nu) = \epsilon_i/(E_\nu cos\theta)$ and

$$I_i(E_\nu) = \frac{\Lambda_i}{\lambda_N}\int_{1/(1-r_i)}^{\infty}\frac{dz}{z^{\gamma+2}}\left[\frac{1}{z+\xi_i(E_\nu)} - \frac{\Lambda_i/\Lambda_N - 1}{2z+\xi_i(E_\nu)} + \frac{(\Lambda_i/\Lambda_N-1)^2}{3z+\xi_i(E_\nu)+...}\right. . \tag{2.39}$$

Eq.(2.39) can be evaluated in the low and high energy limits to yield

$$I_i(E_\nu) = \left[\begin{array}{ll} \frac{1}{\gamma+1}\frac{\Lambda_N}{\lambda_N}(1-r_i)^{\gamma+1}\frac{1}{\xi_i(E_\nu)} & E_{\nu<<\epsilon_i} \\ \frac{1}{\gamma+2}\frac{\Lambda_N}{\lambda_N}(1-r_i)^{\gamma+2}\frac{\Lambda_i}{\Lambda_i-\Lambda_N}In\left(\frac{\Lambda_i}{\Lambda_N}\right) & E_{\nu>>\epsilon_i}. \end{array}\right. . \tag{2.40}$$

The low and high energy limits of (2.38) can be joined with an interpolation of the form

$$N_\nu(E_\nu) \approx \frac{N_N(E_\nu)}{1-Z_{NN}}\sum_i \frac{Br(i\longrightarrow\nu)A_{i\nu}}{1+B_{i\nu}cos\theta E_\nu/\epsilon_i}, \tag{2.41}$$

where

$$A_{i\nu} = Z_{Ni}\frac{(1-r_i)^\gamma}{\gamma+1}, \tag{2.42}$$

$$B_{i\nu} = \left(\frac{\gamma+1}{\gamma+2}\right)\left(\frac{1}{1-r_i}\right)\left(\frac{\Lambda_i-\Lambda_N}{\Lambda_i In(\Lambda_i/\Lambda_N)}\right). \tag{2.43}$$

The flux of muons from the same processes can be obtained by integrating Eq.(2.39) from 1 to $1/r_i$ instead from $1/(1-r_i)$ to ∞. The corresponding coefficients of the interpolation are:

$$A_{i\mu} = Z_{Ni}\frac{1-r_i^{\gamma+1}}{1-r_i}\frac{1}{\gamma+1}, \tag{2.44}$$

$$B_{i\mu} = \left(\frac{\gamma+1}{\gamma+2}\right)\left(\frac{1-r_i^{\gamma+2}}{1-r_i^{\gamma+2}}\right)\left(\frac{\Lambda_i-\Lambda_N}{\Lambda_i In(\Lambda_i/\Lambda_N)}\right). \tag{2.45}$$

That have to be evaluated for the pion and kaon respectively. The flux of muons from the same processes can be obtained by integrating Eq.(2.39) from 1 to $1/r_i$ instead of the last limits. Evaluating all the terms the conventional flux of atmospheric neutrinos takes the form:

$$\phi_{\nu_\mu} \approx 0.018 E_{\nu_\mu}^{-2.7}\left[\frac{1}{1+\frac{2.77 cos\theta E_{\nu_\mu}}{115\,GeV}} + \frac{0.367}{1+\frac{1.18 cos\theta E_{\nu_\mu}}{850\,GeV}}\right]. \tag{2.46}$$

In a similar analysis we can approximate the contribution of the charmed mesons and obtain the final formula [26] :

$$\phi_{\nu_\mu} \approx 0.018 E_{\nu_\mu}^{-2.7}\left[\frac{1}{1+\frac{2.77 cos\theta E_{\nu_\mu}}{115\,GeV}} + \frac{0.367}{1+\frac{1.18 cos\theta E_{\nu_\mu}}{850\,GeV}} + \frac{1.4\times10^{-3}}{1+\frac{0.14 cos\theta E_{\nu_\mu}}{5\times10^7\,GeV}}\right]. \tag{2.47}$$

2.4 Maximum Likelihood Method

2.4.1 Maximum Likelihood Function

This method is very useful in estimate the parameters in physical processes; an extended information about Maximum Likelihood are in [27, 28]. Briefly is introduced the basic ideas of the method.

For a data set D and a model (that depends of the variables $\mathbf{x}$) M($\mathbf{x}$) , the likelihood of the model is the probability of obtain the data set if the model is true:

$$L(M(\mathbf{x})) = P(D|M(\mathbf{x})). \tag{2.48}$$

The ratio of two likelihood values help us to determine which of the two models is more likely to be correct. Thus the values of $\mathbf{x}$ which maximizes the likelihood function is taken to be the estimate of the true value, and if faster the likelihood function falls off the maximum, smaller the confidence regions will be. Is more common to work with the logarithm of the likelihood, which makes the calculations easier. Then the quantity that compares two models is:

$$T = InL(M(\mathbf{x_1})) - InL(M(\mathbf{x_2})). \tag{2.49}$$

The estimation have to be:
a)Consistency: the estimator converges to the true value as more data are accumulated.
b)Efficiency: The rate at which the estimator converges to the true value. If this is equal to the Rao-Cramèr-Frechet bound (the maximum rate of convergence), the estimator is said to be efficcient [27].
c)Bias: the expectation of the difference of the estimator and the true value.
d)Robustness: The insensitivity of the estimator to errors in the assumed probability distributions.

It is proved [28] that if a consistent, efficient estimator exists, then the Maximum Likelihood estimate is also consistent and efficient. The Maximum Likelihood estimate may be biased, however, it and its robustness depend on the models used.

2.4.2 Wilks' Theorem

If the model M($\mathbf{x_0}$) (the Null model) is correct, and the maximum likelihood value obtained by the k parameters of $\mathbf{x}$ to vary is $L(\mathbf{x_M})$, then the statistics:

$$T = 2[InL(M(\mathbf{x_M})) - InL(M(\mathbf{x_0}))]. \tag{2.50}$$

is asymptotically distributed like $\chi^2(k)$ as the size of the data set increases.

2.5 Effective Areas for Muon Neutrino

The neutrino effective area for a muon neutrino is defined so that the product of the neutrino flux multiplied by the effective area gives the event rate.

$$\frac{dN_{\nu_\mu}}{dt} = \int_{E_{\nu_\mu}} \int_{\Omega} A_{eff}(E_{\nu_\mu}, \delta) \frac{d^2\phi}{dE_{\nu_\mu} d\Omega}(E_{\nu_\mu}, \delta) d\Omega dE_{\nu_\mu}, \tag{2.51}$$

The neutrino effective area is [29]:

$$A_{eff}(\delta, E_{\nu_\mu}) = \epsilon(\delta) A(\delta) P(E_{\nu_\mu}, E_{\mu,min}) e^{-\sigma_{\nu_\mu} N_A X(\delta)}. \tag{2.52}$$

where ϵ is the efficiency for a detector of projected area $A(\delta)$ to detect a muon incident at zenith angle δ. The exponential express the muon attenuation in the Earth for angle δ

below the horizon, where $X(\delta)$ is the amount of matter (g/cm^2) along the chord through the Earth. And the term $P(E_{\nu_\mu}, E_{\mu,min})$ is the probability that a muon neutrino on a trajectory that will intercept the detector gives a visible muon in the detector, and $E_{\mu,min}$ is the minimum energy required upon entering the detector for the event to be reconstructed well.

The way to obtain the effective areas in general is complex and is necessary to use many applications with simulations of the detector. Fortunately for many arrangements the detectors publish the effective areas. For example we show in fig. (2.2) the effective areas for the detector IceCube 79 string configuration.

The probability density function for the background and for an external isotropic flux (proportional to $E^{-\alpha}$, $\alpha \geq 2$) are very difficult to obtain for the collaborations, because in general are not public. Also we can calculate this probabilities in base of the samples of experimental data but in the majority of times are incomplete for the final reports; but is the opposite case for the effective areas. We can construct the probabilities in base of this information as follows:
a) We calculate the total event rate for a range of energy of measurements for the detector (for example for the 79 string configuration between 10^2 and 10^9 GeV) for a declination range (for example 80^o) with their respective effective area (for example $-90^o \leq \delta \leq -60^o$ effective area); and we call this value thenumber A
b)Then calculate the same rate but for the range $E \pm \Delta E^*/2$ where E^* is a small energy range around E; being the number B.
c)The probability density function $PDF(\theta, E_{\nu_\mu})$ for the region $E \pm \Delta E^*/2$ and for the angle chosen is finally:

$$PDF(\theta, E_{\nu_\mu}) = B/A. \tag{2.53}$$

Where in the division is eliminated the angular differential of the integrals. And the PDF is calculated with the initial flux that could be astrophysical of background origin.

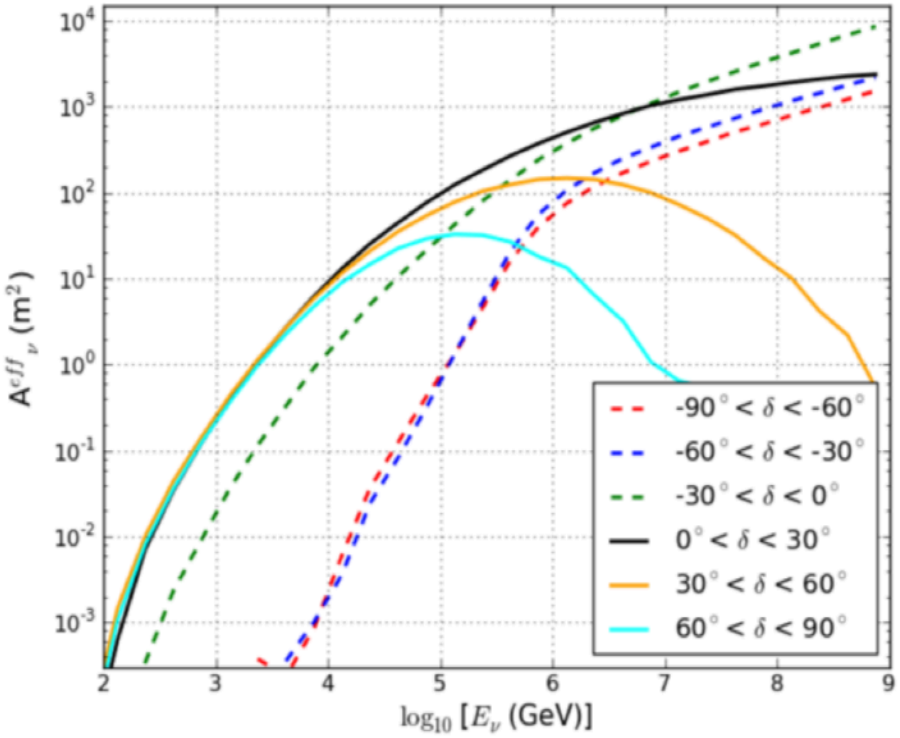

Figure 2.2: Effective Areas for IceCube 79 string configuration [30].

Chapter 3

Problems

It took many years to construct a detector like Icecube which has the ability to detect neutrinos in the range of GeV and higher energies. The atmospheric background has a natural cut of energy of approximately 100 TeV; in consequence was enthusiastically awaited the data runs expecting that they will show evidence of extraterrestrial neutrinos; and fortunately that was the case. In the first part of the chapter it is described the results of the seasons of 79 and 86 strings and the challenges to explain them.
The object Mrk 421 is the closest AGN to the Earth and also is the first extragalactic source that was corroborated that emits in the TeV energy range. In particular this blazar was a multi-TeV emission in 2004 with a not clear counterpart in the low energy range expected to be part of a general leptonic emission. The phenomena constitutes a puzzle for the leptonic model. A description of the flaring is in the last section of the chapter. The two very interesting problems are the motivation of this work.

3.1 Observation of TeV-PeV events with Icecube detector

In November 2012, the IceCube Collaboration announced the detection of two showerlike events with energies slightly above 1 PeV by analyzing the data taken during May 2010 - May 2012 [31]. These data were obtained using the 79 strings configuration and the completed 86 strings configuration with a total combined live time of 662 days. A follow-up analysis of the same data published in November 2013, revealed additional 26 events in the energy range $\sim$ 30 TeV - 250 TeV [32]. Reconstruction of these events shows

that 21 events are showerlike, mostly caused by ν_e and ν_τ and 7 are muon track events. These 28 events have flavors, directions and energies inconsistent with those expected from the atmospheric muon and neutrino backgrounds and this is the first indication of extraterrestrial origin of high energy neutrinos. The track events have uncertainty of the order of one degree in their arrival directions and the angular resolution for the 21 shower events is poor, ranging from$\sim 10^\circ$ to $\sim 50^\circ$. The IceCube analysis ruled out any spatial clustering of the events. The third year (2012-2013) data analysis revealed additional 9 events of which two are track events and the rest are shower events [33]. The event 35 is the most energetic one so far observed. In the full 988-day data, the muon background is expected to be 8.4 ± 4.2 events and the atmospheric neutrino is $6.6^{+5.9}_{-1.6}$ events. Five events 3, 8, 18, 28 and 32 are of down going muons and are consistent with the expected background muon events type. The reports show that the IceCube events are predominantly shower events. The total data with a live time of 988 days, contains a total of 37 neutrino candidate events with deposited energies ranging from 30 TeV to 2 PeV. The observed energy distribution extends to much higher than the expected from the π/K atmospheric neutrino background, which has been measured up to 100 TeV. While a harder spectrum is expected from atmospheric neutrinos produced in charmed meson decay, this probability is constrained by the observed angular distribution. If it was the case such neutrinos are produced also isotropically, but approximately half of those in the southern hemisphere are produced with muons of high energy to reach IceCube and trigger the muon veto. These results in a southern hemisphere charm rate will be $\sim$50% smaller than the northern hemisphere rate, with larger ratios near the poles. The data show no evidence of such a suppression. At the same time for equal neutrino fluxes of flavors (1,1,1), ν_μ CC events make 20% of the interactions. The data fit very well to a combination of background muons, atmospheric neutrinos from π/K decay, atmospheric neutrinos from charmed meson decay, and a isotropic 1:1:1 astrophysical flux which is given in fig. (3.1). As it is anticipated, the atmospheric neutrinos up to TeV energies exhibit a muon flavor dominance but the IceCube result contradicts this property and is consistent with equal fluxes of all the three flavors. For an external E_ν^{-2} spectrum the best fit diffuse flux obtained by IceCube per flavor is $F_\nu = (0.95 \pm 0.3) \times 10^{-8}\, GeV\, cm^{-2}\, s^{-1}\, sr^{-1}$ which is consistent with the Waxman-Bahcall bound [34]. The best fit atmospheric only alternative model, however, would require a charm normalization 3.6 times higher than their current 90% CL upper limit. Even this extreme scenario is disfavored by the energy and angular distributions of the events at 5.7σ using a likelihood ratio test. All the details

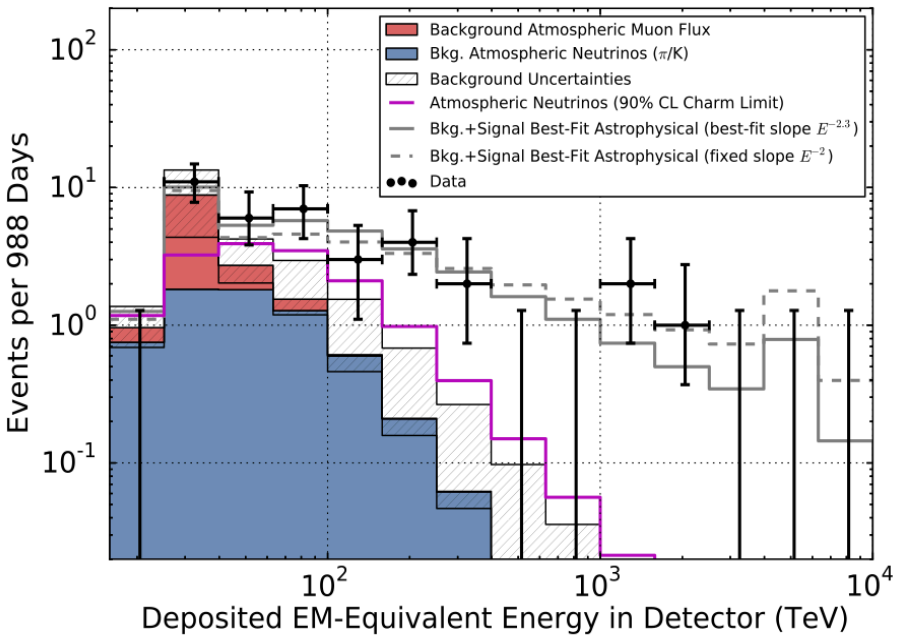

Figure 3.1: Deposited energies of observed events with predictions. The hashed region shows uncertainties on the sum of all backgrounds.

about the observed 37 events is shown in the table (3.1) and these events are also shown in the sky map with equatorial coordinates in fig. (3.2).

Observation of these neutrinos triggered a lot of excitement to understand their origin and production mechanism. While interpreting these events in terms of astrophysical models seems challenging, several possible galactic and extra galactic sources have been discussed which includes, Galactic center [35], γ-ray bursts (GRBs) [36], active galactic nuclei (AGN) [37], high energy peaked blazars (HBLs) [38, 39], starburst galaxies [40] etc. In Ref. [39] many positional correlations of BL Lac objects and galactic pulsar wind nebulae with the IceCube events are shown. It is also very natural to expect that these neutrinos might come from diverse sources having different production mechanisms and different power-law and this information can probably be extracted from the directionality of the observed neutrino events. The largest concentration of 7 events are around the Galactic center and also clustering of the events could be associated to the Norma arm of the Galaxy [41]. As the statistics is too sparse, it is premature to draw any conclusion regarding the galactic origin of these events. There are also nonstandard physics interpretations of these events [42, 43].

ID	Energy	Time	Dec	R.A.	MAE	Type
1	$47.6^{+6.5}_{-5.4}$	55351.3222143	-1.8	35.2	16.3	Shower
2	117^{+15}_{-15}	55351.4659661	-28.0	282.6	25.4	Shower
3	$78.7^{+10.8}_{-8.7}$	55451.0707482	-31.2	127.9	≤ 1.5	Track
4	165^{+20}_{-15}	55477.3930984	-51.2	169.5	7.1	Shower
5	$71.4^{+9.0}_{-9.0}$	55512.5516311	-0.4	110.6	≤ 1.2	Track
6	$28.4^{+2.7}_{-2.5}$	55567.6388127	-27.2	133.9	9.8	Shower
7	$34.3^{+3.5}_{-4.3}$	55571.2585362	-45.1	15.6	24.1	Shower
8	$32.6^{+10.3}_{-11.1}$	55608.82011315	-21.2	182.4	≤ 1.3	Track
9	$63.2^{+7.1}_{-8.0}$	55685.6629713	33.6	151.3	16.5	Shower
10	117^{+15}_{-15}	55351.4659661	-28.0	282.6	25.4	Shower
11	$88.4^{+12.5}_{-10.7}$	55714.5909345	-8.9	155.3	16.7	Shower
12	104^{+13}_{-13}	55739.4411232	-52.8	296.1	9.8	Shower
13	253^{+26}_{-22}	55756.1129844	40.3	67.9	≤ 1.2	Track
14	1041^{+132}_{-144}	55782.5161911	-27.9	265.6	13.2	Shower
15	$57.5^{+8.3}_{-7.8}$	55783.1854223	-49.7	287.3	19.7	Shower
16	$30.6^{+3.6}_{-3.5}$	55798.6271285	-22.6	192.1	19.4	Shower
17	200^{+27}_{-27}	55800.3755483	14.5	247.4	11.6	Shower
18	$31.5^{+4.6}_{-3.3}$	55923.5318204	-24.8	345.6	≤ 1.3	track
19	$71.5^{+7.0}_{-7.2}$	55925.7958619	-59.7	76.9	9.7	Shower
20	1141^{+143}_{-133}	55929.3986279	-67.2	38.3	10.7	Shower
21	$30.2^{+3.5}_{-3.3}$	55936.5416484	-24.0	9.0	20.9	Shower
22	220^{+21}_{-24}	55941.9757813	-22.1	293.7	12.1	Shower
23	$82.2^{+8.6}_{-8.4}$	55949.5693228	-13.2	208.7	≤ 1.9	Track
24	$30.5^{+3.2}_{-2.6}$	55950.8474912	-15.1	282.2	15.5	Shower
25	$33.5^{+4.9}_{-5.0}$	55966.7422488	-14.5	286.0	46.3	Shower
26	210^{+29}_{-26}	55979.2551750	22.7	143.4	11.8	Shower
27	$60.2^{+5.6}_{-5.6}$	56008.6845644	-12.6	121.7	6.6	Shower
28	$46.1^{+5.7}_{-4.4}$	56048.5704209	-71.5	164.8	≤ 1.3	Track
29	$32.7^{+3.2}_{-2.9}$	56108.2572046	41.0	298.1	7.4	Shower
30	129^{+14}_{-12}	56115.7283574	-82.7	103.2	8.0	Shower
31	$42.5^{+5.4}_{-5.7}$	56176.3914143	78.3	146.1	26.0	Shower

32	——	56211.7401231	——	——	——	Coincident
33	385^{+46}_{-49}	56221.3424023	7.8	292.5	13.5	Shower
34	$42.1^{+6.5}_{-6.3}$	56228.6055226	31.3	323.4	42.7	Shower
35	2004^{+236}_{-262}	56265.1338677	-55.8	208.4	15.9	Shower
36	$28.9^{+3.0}_{-2.6}$	56308.1642740	-3.0	257.7	11.7	Shower
37	$30.8\ ^{+3.3}_{-3.5}$	56390.1887627	20.7	167.3	≤ 1.2	Track

Table 3.1: Properties of the objects. In the first column the number of event, in the second the energy detected in TeV, in the third is the time of detection in the MJD system, the next two columns are the declination and right ascension in equatorial coordinates, and the last two are the median angular error of each event in grades and the type of event (shower or track) respectively. Events 28 and 32 have coincident hits in the IceTop surface array, implying that they are almost certainly produced in cosmic ray air showers.

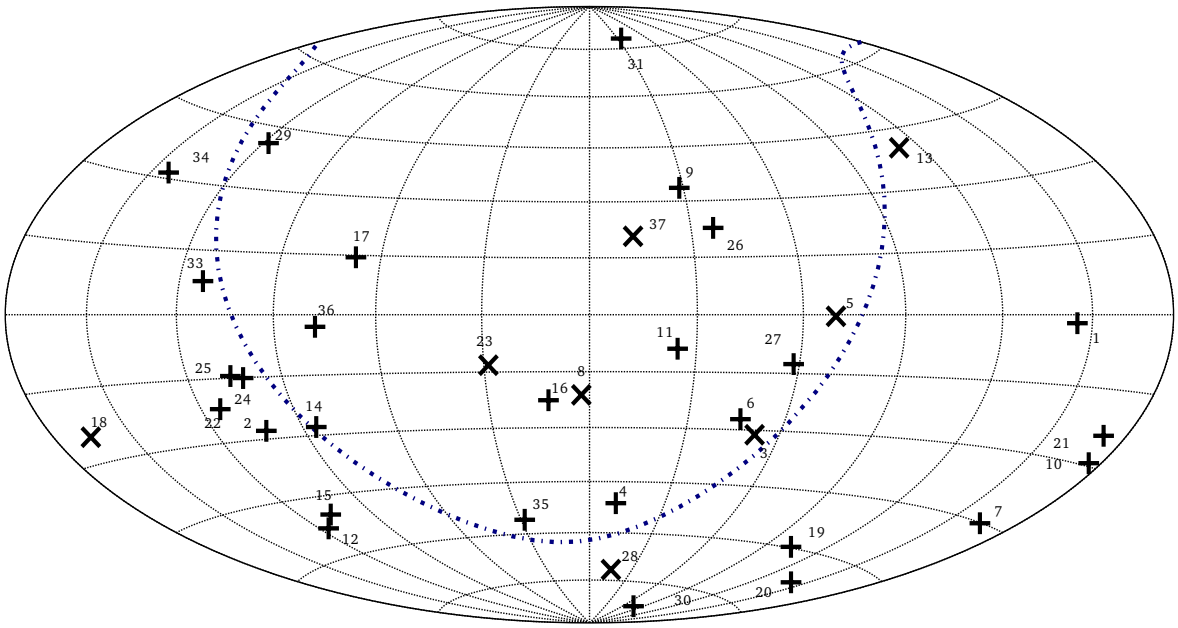

Figure 3.2: The sky map is shown in the equatorial coordinates with the 37 IceCube events. Here + are shower events and × sign are track events. The dotted line is the galactic plane.

3.1.1 Candidates

Blazars, due to their multi-TeV emission, are long believed to be sources of ultra high energy cosmic rays (UHECRs) [38,39,44]. These are extragalactic objects characterized by relativistic jets with a small viewing angle with respect to the line of sight and are powered by a supermassive black hole in the center of their respective galaxy. These objects are also efficient accelerators of particles through shock or diffusive Fermi acceleration processes with a power-law spectrum given as $dN/dE \propto E^{-\alpha}$, with the power index $\alpha \geq 2$ [45]. Protons can reach ultra high energy through the above acceleration mechanisms. Fractions of these particles escaping from the source can constitute the UHECRs arriving on Earth. These objects also produce high energy γ-rays and neutrinos through pp and/or $p\gamma$ interactions [46]. The online catalog for TeV astronomy (**TeVCat**) [47] gives a list of objects which have emitted in multi-TeV γ-rays and many HBLs are there in the list. In the context of photohadronic scenario, these multi-TeV gamma rays will be accompanied by multi-TeV neutrinos. So it is natural to look for neutrino events from these blazers. Few years ago, Pierre Auger (PA) collaboration reported two UHECR events above 57 EeV within 3.1° around Cen A a FR-I galaxy in the local Universe. So this can also be a potential candidate to look for high energy neutrino events in IceCube detector.

Recently ANTARES collaboration presented a time dependent analysis [48] to look for muon tracks using the data taken during the period August 2008 to December 2012. The collaboration selected 41 flaring blazars from the Fermi-LAT and TeV γ-ray sources observed by ground based telescopes H.E.S.S, MAGIC and VERITAS respectively. These selected blazars have significant time variability and having the flux $> 10^{-9}$ photons $cm^{-2}\,s^{-1}$ for the γ-ray energy above 1 GeV. They have also selected seven TeV flaring objects reported by H.E.S.S., MAGIC and VERITAS telescopes with the expectation that the TeV γ-rays may be correlated with the neutrino events. From the 41 Fermi blazar list, 33 are FSRQs, 7 are BL Lacs and one is unknown. Similarly from the list of 7 TeV flaring blazars one is FSRQ and six are HBLs. We are looking for FSRQs and HBLs like probable sources of very high energy neutrinos and can be also possible sources for some of the IceCube event. In this analysis the most significant correlation was found with a GeV flaring blazar from the Fermi-LAT catalog. However, the post-trial probability estimate shows that the event was compatible with background fluctuations.

Therefore, we focus our analysis on these candidate sources (mostly HBLs and FSRQs)

to find out how the IceCube events with the desired energies can be produced through photohadronic interaction within the core region of the emanating jets.

3.2 Flaring Blazars

As discussed in the introduction, flaring is the major activity of blazars and has been observed in many of them by Imaging Atmospheric Cherenkov Telescopes (IACTs). One of the nearest HBL, Markarian 421 (Mrk 421 or Mkn 421) underwent TeV flaring in the year 2004 and it was and simultaneously observed in X-rays and TeV energy. It was observed that the TeV outbursts had no counterparts in the lower energy range during flaring, which implies that this might be an orphan flare like the one observed in the HBL 1ES 1959+650 on 4th June 2002. The orphan flaring challenges the leptonic scenario for its interpretation in the multi-TeV energy range. Previously the orphan flaring of 1ES 1959+650 is studied using the photohadronic scenario by Sahu et al. The flaring of Mrk 421 gives us another opportunity to test the photohadronic scenario. In the last section is discussed Mrk 421 and its multiwavelength observation during the flaring in the year 2004.

3.3 2004 flaring activity of Markarian 421

Mrk 421 is a high synchrotron peaked BL Lac object (HBL) with equatorial coordinates R.A. 166.01°, Dec. 38.19°, and is the first extragalactic source (with a redshift of z=0.031) to be discovered as a VHE gamma-ray source [49]. It has a luminosity distance d_L of about 129.8 Mpc. Its central supermassive black hole is assumed to have a mass of $M_{BH} \simeq (2-9) \times 10^8 \, M_\odot$ corresponding to a Schwarzschild radius of $(0.6-2.7) \times 10^{14}$ cm and the Eddington luminosity $L_{Edd} = (2.5-11.3) \times 10^{46} \, erg \, s^{-1}$. The synchrotron peak of its SED is in the soft to medium X-ray range and the SSC peak is in the GeV range. It is one of the fastest varying γ-ray sources. In the past through dedicated multi wavelength observations, the source has been studied intensively by most TeV experiments, including H.E.S.S, MAGIC and VERITAS. A period of very strong activity was reported in 2000/2001. Extensive multi wavelength campaigns were useful to learn more about the SED and the spectral correlations of Mrk 421. The results showed positive but complex correlation between X-rays and gamma rays which challenges both the simple

one-zone leptonic model and the hadronic model. Also modeling of data during different states indicated that the one zone SSC model is insufficient to describe the observations. With the launch of the Fermi satellite in 2008 the observational gap at energies between 0.1 MeV and 0.3 TeV was filled. However, a one-zone SSC model explains the observed average SED reasonably well [50] as shown in fig. (3.3) . Several flares were observed in the 2003/2004 season. From February 2003 to June 2004, Mrk 421 was observed at TeV energies with the Whipple 10 m telescope (on Mt. Hopkins, USA) The average observational run was 28 minutes (but more runs were taken on occasions). During April 2004, a large flare took place both in the X-rays and the TeV energy band. The flare lasted for more than two weeks (from MJD 53104 to roughly MJD 53120). But due to a large data gap between MJD 53093 and 53104, it is difficult to exactly quantify the duration. To take data in both TeV band and X-ray band, Whipple worked simultaneously with the Rossi X-ray Timing Explorer (RXTE). It was also observed simultaneously in radio and optical wavelengths. The optical data were obtained with the Fred Lawrence Whipple Observatory (FLWO) 1.2m telescope (located adjacent to the Whipple 10 m gamma ray telescope on Mt. Hopkins) and with the 0.4 m telescope at the Bolwood Observatory in Stittsville, Ontario, Canada. For the radio observations they used the 26 m telescope at the University of Michigan Radio Astronomy Observatory (UMRAO) and the 13.7 m Metsähovi radio telescope at the Helsinski University of Technology. During the flaring it was observed that, the TeV flares had no coincident counterparts at longer wavelengths. Also it was observed that the X-ray flux reached its peak 1.5 days after the TeV flux did during this outburst. So it is possible that, the TeV flare might not be a true orphan flare like the one observed in 1ES 1959+650. On the other hand remarkable similarities between the orphan TeV flare in 1ES 1959+650 and Mrk 421 were observed, including similar variation patterns in X-rays. We use the flaring model of Sahu et al. to study this multi-TeV flaring event of Mrk 421.

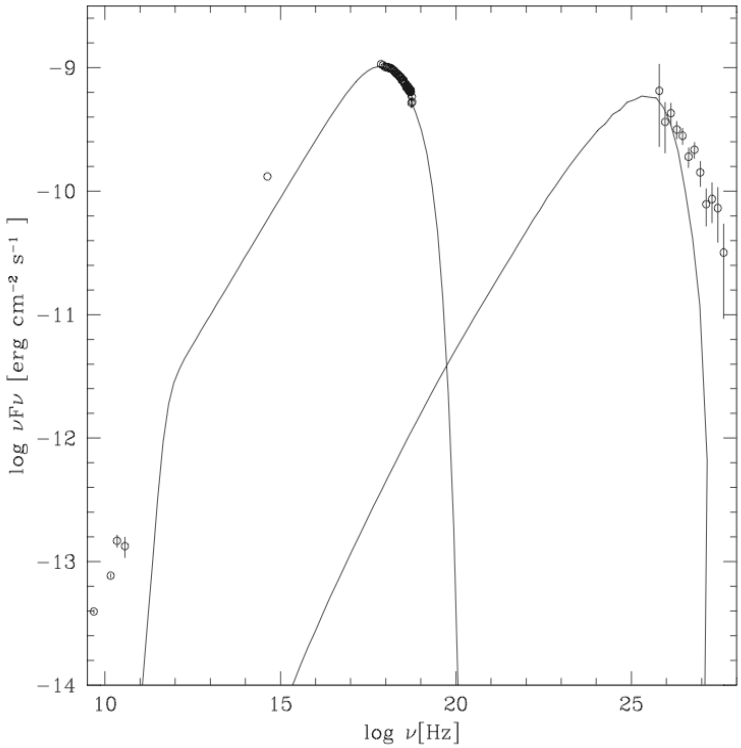

Figure 3.3: Spectral energy distribution of Mrk 421. It was derived from the high flux data. The solid line shows the best fit to the data with a one zone SSC model: δ=14, B=0.26 G, R=0.7×10^{16} cm, w_e=0.086 erg cm^{-3}, p_1=2.05, p_2=3.4,log(E_b)=11.0, log(E_{min})=6.5 and log(E_{max})=11.6. All the energies in eV.

Chapter 4

Results

In this Chapter the results of the work done are discussed in detail with a summary and outlook to each individual work.

The IceCube Collaboration has observed 37 neutrino events in the energy range of $30\,TeV \leq E_\nu \leq 2$ PeV and the sources of these neutrinos are unknown. Explaining these events in terms of astrophysical models is challenging. In two publications we have shown that some of the IceCube events are spatially correlated with some HBLs. In the first paper we have shown that 12 HBLs and one FR-I galaxy (Cen A) have positional correlation with 10 IceCube events of the 41 TeV HBL from TeVCat [47] plus Cen A. Recently ANTARES collaboration analyzed 41 flaring blazars to look for muon neutrinos. We use the same list of blazars also to look for a possible correlation with the IceCube neutrino events in a second publication. The results and analysis of these are discussed in detail.

The high energy blazar Mrk 421 underwent multi-TeV flaring during April 2004 and simultaneous observation were made in X-ray and TeV energies. It was observed that the VHE emission had no lower energy counterparts, which can probably be an orphan flaring. It is well known that leptonic model has difficulties in explaining the orphan flaring. In a third paper we used the photohadronic model developed by Sahu et al. to explain this multi-TeV flaring.

The results of these three articles are discussed in the same order as mentioned above, and in each section with the reference of the published article at the end of the title.

4.1 Possible sources of IceCube TeV-PeV events [44]

For our analysis we assume that the TeV-PeV neutrinos are produced from the photohadronic interaction ($p\gamma$) in the inner jet region of the HBL where the background photon density $n'_{\gamma,f}$ in the SSC region is high. We found coincidence in the positions of 12 HBLs and one radio galaxy, Cen A within the error circles of 10 IceCube events. These objects are taken from the online catalog TeVCat [47] and are observed in multi-TeV γ-rays. However, the redshift, Lorentz factor and doppler factor of some of these HBLs are not yet known. So whichever HBL has known z, Γ, δ, SED and lies within the error circle of the IceCube event, we calculate the seed photon energy ϵ_γ necessary to produce the desired neutrino energy E_ν through photohadronic interaction with the eq. (2.9). The events 25 and 34 have very large errors $> 40^\circ$, so we neglect these two events from our analysis. For the calculation of $n'_{\gamma,f}$, first we estimate the radius of the inner blob R'_f, which will satisfy the restriction $R_s < R'_f < R'_b$, where $R_s = 2G_N M_{BH}/c^2$ is the Schwarzschild radius of the central black of mass M_{BH}. The R'_b is obtained from the leptonic model used to fit to the objects SED. The values of R'_f and R'_b for the objects are shown in table (4.1). We assume a very conservative 1% energy loss of the UHE protons in the inner blob on the dynamical time scale t'_d which corresponds to a optical depth of $\tau_{p\gamma} \sim 0.01$ and consequently $n'_{\gamma,f} \sim 2 \times 10^{10}\, R'^{-1}_{f,15}\, cm^{-3}$. The proton in the inner jet region has maximum energy $E_{p,max} \sim 3 \times 10^{17} (B'_f/G) R'_{f,15}\, eV$, where B'_f is the commoving magnetic field, which is higher than the outer region. For all neutrino flavors α we assume a power-law spectrum of the form

$$J_{\nu_\alpha}(E_\nu) = A_{\nu_\alpha} \left(\frac{E_\nu}{100\, TeV} \right)^{-\kappa}, \tag{4.1}$$

where 100 TeV is the point of normalization and the neutrino flux can be given as [51]

$$F_\nu = \sum_\alpha \int_{E_{\nu 1}(1+z)}^{E_{\nu 2}(1+z)} dE_\nu E_\nu J_{\nu_\alpha}(E_\nu). \tag{4.2}$$

The normalization constant A_{ν_α} is given by

$$A_{\nu_\alpha} = \frac{1}{3} \frac{N_\nu}{T \Sigma_\alpha \int_{E_{\nu_1}}^{E_{\nu_2}} dE_\nu A_{eff,\alpha}(E_\nu) \left(\frac{E_\nu}{100 TeV}\right)^{-\kappa}}, \tag{4.3}$$

where N_ν is the number of neutrino events and $A_{eff,\alpha}$ is the effective area for different neutrino flavors. The time period $T = 988$ days is used [32] for the calculation of normalization constant. The integration limit is from 25 TeV to 2.2 PeV [51] and κ

is the spectral index. All the 37 IceCube events with their individual error circles in equatorial coordinates are shown in the sky map in fig. (1). The 12 HBLs and the Cen A are within the error circles of 10 IceCube events which are also shown in the sky map. In table (4.1), we have summarized all the relevant parameters of these 13 objects. All the correlated IceCube events are shower events with sub-PeV energies and the event 35 which is the only PeV event with $E_\nu \simeq 2$ PeV. Except the HBL, KUV00311-1993 [47], all others have their z, Γ and δ measured/fitted and SEDs are calculated from the leptonic model. For most of the objects ϵ_γ lies between the synchrotron peak energy and the forward falling tail of synchrotron energy with the exception of RGBJ0192+017 [52] and 1ES1011+496 [53]. In these two HBLs ϵ_γ lies in the beginning of the SSC spectrum and the values are 179 keV and 69 keV respectively. The corresponding photon densities and the neutrino fluxes are shown in table (4.1). Our estimate of $n'_{\gamma,f}$ is based on the assumption of 1% energy loss of the UHECR proton for all the HBLs/AGN. We observed that by varying κ between 2.2 and 3.08 we found a small variation is the neutrino flux. At the end we fix its value to 2.2.

Object (Dec,RA);z,δ	ID	$\frac{E_\nu}{TeV}$	$\frac{\epsilon_\gamma}{keV}$	$R'_{f,15}$	$R'_{b,15}$	$n'_{\gamma,f,10}$	$F_{\nu,-9}$	$\delta\chi^2$
RGBJ0152+017 [52]	1	47.6	179.	0.9	1.5	2.2	2.41	0.24
(1.77,28.14);0.08,25								
H2356-309 [54]	7	34.3	111.	0.5	3.4	4.0	2.38	0.66
(-30.62,358.79); 0.165, 18	10	97.2	39.					0.47
	21	30.2	125.					0.29
SHBLJ001355.9 [55]	21	30.2	45.	1.0	35.	2.0	2.41	0.13
(-18.89,3.46);0.095,10								
KUV00311-1938	21	30.2	-	-	-	-	-	0.05
(-19.35,8.39);-,-								
Mrk421 [15]	9	63.2	46.	3.0	7.0	0.7	2.43	0.61
(38.19,166.01); 0.031, 14								
1ES1011+496 [53]	9	63.2	69.	5.0	10.	0.4	2.36	0.94
(49.43,153.77);0.212,20								
PKS2005-489 [56]	12	104.	31.	5.0	400.	0.4	2.42	0.33
(-48.83,302.36);0.071,15	15	57.5	53.					0.25

PG1553+113 [57]	17	200.	50.	3.0	10.	0.7	2.29	0.59
(11.19,238.94);0.4,35								
Mrk180 [64]	31	42.5	34.	5.0	20.	0.4	2.43	0.18
(70.16,174.11);0.045,10								
1ES0502+675 [65]	31	42.5	35.	5.0	10.	0.4	2.31	0.66
(67.62,76.98);0.341,13								
RGBJ0710+591 [66]	31	42.5	267.	5.0	20.	0.4	2.39	0.77
(59.15,107.61);0.125,30								
1ES1312-423 [61]	35	2004.	0.32	5.0	240.	0.4	2.40	0.85
(-42.6,198.75);0.105,7.								
Cen A (FR-I) [21]	35	2004.	0.056	0 .6	3.0	3.3	2.45	0.73
(-43.01,201.36);.00183,1								

Table 4.1: The objects HBLs/AGN are shown in first column which are in the error circles of the IceCube events ID (second column). Below each object we also put their coordinates, Declination and Right Ascension (Dec, RA) in degree, redshift (z) and the Doppler factor (δ). In the third and the fourth columns the observed neutrino energy E_ν/TeV and the corresponding seed photon energy ϵ_γ/keV are given. In fifth and the sixth columns the radius of the inner blob R'_f and the outer blob R'_b are given in units of $R' = 10^{15}R'_{15}\,cm$. The seed photon density in the inner blob $n'_{\gamma,f}$ in units of $n'_{\gamma,f} = 10^{10}\,n'_{\gamma,f,10}\,cm^{-3}$ is given in the seventh column and diffuse neutrino flux F_ν in units of $F_\nu = 10^{-9}\,F_{\nu,-9}\,GeV\,cm^{-2}\,s^{-1}\,sr^{-1}$ is given in the eighth column. In the last column we have shown the $\delta\chi^2$ value for each event defined in the next section. The reference to each object is given in the first column.

The HBL, H2356-309 [54] is within the error circles of three IceCube events 7, 10 and 21 and their corresponding synchrotron energies, $n'_{\gamma,f}$ and neutrino flux are shown in table (1). Another two HBLs, SHBLJ001355.9 [55] and KUV00311-1938 are also within the error circle of the event 21 and SHBLJ001355.9 has the corresponding synchrotron energy $\epsilon_\gamma \simeq 45$ keV. The blazar PKS2005-489 [56] is in the error circles of the events 12 and 15, and to produce these neutrino events the photon energy is in the range 30 keV-53 keV which is near the synchrotron peak and the corresponding proton energy is in the range $1.2\,PeV \leq E_p \leq 2.1\,PeV$. These two events are also spatially correlated with the Fermi bubble. The event 17 has a mean energy of 200 TeV and is correlated with the HBL, PG1553+113 [57] and is the farthest one in our list with a redshift of $z = 0.4$. The $n'_{\gamma,f}$ and neutrino fluxes for PKS2005-489 and PG1553+113 are shown in table 4.1.

Very recently the Telescope Array (TA) observed an UHECR hotspot above 57 EeV in a region within 20° radius circle centered at RA= 146.7° and Dec. = 43.2° [58], the shaded closed counter in the sky map in fig. (1). This region correlates with three neutrino events 9, 26 and 31. We found three HBLs: Mrk 180, 1ES0502+675 and RGBJ0710+591 within the error circle of the IceCube event 31. Interestingly, positions of two blazars, Mrk 421 [15] and 1ES1011+496 [53] are also simultaneously within the error circle of the IceCube event 9 and within the TA hotspot [39, 59]. The required E_p and ϵ_γ for Mrk 421 are 1.3 PeV and 46 keV respectively. The photon density and F_ν are shown in table (1). Similarly for 1ES1011+496 also we have shown the $n'_{\gamma,f}$ and F_ν.

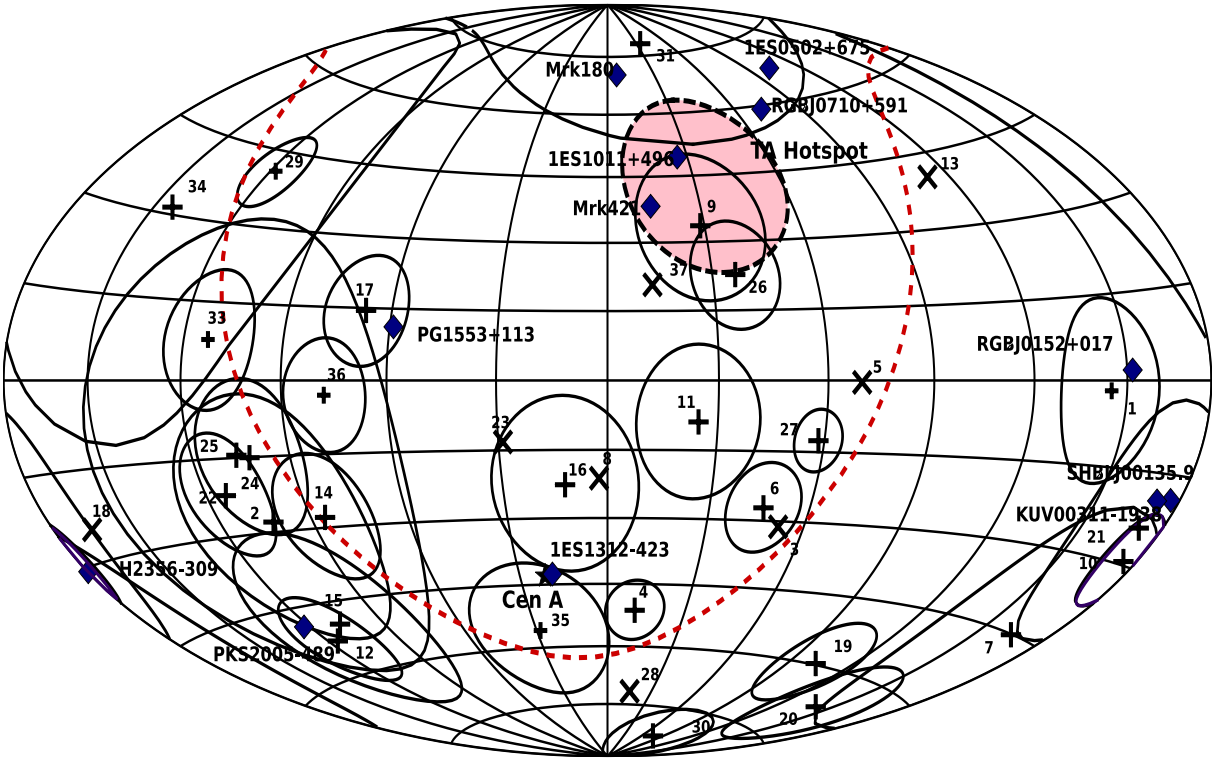

Figure 4.1: The sky map is shown in the equatorial coordinates with the 37 IceCube events and their individual errors (only for shower events). Here + are shower events and × sign are track events with their corresponding event ID. We have also shown the positions of the HBLs with their names which are within the error circle of the IceCube events.The TA hotspot is shown as a shaded closed contour and the galactic plane is shown as a dashed line. A simple program base for these maps is in section(5.1)

Cen A is the nearest active radio galaxy and for long time has been proposed as the source of UHECRs. Few years ago Pierre Auger (PA) Collaboration reported two UHECR events above 57 EeV within 3.1° around Cen A [60]. Its position coincides within the error

circle of the IceCube event 35 having the highest neutrino energy of 2 PeV so far observed by IceCube. In terms of the hadronic model discussed above the 2 PeV neutrino energy corresponds to a proton energy of ~ 40 PeV and the seed photons energy is $\epsilon_\gamma \sim 56$ eV which is in the valley formed by the synchrotron and the SSC photons. The seed photon density $n'_{\gamma,f} \sim \times 10^{10}\, cm^{-3}$ around $\epsilon_\gamma \sim 56$ eV is also high. For $\epsilon_\gamma < 56$ eV, synchrotron emission dominates and the low energy seed photon density increases rapidly [21]. So in principle $E_\nu > 2$ PeV can be produced more efficiently. But non-observation of neutrinos above 2 PeV from Cen A can be due to (i) low flux of UHECR above 40 PeV and/or (ii) there is a cut-off energy around 40 PeV beyond which the relativistic jet is unable to accelerate protons. Probably many more years of data are necessary to shed more light on this possible correlation between the IceCube event and the position of Cen A. Position of another HBL 1ES1312-423 also almost coincide with the position of the Cen A and thus falls within the error circle of the IceCube event 35. For this HBL the $\epsilon_\gamma = 0.32$ keV and the corresponding observed photon flux is $F_\gamma \sim 6 \times 10^{-12}\, erg\, cm^{-2}\, s^{-1}$ which is closed to the synchrotron peak [61].

The multi-TeV flaring of the objects 1ES1959+650, Mrk 421 and M87 are interpreted through the photohadronic interaction as discussed in Chapter 2 [20,62,63]. The maximum energy of these high energy γ-rays are less than 20 TeV (Mrk 421 [62]) which corresponds to proton energy $E_p < 200$ TeV and neutrino energy $E_\nu < 10$ TeV. But for the interpretation of the IceCube events the necessary proton energy will be $E_p = 20 \times E_\nu$. For $30\, TeV \leq E_\nu \leq 2\, PeV$ the proton energy will be in the range $600\, TeV \leq E_p \leq 40\, PeV$. So neutrino flux from the interaction of these very high energy protons with the background photons can be small from an individual HBL. Apart from this, we have only observed flaring episodes of very few HBLs. So it is very hard to justify the temporal correlation of IceCube events during a flaring episode of a HBL. We have to wait longer period and have sufficient data to comment about the correlation between the IceCube events and the flaring episode of the object.

In the photohadronic scenario both the TeV-PeV neutrinos and the TeV-PeV γ-rays are correlated as both are produced from the decay of charged and neutral pions respectively as shown in Eq.(2.3). The background seed photons responsible for the production of these high energy neutrinos and γ-rays have energies above few keV. These photons have energy in between the synchrotron peak and the low energy tail of the SSC spectrum. The TeV-PeV photons produced from the π^0 decay will interact mostly with the

same $\sim$ keV seed photons in the inner blob region to produce e^+e^- pairs. The required threshold energy for the seed photon to produce the pair is $\epsilon_{\gamma,th} \geq 2m_e^2/E_\gamma$ which is mostly in the microwave range. Also the $\sigma_{\gamma\gamma} \sim 1.7 \times 10^{-25}\, cm^{-2}$ is the maximum in the microwave range and the pair creation cross section for keV background photon is very small $\sigma_{\gamma\gamma} \leq 10^{-29}\, cm^2$. In the region where the TeV-PeV photons and neutrinos are produced, the microwave photon density is very low. So even if the seed photon density is high (in the keV range), the mean free path for the TeV-PeV photons satisfy $\lambda_{\gamma\gamma} \gg R'_f$, hence, there will be negligible attenuation of these photons in the inner blob region. Again in the outer blob, the low energy photon density is order of magnitude smaller than the inner blob, so no attenuation in the outer region. However, on their way to the Earth, these TeV-PeV photons can interact with the low energy photons to produce pairs.

4.1.1 Statistical analysis

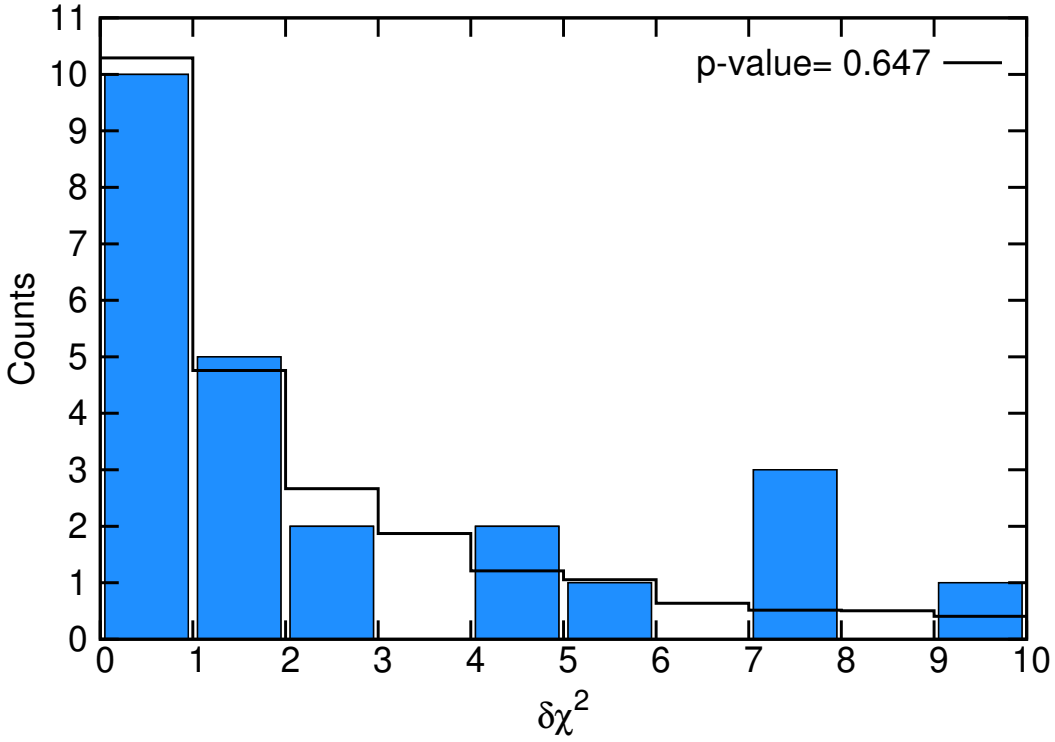

Figure 4.2: The observed IceCube events (shaded histograms) and the simulated events (open histograms with continuous line is for random RA) for different $\delta\chi^2$ distribution are shown for angular resolution of the IceCube events $\leq 40^\circ$. The p-value for the open histograms are also given.

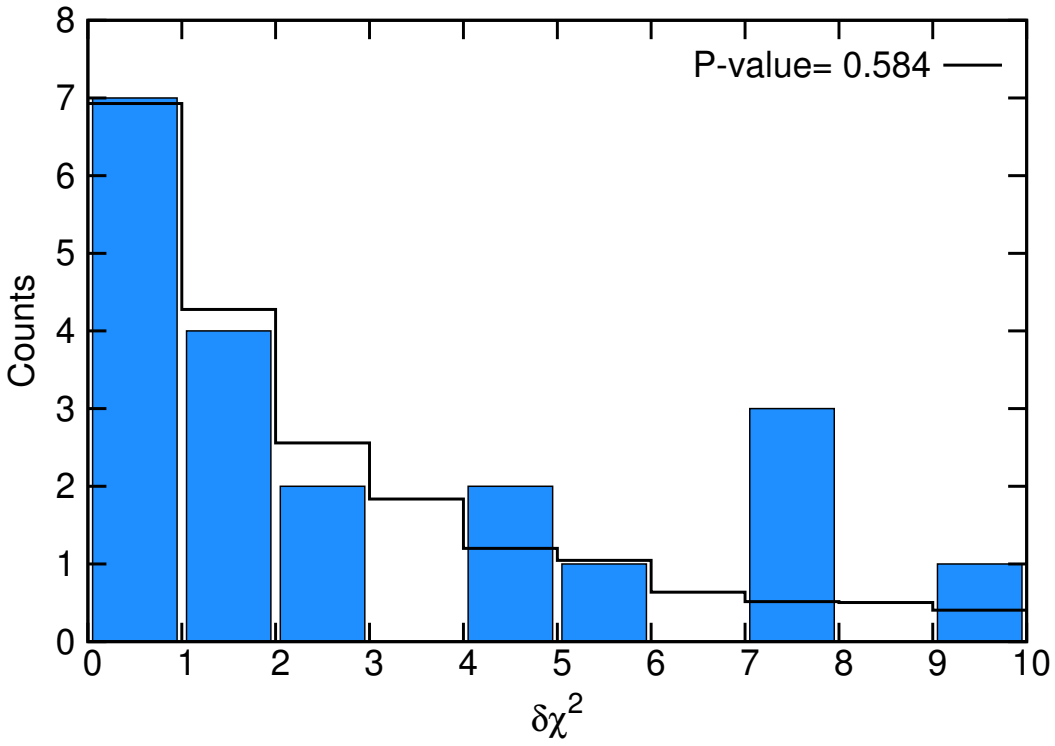

Figure 4.3: Same as fig.(4.2) but for angular resolution of the IceCube events $\leq 20^{\circ}$.

We have also done a statistical analysis to look for the correlation between the IceCube events and the 42 TeV emitting HBL/AGN from the TeVCat [47]. Here we adopt the method used in ref. [51] and convert the coordinates (RA and Dec) into unit vectors on a sphere as

$$\tilde{x} = (sin\theta\, cos\phi, sin\theta\, sin\phi, cos\theta), \tag{4.4}$$

with $\phi = RA$ and $\theta = \pi/2 - Dec$, where i and j correspond to the event coordinates and object coordinates respectively. The angle between the two unit vectors $\tilde{x}_i$ and $\tilde{x}_j$ is given as $\gamma = cos^{-1}(\tilde{x}_j.\tilde{x}_i)$ which is independent of the coordinate system and is a measure of correlation between the events and the objects. Then one makes use of the quantity

$$\delta\chi_i^2 = min_j \left(\gamma_{ij}^2/\delta\gamma_i^2\right), \tag{4.5}$$

where $\delta\gamma_i^2$ is the angular error on the ith coordinate. Only 10 events meet the condition that $\delta\chi^2 \leq 1$ with 13 objects which are shown in the sky map and also in table (4.1). The $\delta\chi^2$ values of these events are given in the last column of table (4.1). From the Monte Carlo simulation we estimate the significance of any correlation with IceCube events by randomizing the RA of the 42 objects within their allowed ranges. One has to remember

that only the value of $\delta\chi$ for the object closest to the neutrino event is chosen in this method. The distribution of $\delta\chi_i^2$ is realized by repeating this process one million times and the p-value is calculated by counting the number of times 10 or more IceCube events satisfy $\delta\chi^2 \leq 1$ divided by the total number of realizations. In fig. (4.2), the shaded histograms correspond to the number of correlated neutrino events with the 42 objects of the TeVCat in different ranges of $\delta\chi^2$ value. The open histograms correspond to the expected number of correlated neutrino events from the simulations (continuous line for the randomized RA) with their corresponding p-value which is 0.647 corresponds to a confidence level (CL) of $\sim 35\%$. In another simulation we select the IceCube events which have angular errors $\leq 20^\circ$. In this case the IceCube events 7, 21 and 31 will not contribute. So with this constraint in angular resolution, we have only 7 events instead of 10 events considered earlier. In this simulation we found the CL $\sim 42\%$ this is shown in fig. (4.3). Both of these analysis shows that there is no significant statistical correlation between the IceCube events and the HBLs positions. As we have shown by increasing the angular resolution from 40° to 20° the CL increases by $\sim 7\%$. Also we believe that 42 objects from the TeVCat are not enough to give a better statistics when the events are isotropic. Apart from these objects there may be other type of sources which will contribute but are not included in our list. In future research projects we would like to consider more sources for our analysis.

4.1.2 Summary and outlook

The astrophysical interpretation of the 37 TeV-PeV neutrino events by IceCube is challenging and several viable candidates have been proposed and HBL is one of them. The HBLs are the sources capable of producing multi-TeV γ-rays. In the photohadronic scenario, TeV γ-rays are accompanied with multi-TeV neutrinos from the decay of charged pions and kaons. By analyzing the online catalog TeVCat [47] we found coincidence of 12 HBLs and one FR-I galaxy Cen A positions within the error circles of 10 IceCube events. All these events are found to be shower events. The position of the HBL, H2356-309 coincides with three IceCube events. We found positions of Mrk 421 and 1ES1011+496 are within the error circle of the IceCube event 9 as well as within the error circle of the TA hotspot. The observed highest energy PeV event coincides with the positions of Cen A and the the HBL 1ES1312-423. Although, from the statistical analysis we found no significant correlation between the IceCube events and the 42 objects in the TeV Catalog,

it does not necessarily discard the photohadronic model interpretation for some of the IceCube events. Many more years of data are necessary to confirm or refute the positional correlations of the HBLs/AGN with the IceCube events. Also these possible candidate sources should be constantly monitored and studied in greater detail to have a better understanding of their properties and emission mechanisms.

4.2 Blazar origin of some IceCube events [67]

The ANTARES collaboration searched for high energy cosmic muon neutrinos using the data taken during the period August 2008 to December 2012 in which they selected 41 very bright and variable blazars which had undergone flaring. Here our aim is to study the positional correlation with the IceCube events, their statistical significance as well as the calculation of neutrino flux using the photohadronic scenario.

In the context of recent IceCube results, we analyzed the 41 flaring blazars taken from the Fermi-LAT catalog which are previously studied by the ANTARES collaboration to look for possible temporal and spatial correlation [48]. We have also analyzed the 7 TeV flaring objects as discussed by ANTARES collaboration for the possible spatial correlation with the IceCube events. In fact all these 7 objects are there in the TeVCat [47] which we had already analyzed in Ref. [44] and found that the only HBL, PG 1553+113 has the positional correlation with the IceCube event 17. So we don't discuss about these 7 flaring objects here any more. For our analysis of the possible correlation of IceCube events with the ANTARES sources we use the unbinned Maximum Likelihood Method (MLM) and two different values of spectral index $\kappa = 2$ and 2.5 which is shown in Eq. (4.2) . We also do the separate analysis with and without the contribution from the prompt flux coming from the charm hadron decay. Our results are summarised in table (4.2).

All the 28 shower events with their individual errors and the 8 track events are shown in the sky map with equatorial coordinates in fig. (4.4). The positions of ten FSRQs and two BL Lac objects are also shown in the sky map.

4.2.1 Unbinned Maximum Likelihood Method

To identify the possible sources of IceCube events we employ the Unbinned Maximum Likelihood Method (MLM) [68] to find spatial correlation between the blazar sample

Object (RA,Dec.)	Type z, Γ	ID	$\delta\chi^2$	E_ν/TeV	ϵ_γ/keV	n_s^*	TS	p value	post-p value
PKS2326-502 [72]	FSRQ	7	0.46	34.3	182.19	0.06	0.0008	0.44	1.0
(352.32, -49.94)	0.518,30								
PKS0208-512 [73]	FSRQ	7	0.29	34.3	37.67	0.59	0.109	0.22	1.0
(32.7, -51.2)	1.003, 18								
PKS0235-618 [38]	FSRQ	7,20	0.80,0.27	34.3, 1141	21.68, 0.65	0.39	0.040	0.18	1.0
(39.29, -61.62)	0.467,10								
PMNJ2345-1555 [74]	FSRQ	21	0.48	30.2	34.07-51.62	0.71	0.197	0.43	1.0
(356.27, -15.89)	0.621,13-16								
B22308+34	FSRQ	34	0.23	42.1	-	0.97	0.503	0.48	1.0
(347.77, 34.43)	1.817, -								
PKS0244-470	FSRQ	7	0.54	34.3	-	0.73	0.179	0.17	1.0
(41.06, -47.06)	1.385, -								
CTA102 [75]	FSRQ	34	0.31	42.1	8.85	0.77	0.249	0.53	1.0
(338.12, 11.72)	1.036, 10								
PMNJ2331-2148 [76]	FSRQ	21	0.52	30.2	31.23	0.6	0.125	0.45	1.0
(352.75 ,-21.74)	0.563, 12								
PKS2227-08 [77]	FSRQ	34	0.97	42.1	5.80	0.53	0.096	0.53	1.0
(337.44, -8.55)	1.559, 10								
OJ287 [73]	BL Lac	26	0.62	210	6.43	1.32	0.691	0.31	0.99
(133.85,20.09)	0.306 , 12					0.69	0.184	0.33	1.0
PKS0805-07	BL Lac	27	0.52	60.2	7.43	1.23	0.556	0.24	1.0
(122.06, -7.85)	1.837, 15					0.54	0.102	0.27	1.0
3C454.3 [75]	FSRQ	34	0.31	42.1	25.72	0.85	0.33	0.50	1.0
(343.5, 16.15)	0.859, 15					0.24	0.022	0.49	1.0

Table 4.2: The objects which are in the error circles of the IceCube events (ID in third column) are given in the first column. Below each object we also put their coordinates, Right Ascension and Declination (R.A., Dec.) in degrees (this table is given in equatorial coordinates). The second column gives the type of object and below this we also give its redshift (z) and the bulk Lorentz factor (Γ). In the fourth column, the $\delta\chi^2$ of the object is given. In the fifth and the sixth columns the deposited neutrino energy E_ν/TeV and the corresponding seed photon energy ϵ_γ/keV are given. In columns seventh and eighth the values of the n_s^* and TS are given from the Maximum Likelihood Method. In columns ninth and tenth the p-value and the posteriori p-value (post p-value) are also shown. The last three objects are without (upper value) and with (lower value) the prompt contribution to the background PDF.

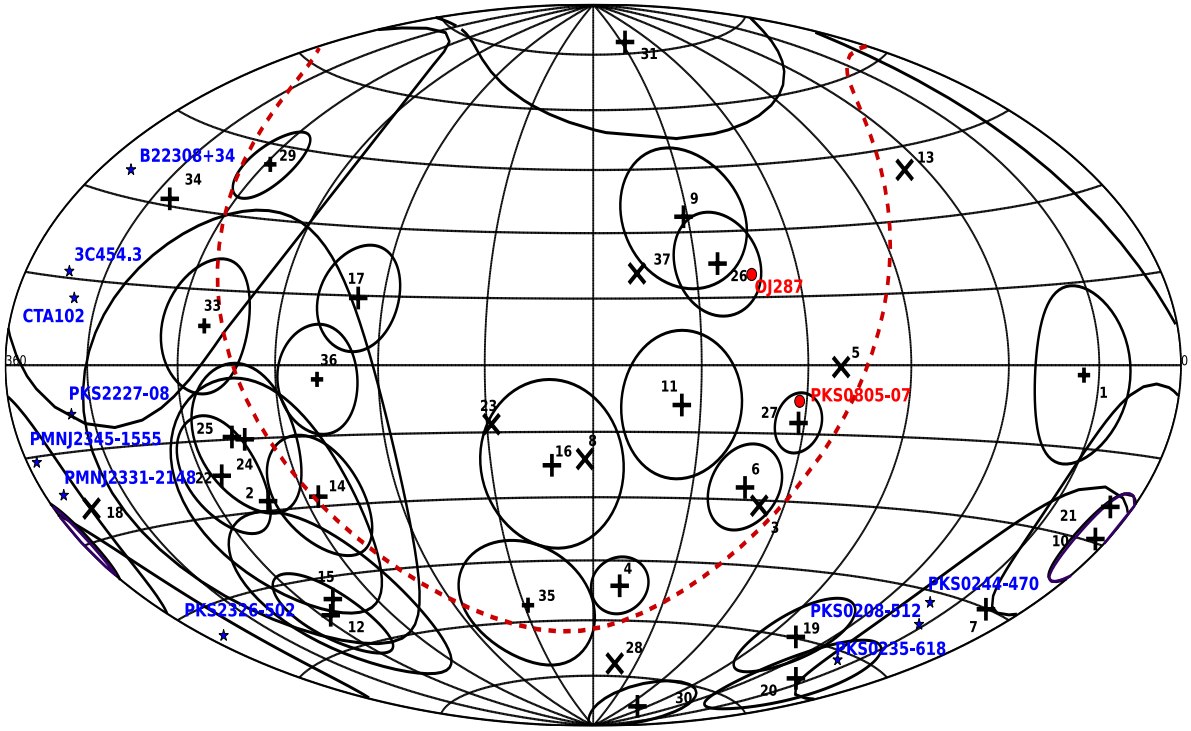

Figure 4.4: The sky map is shown in Equatorial coordinates with 37 IceCube events and their individual errors (only for shower events). Here + corresponds to shower event and × sign corresponds to track event with their corresponding event ID. We have also shown the positions and names of the blazars which are within the median angular error of the IceCube events and have a TS value > 0. The objects in blue color are FSRQs and in red color are BL Lac.

under consideration and the IceCube events. The signal and the background weights are not separable for an object and both contribute to the likelihood function, which is given by the product of the individual probability densities for the IceCube events as [69]

$$\mathcal{L}(n_s, \vec{x}_s) = \prod_{i=1}^{N} \left[\frac{n_s}{N} S_i(\vec{x}_s) + \left(1 - \frac{n_s}{N}\right) B_i \right], \tag{4.6}$$

where N is the number of IceCube events we take into account, n_s/N is the weight associate with the signal probability density function (PDF) and its values vary between 0 and 1. The background PDF depends on the the neutrino energy and the declination which is expressed as

$$B_i = \mathcal{B}(E_i, \delta_i). \tag{4.7}$$

The background is constructed from the integrated effective areas of the IceCube 79 strings configuration [30], according to section (2.5). We show the background PDF for the event

37 in fig. (4.5). The calculation program for this event and part of the data are shown in section (5.2) of the appendix. The neutrino effective area depends on the detector geometry and the absorption of the neutrinos by the Earth. The background PDF takes into account the contribution from the atmospheric muon neutrinos. Above ~ 100 TeV, neutrinos from the decay of charm hadrons $D^{\pm}, D^{0}$ contribute to the background neutrino flux known as prompt flux. Equal number of neutrinos and anti-neutrinos of electron and muon flavors are produced in this process. However, the prompt flux is poorly understood in the high energy limit. For the background calculation we also include the contribution from the prompt background [26, 70].

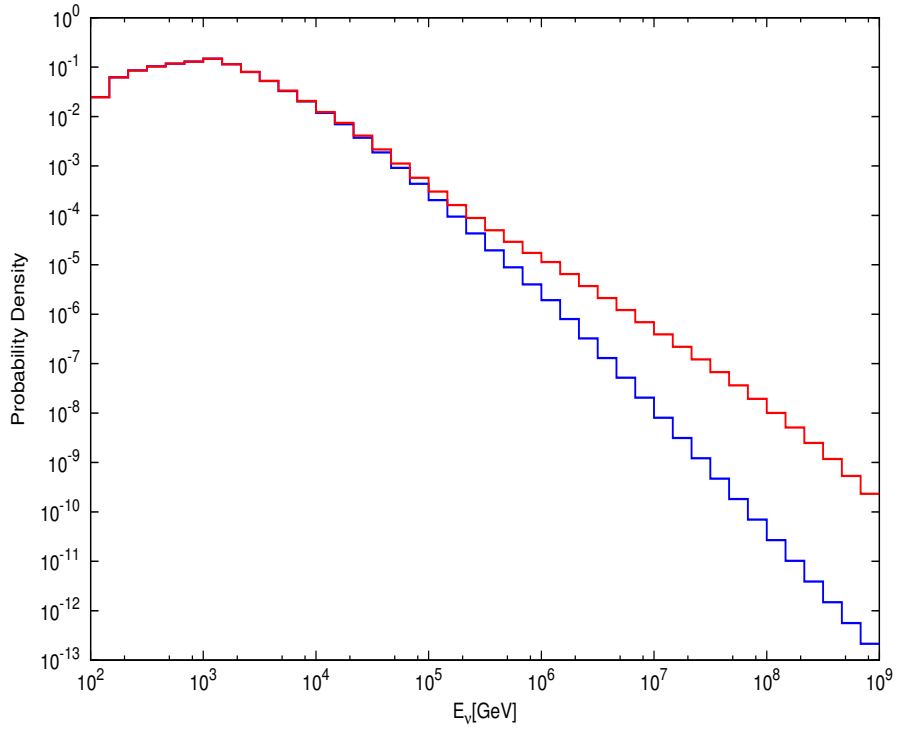

Figure 4.5: Probability density function for the neutrino event 37. The blue line is the probability taking into account the conventional neutrino background, and the red one including the conventional and prompt contributions.

The signal PDF is defined as the product of a spatial term and the energy term

$$S_i = \mathcal{S}_i(|\mathbf{x}_i - \mathbf{x}_s|, \sigma_i)\, \mathcal{E}_i(E_i, \delta_i, \kappa), \tag{4.8}$$

where we have defined

$$\mathcal{S}_i(\vec{x}_s) = \frac{1}{2\pi\sigma_i^2} e^{-\frac{|x_i - x_s|^2}{2\sigma_i^2}}, \tag{4.9}$$

which is a Gaussian function [71]. In the above Eq.(4.9), $|x_i - x_s|^2$ is the space angle difference between the source and the reconstructed event direction and σ_i is the standard deviation of the i^{th} IceCube angular error distribution, that for this case is related with the median angular error (M) like $\delta\gamma_i = 1.177 \times \sigma_i$. We also define

$$\delta\chi^2 = \frac{|x_i - x_s|^2}{\delta\gamma_i^2}, \tag{4.10}$$

The value of $\delta\chi^2 \leq 1$ signifies that the object is inside the median angular error $\delta\gamma$ of the IceCube event. The signal energy PDF $\mathcal{E}_i$ is constructed in a similar form that background one and depends on the event energy, spectral index κ and the declination. Here we use $\kappa = 2$ and 2.5 for our analysis. The graph the signal PDF for the 0^o to 30^o effective area is shown in the fig. (4.6).

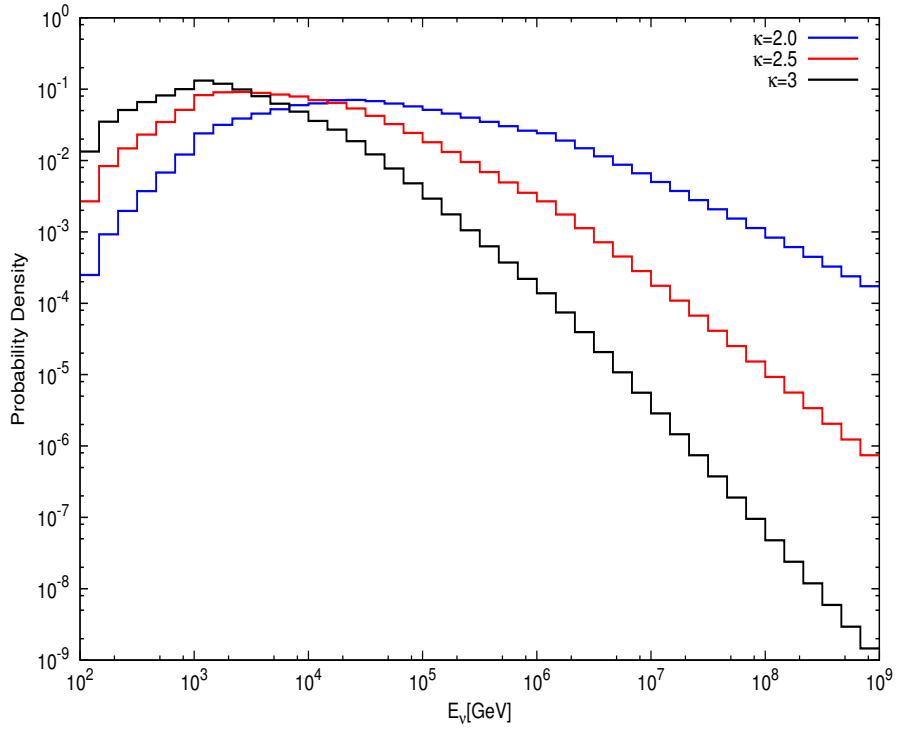

Figure 4.6: Effective Area for a muon neutrino for the effective area of the angle range from 0^o to 30^o. The parameter κ is valuated in 2,2.5 and 3 but the values of 3 are not used in the MLM.

The ANTARES analysis takes into account both the temporal and energy dependence of the flaring events whereas our analysis is independent of the time. The observed IceCube events can be modelled by taking into account two hypothesis: (1) the events

could be produced by the muon neutrinos (background), or (2) from an astrophysical source which also includes the background contribution. A good test of compatibility is the ratio of these two hypothesis. We can take the ratio of the likelihood with the background of unique weight ($n_s = 0$) and the maximized likelihood of the second hypothesis with the corresponding n_s values defined as $n_s = n_s^*$. Now to evaluate each point source we use this Test Statistic (TS) taking minus twice the log of the likelihood ratio,

$$TS = -2 \log \left[\frac{\mathcal{L}(n_s = 0)}{\mathcal{L}(n_s = n_s^*)} \right]. \tag{4.11}$$

For this procedure we use all the IceCube events. For our present analysis, we take into account 36 events out of reported 37 events (event 32 is excluded in the present analysis because its energy and direction are not reported). We calculate the significance of each source location, running 10,000 simulations in which the declination of each IceCube sample event is fixed but the right ascension is randomized. In this case p-value is calculated as the number of simulations with $TS_{(sim)} \geq TS$ divided by the total number of simulations for a given source, where $TS_{(sim)}$ is the TS value obtained from the simulation. Also, the posteriori p-value for each object is estimated as the fraction of the randomized simulations that yields an equal or higher TS value for at least one of the 41 ANTARES sources. The compatibility of the second hypothesis depends on the estimate of the posteriori p-value. If the posteriori p-value is close to unity then it is consistent with the background.

4.2.2 With spectral index $\kappa = 2$

From the 41 Fermi blazars of ANTARES list, 32 objects have TS > 0 for the spectral index $\kappa = 2$ without the prompt contribution to the background. However, this number reduces to 19 when we include the charm contribution.

From the above 32 objects 12 are within the median angular error of at least one IceCube event having $\delta\chi^2 < 1$. The FSRQ, PKS 0235-618 is the only object associated with two IceCube events (7, 20). The FSRQs, PKS 2326-502, PKS 0208-512, PKS 0235-618 and PKS 0244-470 are within the error circle of event 7, while the FSRQs, 3C454.3, B22308+34, CTA102 and PKS 2227-08 are within the error circle of event 34. Another two FSRQs, PMNJ2345-1555 and PMNJ 2331-2148 are within the error circle of the IceCube event 21. The BL Lac objects, OJ287 and PKS0805-07 are coincident with the

events 26 and 27 respectively. All the relevant parameters of the above objects are shown in table (4.2).

4.2.3 Statistical analysis

Using the above MLM method, the posteriori p-value of all the above 12 objects are found to be $\geq 99\%$. This shows that our result (without the prompt contribution to the atmospheric background) is consistent with the background fluctuation.

By including the prompt contribution to the background we found that 19 objects have TS > 0 of which only three objects two BL Lac objects (OJ287, PKS 0805-07) and one FSRQ (3C454.3) are within the median angular error of three IceCube events (26, 27, 34). These three objects are shown in the table (4.2)

We observed that the background photon energy ϵ_γ for most of the events are below $<$ 40 keV which shows that the photon density $n'_{\gamma,f}$ can be large in the inner region of the jet. By assuming a conservative 1% energy loss by the UHE protons we get the photon density in the inner region $n'_{\gamma,f} \sim 2 \times 10^{10}\, cm^{-3}$ which has a radius $R'_f \sim 10^{15}\, cm$. Estimate of R'_f value depends on the outer blob radius R'_b, while the later parameter is adjusted to fit the spectral energy distribution (SED) in the leptonic model of the objects. However, for most of the objects $R'_b > 10^{15}$ cm is taken to fit the SED [44]. So, here we take $R'_f \sim 10^{15}\, cm$ for the estimation of $n'_{\gamma,f}$. The simulation shows that the $0 <$ TS < 1 for all the objects.

The diffuse neutrino flux F_ν for all these objects is $2.31 \times 10^{-9}\ \ GeV\, cm^{-2}\, s^{-1}\, sr^{-1}$ because for $\kappa = 2$, the integral in Eq. (4.2) is independent of the redshift, so the F_ν is the same for all the objects. On the other hand it varies slightly for $\kappa \neq 2$. The high posteriori p-value for all these objects shows that our result is consistent with the background fluctuation. We also repeated the simulation for $\kappa = 2.5$. As κ changes the flux reduces and found that non of the 41 objects satisfy the condition TS > 0.

4.2.4 Summary and outlook

ANTARES collaboration looked for possible temporal and spatial correlation of 41 flaring objects selected from the Fermi-LAT catalog. We analyzed the same objects for the possible spatial correlation with the IceCube events. For our analysis, we take into account

the energy dependence of both the background and the signal constructed from the data of the 79 IceCube string configuration. We consider two different values of the spectral index 2 and 2.5 and also analyze our results with and without the prompt contribution to the atmospheric neutrino flux. We observed that, from the 41 flaring objects, for $\kappa = 2$, the MLM gives twelve objects (without prompt flux contribution) and three objects (with prompt flux contribution) within the error circle of some IceCube events. For these objects we have also estimated the neutrino flux. However, for all these possible candidates, the TS value is very small which leads to very high posterior p-values $\geq 99\%$ and is consistent with the background fluctuation. It is possible that the high energy neutrino flux from these objects are much below the IceCube limit or blazars may not have powerful central engine to produce very high energy cosmic rays. So most of the events in IceCube can be from some other type of sources. We have to wait for more data to look for possible correlation of FSRQs and BL Lac objects with the IceCube events.

4.3 Multi-TeV flaring from Markarian 421 [62]

By using the one-zone SSC model, the average SED of Mrk 421 is fitted in fig. (11) of ref. [15]. In fig. (4.7) we show the SED of Mrk 421. In this figure, the red crosses to the extreme left are the measurements in the radio frequency band measured by 26 m telescope at the University of Michigan Radio Astronomy Observatory (UMRAO) and by the 13.7 m Metsähovi radio telescope at Helsinki. The single cross (red) in the optical range is measured by Fred Lawrence Observatory (FLWO) 1.2 m telescope. The points of the first peak in the X-ray range are from Rossi X-ray Explorer (RXTE) [15].

In the one-zone leptonic model, the blob of size $R'_b \sim 0.7 \times 10^{16}\, cm$ moves down the conical jet with a Lorentz factor $\Gamma \simeq 14$ and a Doppler factor of $\mathcal{D} = 14$. The emitting region is filled with an isotropic electron population and a randomly oriented magnetic field $B' = 0.26$ G. In the present work we study the flaring of Mrk 421 during April 2004. We use the parameters of the one-zone leptonic model of ref. [15]. The parameters of the one-zone synchrotron model are summarized in table(4.3). In principle the Lorentz factor in the inner jet should be larger than the outer jet. But here we assume that $\Gamma_{out} \simeq \Gamma_{in} \simeq \Gamma$.

The flaring of Mrk 421 in April 2004 was observed in the energy range $0.25\, TeV (6.0 \times 10^{25}\, Hz) \leq E_\gamma \leq 16.85\, TeV (4.1 \times 10^{27}\, Hz)$ by the Whipple telescope. In the hadronic

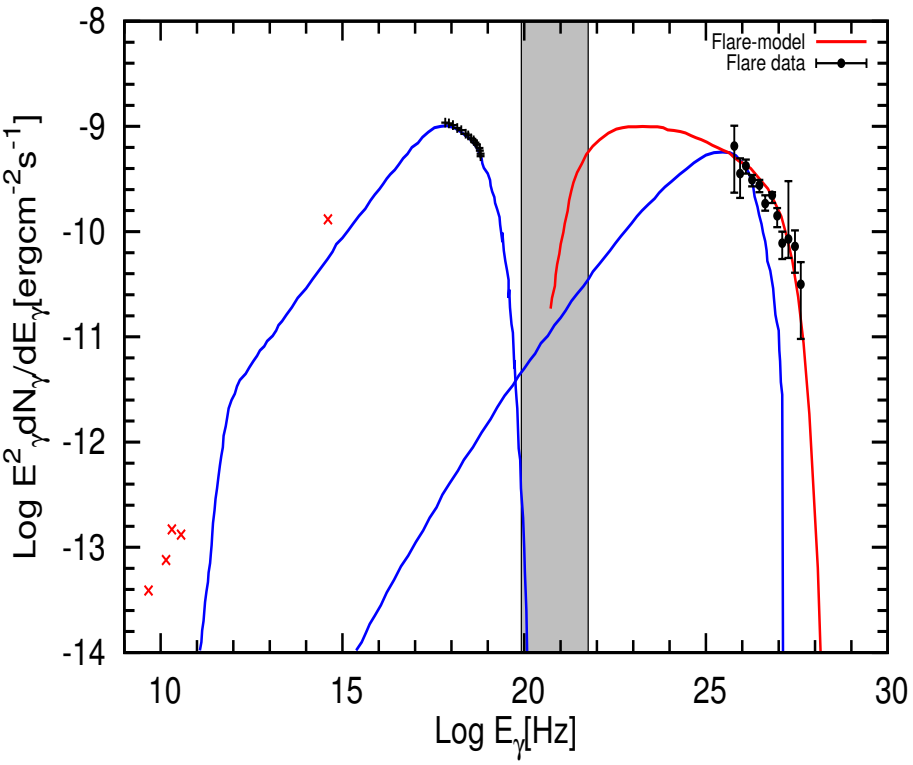

Figure 4.7: The SED of Mrk 421 is shown in all the energy bands which are taken from Ref. [15]. The flare of April 2004 in multi-TeV energy is shown here. The hadronic model fit to the April 2004 data is shown as continuous line to the extreme right. The shaded region is the energy range of SSC photons where the Fermi-accelerated protons are collided to produce the Δ-resonance.

model discussed above, this corresponds to the Fermi accelerated proton energy in the range $2.5\,TeV \leq E_p \leq 168\,TeV$ and the corresponding background photon energy will lie in the range $23.6\,MeV(5.7 \times 10^{21}\,Hz) \geq \epsilon_\gamma \geq 0.35\,MeV(8.4 \times 10^{19}\,Hz)$. This range of ϵ_γ is the shaded region shown in fig. (4.7) which is in the low energy tail of the SSC photons. For the calculation of normalized multi-TeV flux we take into account one of the observed TeV fluxes from the flare with its corresponding energy and with the use of Eq.(2.16) calculate other TeV fluxes. In this model the free parameters are the spectral index α and the TeV γ-ray cut-off energy E_c which are adjusted to obtain the best fit and the values are $\alpha = 2.7$ and $E_c = 6.2$ TeV. This value of E_c corresponds to the proton cut-off energy $E_{p,c} = 62$ TeV and the background SSC photon energy $\epsilon_{\gamma,SSC} = 0.96\,MeV$ $(2.3 \times 10^{20}\,Hz)$ which is very close to the beginning of the SSC energy as shown in fig. (4.7). This shows that for orphan flaring, the cut-off energy E_c is due to the change from the synchrotron band to the SSC band and can be calculated from their crossover energy.

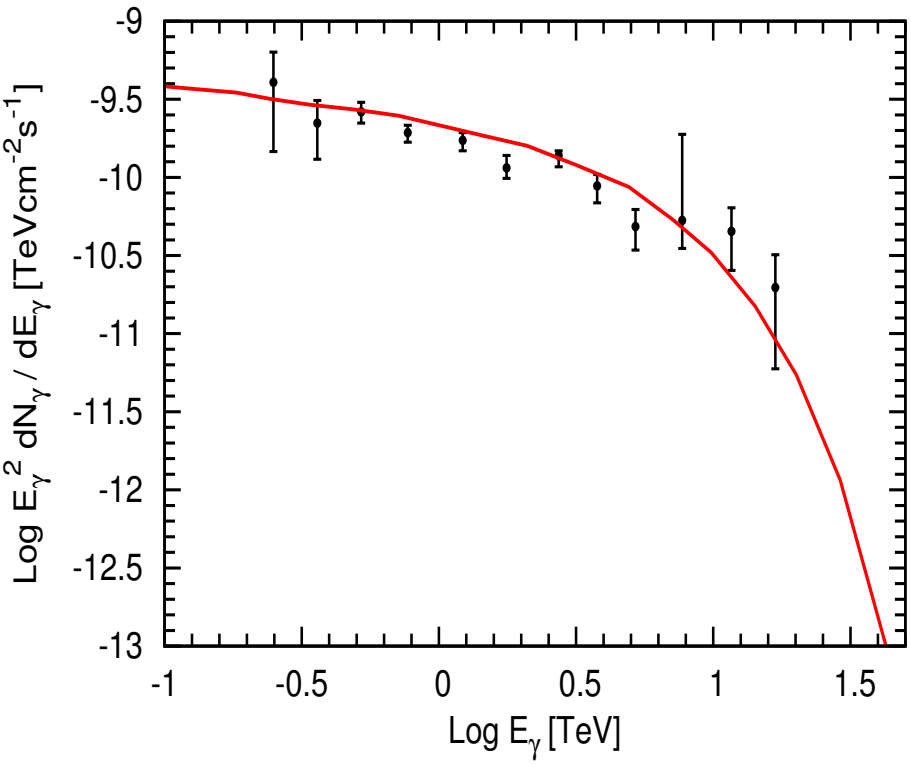

Figure 4.8: The continuous curve is the hadronic model fit to the multi-TeV flaring data of Mrk 421.

In fig. (4.8) we show both the observed multi-TeV SED and our model fit to it. In our results, the presence of $\Phi_{SSC}(\epsilon_\gamma)$ in Eq. (2.17) modifies the power-law with the exponential fall scenario. From the best fit parameters we obtain the value of the dimensionless constant $A_\gamma \simeq 20$ in Eq. (2.17). By using the best fit parameters, we have also calculated the value of A_γ from the multi-TeV flare of 1ES 1959+650 and M87 and the multi-TeV emission from Centaurus A, which are given as 86, 1.86 and 8.6×10^{-4} respectively. We observe that for orphan flaring the condition $A_\gamma \gg 1$ is satisfied as is seen from 1ES 1959+650 and Mrk421. On the other hand for non-orphan flaring this value is small i.e. $A_\gamma \leq 1$.

In the flaring state, the proton luminosity L_p for the highest observed proton energy $E_p = 168$ TeV has to be smaller than the $L_{Edd} \sim 2.5 \times 10^{46}\, erg\, s^{-1}$ and this gives $\tau_{p\gamma} > 0.02$ in the inner jet region. For our estimates we consider the hidden jet size $R'_f \simeq 3{\times}10^{15}$ cm which is between R_s and the blob radius R'_b. This value of R'_f corresponds to a day scale variability. We take day scale variability due to the fact that the flaring lasted for more than two weeks. If we consider small R'_f then the seed photon density

Table 4.3: These parameters (up to B') are taken from the one-zone synchrotron model of ref. [15] which are used to fit the SED of Mrk 421. The last three parameters are obtained from the best fit to the observed flare data in our model.

Parameter	Description	Value
M_{BH}	Black hole mass	$(2-9)\times 10^8 M_\odot$
z	Redshift	0.031
Γ	Bulk Lorentz Factor	14
$\mathcal{D}$	Doppler Factor	14
R'_b	Blob Radius	0.7×10^{16}cm
B'	Magnetic Field	0.26 G
R'_f	Inner blob Radius	3×10^{15}cm
α	Spectral index	2.7
E_c	γ-ray Cut-off Energy	6.2 TeV

will increase as can be seen from (2.20). But this increase in density will not affect our results because we are using the scaling behavior of Eq.(2.2). The constraint on the optical depth gives the lower limit on the seed photon density in the inner region $n'_{\gamma,f} > 1.3\times 10^{10}\, cm^{-3}$. Again by assuming $t'_{p\gamma} < t'_d$ we obtain the upper limit on the optical depth $\tau_{p\gamma} < 2$ and this corresponds to the photon density $n'_{\gamma,f} < 1.3\times 10^{12} cm^{-3}$. We have also estimated the seed photon density from Eq.(2.20), for $\epsilon_\gamma = 0.35$ MeV, which gives $n'_{\gamma,f} < 8.9\times 10^{10} cm^{-3}$. The upshot of this analysis is that we get the constraint $1.3\times 10^{10}\, cm^{-3} < n'_{\gamma,f} < 8.9\times 10^{10} cm^{-3}$, which shows that the photon density in this region is high. This range of photon density corresponds to the optical depth in the range $0.02 < \tau_{p\gamma} < 0.13$ and the proton flux at $E_p = 168$ TeV is below the $F_{Edd} \sim 1.24\times 10^{-8}\, erg\, cm^{-2}\, s^{-1}$. Due to the adiabatic expansion of the inner blob, the photon density will be reduced to n'_γ and the energy will dissipate once these photons are in the bigger cone. So even if we have two-zones (the inner and the outer), only the outer zone will be responsible for the observed synchrotron and IC peaks. From the leptonic model fit to the SED, the magnetic field in the outer jet region is $B' = 0.26$ G and higher magnetic field is expected in the inner jet region. The maximum proton energy in the hidden jet region will be $E_{p,max} \sim 10^{18}(B'_f/1G)$ eV and for larger magnetic field the $E_{p,max}$ can even be higher.

In the normal jet scenario we estimate the proton flux needed to explain the observed

TeV γ-rays. Corresponding to the background energy $\epsilon_\gamma = 0.35$ MeV the photon density is $n'_\gamma \sim 4 \times 10^3\, cm^{-3}$ and the the optical depth is $\tau_{p\gamma} \sim 1.4 \times 10^{-8}$. As discussed above, for background SSC photon energy 0.35 MeV, the observed TeV photon has the energy $E_\gamma = 16.85$ TeV and its flux is $F_\gamma \sim 3.16 \times 10^{-11}\, erg\, s^-\, cm^{-2}$. The high energy proton responsible for the photohadronic process to produce this TeV γ-ray has energy $E_p = 168$ TeV and we can estimate its flux from Eq.(2.21) which gives $F_p \simeq 10^6 \times F_{Edd}$. This shows that the normal jet model needs super Eddington power in protons to explain the high energy peaks, whereas, the inner jet scenario exterminates this extreme energy requirement.

The high energy protons will be accompanied by high energy electrons in the same energy range. In the magnetic field of the jet, these electrons will emit synchrotron photons in the energy range $4 \times 10^{19}\, Hz$ to $2 \times 10^{23}\, Hz$, which is in the lower part of the SSC spectrum and will not be observable because of the lower flux. Also the SSC emission will take place from these high energy electrons and the energy of these IC photons will be $E_{IC} \sim \gamma_e^2 \epsilon_{syn}$. By considering the electron Lorentz factor in the range $7 \times 10^2 \leq \gamma_e \leq 4 \times 10^4$ [50] and the peak energy of the synchrotron photon $\epsilon_{syn} \sim 10^{18}\, Hz$, the SSC process can contribute in the energy range $2\, GeV \leq E_{IC} \leq 6.6\, TeV$. But the details of the SSC flux depends on the breaks in SSC spectrum and the spectral index. It is observed that during the flaring of Mrk 421, the X-ray emission reached the peak, days after the TeV emission, which poses a serious challenge to the SSC model [15]. The SSC contribution to the multi-TeV band will be very much suppressed. Similarly the multi-TeV photons in the energy range $0.25\, TeV \leq E_\gamma \leq 16.85\, TeV$ can interact with the background photons to produce e^+e^- pair and these individual electron or positron will have energy $E_\gamma/2$. To produce e^+e^- pair the required threshold seed photon energy $\epsilon_\gamma \geq 2m_e^2/E_\gamma$ is needed. During the flaring, the multi-TeV γ-rays in the energy range $0.25\, TeV \leq E_\gamma \leq 16.85\, TeV$ will interact with the soft seed photons in the energy range $0.05\, eV \leq \epsilon_\gamma \leq 3.5\, eV$ (in between the infrared and the visible range), where $\sigma_{\gamma\gamma} \sim 1.7 \times 10^{-25}\, cm^2$ is the maximum cross section and for higher ϵ_γ, the $\sigma_{\gamma\gamma}$ will be smaller. The origin of these soft photons are from the synchrotron emission of $1 - 10$ GeV electrons in a magnetic field ~ 1 Gauss towards the base of the evolving jet as well as the ambient photons from the disk. On the other hand multi-TeV γ-rays are produced beyond this region where the photons are in the low energy tail ($0.35\, MeV - 23.5\, MeV$ range) of the IC photons. These two regions are distinct and there will not be enough low energy seed photons (0.05-3.5 eV) in the IC tail

region. So, mostly the TeV photons will encounter the IC photons and the pair production cross section for $\epsilon_\gamma \geq 0.35\,MeV$ is very small $\sigma_{\gamma\gamma} \leq 10^{-30}\,cm^2$, which corresponds to a mean free path $\lambda_{\gamma\gamma} \geq 10^{19}\,cm$. Hence, TeV photons will not be attenuated much due to e^+e^- pair production. Also it has been observed that, during the flaring of Mrk 421, the variation in the light curves at optical and radio wavelengths are slight [15], which shows that the low energy photon production was suppressed. The positron produced from the π^+ decay will have energy $E_\gamma/2$ and it will radiate synchrotron photons in the energy range $2 \times 10^{17}\,Hz$ to $9 \times 10^{20}\,Hz$. The photon flux $F_{e^+,syn}$ from the synchrotron radiation of e^+ will be much smaller than $F_\gamma(E_\gamma = 0.25\,TeV)/8$, i.e., $F_{e^+,syn} \ll 8 \times 10^{-11}\,erg\,cm^{-2}\,s^{-1}$. This flux is well below the observed flux limit in the normal case as can be seen from fig. (4.7). From the above analysis our conclusion is that, the photon fluxes from the synchrotron emission of the electrons and positrons are not observable during the flaring event of Mrk 421 in April 2004, which makes this flare orphan, like the one observed in 1ES 1959+650. In principle, the multi-TeV γ-rays from the extragalactic sources can be reduced due to the absorption of TeV photons by the diffuse extragalactic background light (EBL) through the process $\gamma_{\rm TeV} + \gamma_{\rm b} \rightarrow e^+e^-$ due to the energy dependent optical depth [78–80]. But for low redshifts and the energy rage of our interest, the optical depth does not vary much. Hence we can assume almost a constant optical depth [22] so that the spectral shape remains nearly unchanged.

In conclusion, from the study of the flaring events in blazars, we deduce that the flaring phenomena can be explained through the photohadronic interaction in a compact and confined region within the blazar jet where the photon density is high. From the study of 1ES 1959+650 and Mrk 421, we deduce that orphan flaring can only be possible for those blazars which have a deep valley in between the end of the synchrotron SED and the beginning of the SSC SED as shown in fig. (4.7). We note that the HBLs Mrk 501 and PG 1553+113 are possible candidates for orphan flaring in future. For the orphan flaring events we find $A_\gamma \gg 1$ and for non-orphan flaring $A_\gamma \leq 1$.

If Mrk 501 were to produce an orphan flare then the flare energy will lie in the range $1\,TeV \leq E_\gamma \leq 8.6\,TeV$ and this corresponds to the background SSC photon energy in the range $4.3\,MeV \geq \epsilon_\gamma \geq 0.5\,MeV$. We estimate this by taking the parameters of Mrk 501 as follows: $\mathcal{D} = 12$, $z = 0.034$ from Ref. [81]. In this case the maximum Fermi-accelerated proton energy will be $E_p \leq 10E_\gamma \sim 86\,TeV$. Also, another condition which must hold for

the orphan flaring is (from Eq.(2.18))

$$A_\gamma = \frac{F(8.6\,TeV)}{\Phi_{SSC}(0.5\,MeV)} \left(\frac{1}{8.6}\right)^{-\alpha+3} e^{8.6/(E_c/TeV)} \gg 1. \tag{4.12}$$

It has to noted that, if $\mathcal{D}$ changes, accordingly the values of E_γ, ϵ_γ and the E_p will also change, but the condition of Eq.(4.12) is independent of these changes.

4.3.1 Summary and outlook

The orphan flaring of Mrk 421 can be explained well by the hadronic model. We observe that, in this model, the multi-TeV photon flux is proportional to $\Phi_{SSC}(\epsilon_\gamma)$, $E_\gamma^{-\alpha+3}$ and an exponential decay term as shown in Eq. (2.17). This implies that the Fermi accelerated protons interact with the background photons (in the low energy tail) of the SSC spectrum. During the April 2004 flaring of Mrk 421, we have shown that the flux from the synchrotron emission from the high energy e^+ and e^- is suppressed relative to the normal flux implying that the flaring was orphan in nature, like the one observed in 1ES 1959+650. We have also shown what type of blazar spectrum will result in orphan flaring and predict that Mrk 501 and PG 1553+113 are possible candidates for orphan flaring in the future. Monitoring of these objects by the TeV gamma-ray telescopes will shed more light on the details on the orphan flaring mechanism.

4.4 Articles

For the ending of this chapter we put the first page of each article in the same order of this content to show each of the papers published.

Eur. Phys. J. C (2015) 75:273
DOI 10.1140/epjc/s10052-015-3519-1

THE EUROPEAN PHYSICAL JOURNAL C

Letter

Some possible sources of IceCube TeV–PeV neutrino events

Sarira Sahu[a], **Luis Salvador Miranda**

Instituto de Ciencias Nucleares, Universidad Nacional Autónoma de México, Circuito Exterior, C.U., A. Postal 70-543, 04510 Mexico, DF, Mexico

Received: 24 March 2015 / Accepted: 10 June 2015 / Published online: 23 June 2015

Abstract The IceCube Collaboration has observed 37 neutrino events in the energy range 30 TeV $\leq E_\nu \leq$ 2 PeV and the sources of these neutrinos are unknown. Here we show that the positions of 12 high energy blazars and the position of the FR-I galaxy Centaurus A coincide within the error circles of ten IceCube events, the latter being in the error circle of the highest energy event so far observed by IceCube. Two of the above blazars are simultaneously within the error circles of the Telescope Array hotspot and one IceCube event. We found that the blazar H2356-309 is within the error circles of three IceCube events. We propose that photohadronic interactions of the Fermi accelerated high energy protons with the synchrotron/SSC background photons in the nuclear region of these high energy blazars and AGN are probably responsible for some of the observed IceCube events.

1 Introduction

In November 2012, the IceCube Collaboration announced the detection of two showerlike events with energies slightly above 1 PeV by analyzing the data taken during May 2010–May 2012 [1].

A follow-up analysis of the same data published in November 2013 revealed additional 26 events in the energy range ∼30 to 250 TeV [2]. Reconstruction of these events shows that 21 events are showerlike, mostly caused by ν_e and ν_τ and seven are muon track events. These 28 events have flavors, directions, and energies inconsistent with those expected from the atmospheric muon and neutrino backgrounds and probably this is the first indication of extraterrestrial origin of high energy neutrinos. The track events have uncertainty of order one degree in their arrival directions and the angular resolution for 21 shower events is poor, ranging from∼10° to ∼50°. The IceCube analysis ruled out any spatial clustering of the events. The third year (2012–2013) data analysis revealed additionally nine events, of which two are track events and the rest are shower events [3]. The event 35 is the most energetic one so far observed. In the full 988-day data, the muon background is expected to be 8.4 ± 4.2 and for the atmospheric neutrinos we have $6.6^{+5.9}_{-1.6}$. Five events are down going muons and are consistent with the expected background muon events. This shows that the IceCube events are predominantly shower events. For a E_ν^{-2} spectrum the best fit diffuse flux obtained by IceCube per flavor is $F_\nu = (0.95 \pm 0.3) \times 10^{-8}$ GeV cm^{-2} s^{-1} sr^{-1}, which is consistent with the Waxman–Bahcall bound [4]. The observation of these neutrinos triggered a lot of excitement as regards understanding of their origin and production mechanism. While interpreting these events in terms of astrophysical models seems challenging, several possible galactic and extra galactic sources have been discussed, which include the Galactic center [5–8], γ-ray bursts (GRBs) [9,10], active galactic nuclei (AGN) [11–14], high energy peaked blazars (HBLs) [15–17], starburst galaxies [18,19] etc. In Ref. [15] many positional correlations of BL Lac objects and galactic pulsar wind nebulae with the IceCube events are shown. It is also very natural to expect that these neutrinos might come from diverse sources having different production mechanisms and different power laws and this information can probably be extracted from the directionality of the observed neutrino events. The largest concentration of seven events is around the Galactic center and also clustering of the events could be associated to the Norma arm of the Galaxy [20]. As the statistics is too sparse, it is premature to draw any conclusion regarding the galactic origin of these events. There are also nonstandard physics interpretations of these events [21–27].

We found coincidence of 12 TeV emitting HBL positions and the FR-I galaxy Centaurus A (Cen A) within the error circles of ten IceCube events from the online catalog for TeV astronomy (TeVCat) [28]. Due to the observed multi-TeV emission, these objects have long been believed

[a] e-mail: sarira@nucleares.unam.mx

Eur. Phys. J. C (2016) 76:402
DOI 10.1140/epjc/s10052-016-4247-x

THE EUROPEAN PHYSICAL JOURNAL C

Regular Article - Theoretical Physics

Blazar origin of some IceCube events

Luis Salvador Miranda[a], **Alberto Rosales de León**[b], **Sarira Sahu**[c]

Instituto de Ciencias Nucleares, Universidad Nacional Autónoma de México, Circuito Exterior, C.U., A. Postal 70-543, 04510 Mexico, DF, Mexico

Received: 2 October 2015 / Accepted: 5 July 2016 / Published online: 15 July 2016

Abstract Recently the ANTARES collaboration presented a time dependent analysis of a selected number of flaring blazars to look for upward going muon events produced from the charge current interaction of the muon neutrinos. We use the same list of flaring blazars to look for a possible positional correlation with the IceCube neutrino events. In the context of the photohadronic model we propose that the neutrinos are produced within the nuclear region of the blazar where Fermi accelerated high energy protons interact with the background synchrotron/SSC photons. Although we found that some objects from the ANTARES list are within the error circles of a few IceCube events, the statistical analysis shows that none of these sources have a significant correlation.

1 Introduction

Interactions of ultra high energy cosmic rays (UHECRs) with the background medium photons and protons produce high energy γ-rays and neutrinos. On their way to Earth the UHECRs can be deflected in the magnetic field and the high energy γ-rays can be absorbed. So both of these heavenly messengers will lose their directionality. On the other hand neutrinos will be directly pointing to the source, which is why neutrinos are considered as ideal cosmic messengers.

The IceCube detector located at South Pole in Antarctic ice is precisely built to look for high energy neutrinos (above few TeV) by measuring the Cherenkov radiation of the secondary particles created in each neutrino event. The energy deposited by each event and the secondary particles' direction and topology can be calculated from the trail of the observed Cherenkov light. In 2012 the IceCube collaboration published two years of data (2010–2012) in which 28 neutrino events with energies between 30 and 1200 TeV were observed [1]. Twenty-one of these events are shower-like and the rest are muon tracks. In this analysis two events were PeV neutrino shower events. Adding a third year of analysis in a total 988-days data revealed a total of 37 events, of which nine are track events and the rest are shower events [2]. The shower events have larger angular errors (an average of 15°) than the track events (about 1°). These events have flavors, directions, and energies inconsistent with those expected from the atmospheric muon and neutrino backgrounds. So the study of arrival directions is helpful to find sources of high energy neutrinos and the relevant acceleration mechanism acting within the source.

The isotropic distribution of these IceCube neutrino events suggests a contribution from at least some extragalactic sources. There exist different types of potential astrophysical sources to produce UHECRs and hence high energy neutrinos and γ-rays. The list includes: γ-ray bursts (GRBs) [3], core of active galactic nuclei (AGN) [4], high energy peaked blazars (HBLs) [5–7], starburst galaxies [8], and sources from Galactic center [9]. In Ref. [5] many positional correlations of BL Lac objects and galactic pulsar wind nebulae with the IceCube events are shown. There are also nonstandard physics interpretations of these IceCube events from the decay of superheavy dark matter particles, the leptoquark interaction, and the decay of exotic neutrinos [10] (see [11] for a recent review).

Recently the ANTARES collaboration presented a time dependent analysis [12] to look for upward going muon tracks by charge current interaction of ν_μ from flaring blazars selected from the Fermi-LAT and TeV γ-ray observed by ground based telescopes H.E.S.S, MAGIC, and VERITAS, respectively. In this analysis the most significant correlation was found with a GeV flaring blazar from the Fermi-LAT catalog. However, the post-trial probability estimate shows that the event was compatible with background fluctuations. In this work we would like to analyze the above list of Fermi-LAT flaring blazars to see if there is any correlation with the IceCube neutrino events. We use the unbinned maximum

[a] e-mail: luis.miranda@correo.nucleares.unam.mx
[b] e-mail: albertoros4@ciencias.unam.mx
[c] e-mail: sarira@nucleares.unam.mx

Eur. Phys. J. C (2016) 76:127
DOI 10.1140/epjc/s10052-016-3975-2

THE EUROPEAN PHYSICAL JOURNAL C

Regular Article - Theoretical Physics

Multi-TeV flaring from blazars: Markarian 421 as a case study

Sarira Sahu[1,a], **Luis Salvador Miranda**[1,b], **Subhash Rajpoot**[2,c]

[1] Instituto de Ciencias Nucleares, Universidad Nacional Autónoma de México, Circuito Exterior, C.U., A. Postal 70-543, 04510 Mexico, DF, Mexico
[2] Department of Physics and Astronomy, California State University, 1250 Bellflower Boulevard, Long Beach, CA 90840, USA

Received: 22 April 2015 / Accepted: 25 February 2016 / Published online: 7 March 2016

Abstract The TeV blazar Markarian 421 underwent multi-TeV flaring during April 2004 and simultaneously observations in the X-ray and TeV energies were made. It was observed that the TeV outbursts had no counterparts in the lower energy range. One implication of this is that it might be an orphan flare. We show that Fermi-accelerated protons of energy $\lesssim$168 TeV can interact with the low energy tail of the background synchrotron self-Compton photons in the inner region of the blazar to produce the multi-TeV flare and our results fit very well with the observed spectrum. Based on our study, we predict that the blazars with a deep valley in between the end of the synchrotron spectrum and the beginning of the SSC spectrum are possible candidates for orphan flaring. Future possible candidates for this scenario are the HBLs Mrk 501 and PG 1553 + 113 objects.

1 Introduction

Active galactic nuclei (AGN) emit electromagnetic radiation the spectrum of which stretches from radio to gamma-rays and exhibit large luminosity variations on time scales ranging from less than an hour up to several years. A super massive black hole is believed to sit at the center of the AGN surrounded by an accretion disk in the inner region and a torus of gas cloud in the outer region. Oppositely directed relativistic jets are ejected from the AGN which are perpendicular to the accretion disk and the torus. In the framework of the unification scheme of AGN, blazars and radio galaxies are intrinsically the same objects, viewed at different angles with respect to the jet axis. When the angle between the jet and the line of sight is small they are called blazars and in contrast, for radio galaxies, the angle between the jet and the light of sight is large. Almost all AGN detected at very high energy (VHE) (>100 GeV) are blazars with the exception of the three objects, Centaurus A (Cen A) [1,2], M87 and NGC 1275 which are radio galaxies [3,4]. The spectral energy distribution (SED) of these AGN have a double peak structure in the $\nu - \nu F_\nu$ plane. In the context of the leptonic model, the low energy peak corresponds to the synchrotron radiation from a population of relativistic electrons in the jet. Although the general consensus is that the high energy peak corresponds to the synchrotron self Compton (SSC) scattering of the high energy electrons with their self-produced synchrotron photons, this result remains inconclusive for various reasons [2]. However, this leptonic model is very successful in explaining the multi wavelength emission from blazars and FR I galaxies [1–4].

Although the SSC scenario seems to work very well to explain the SED of AGN up to the second peak [5,6], difficulties arise in explaining the multi-TeV emission detected in Cen A [7], flares from the radio galaxy M87 [8], the flares from blazars 1ES 1959 + 650 [9,10] and Markarian 421 (Mrk 421) [11]. Also the inevitable outcome of the leptonic scenario is that emission in multi-TeV energy has to be accompanied by a simultaneously enhanced emission in the synchrotron peak. Unfortunately the enhanced synchrotron emission was not observed in the flaring of 1ES 1959+650 in June 2002 [9] and also probably in the flaring of Mrk 421 in April 2004 [11], which implies that the SSC scenario may not be efficient enough to contribute in the multi-TeV regime.

To explain the orphan flaring of 1ES1959 + 650 a hadronic synchrotron mirror model was proposed by Böttcher [12]. In this model, the high energy protons from the jet interact with the primary synchrotron photons that have been reflected off clouds located at a few pc above the accretion disk. These photons are blue shifted in the jet frame so that there is a substantial decrease in the high energy protons to overcome the threshold for Δ-resonance. Similarly a structured leptonic jet model is proposed to explain the orphan TeV flare [13].

[a] e-mail: sarira@nucleares.unam.mx
[b] e-mail: luis.miranda@correo.nucleares.unam.mx
[c] e-mail: Subhash.Rajpoot@csulb.edu

Chapter 5

Appendix

5.1 SkyMaps

The tools and the steps for installing and learn to use this package is online in http://matplotlib.org/basemap. The next program is the code for plot a simple point in the celestial sphere and below is the corresponding figure.

```
# MY SKYMAP PROGRAM
from mpl_toolkits.basemap import Basemap
import numpy as np
import matplotlib.pyplot as plt
import matplotlib.pyplot as pl
#import pylab
#from mpl_toolkits.basemap import Basemap, pyproj,addcyclic
#from mpl_toolkits.basemap.pyproj import Geod
#import cartopy.crs as ccrs
#import PROJ4 as pr
# lon_0 is central longitude of projection.
# resolution = 'c' means use crude resolution coastlines.
m = Basemap(projection='hammer',celestial='None',lon_0=180.,resolution='h')
# draw parallels and meridians.
m.drawparallels(np.arange(-90.,90.,15.),linewidth=1.5,dashes=[1,0])
m.drawmeridians(np.arange(0,360.,30.),linewidth=1.5,dashes=[1,0])
#m.drawparallels(np.arange(-90.,90.,15.),labels=[True,False,False,True])
```

```
#m.drawmapboundary(fill_color='None')
#pl.text(0.,90,'h')
#fig=plt.figure(figsize=(8,4.5))
#ax = fig.add_axes([0.05,0.05,0.9,0.85])
#HBL'S
#1H:SHBLJ001355.9
#poly = map.tissot(180+3.46667,-18.8914, 10,70,color='cyan')
lon1, lat1 =3.46667,-18.8914
xpt1,ypt1 = m(lon1,lat1)
m.plot(xpt1,ypt1,'D',ms=10,color='#000080')
lon2, lat2 = lon1+40,lat1+1.
xpt2,ypt2 = m(lon2,lat2)
pl.text(xpt2,ypt2,'SHBLJ00135.9',fontsize=12,fontweight='bold',color='black')
plt.title("")
plt.show()
```

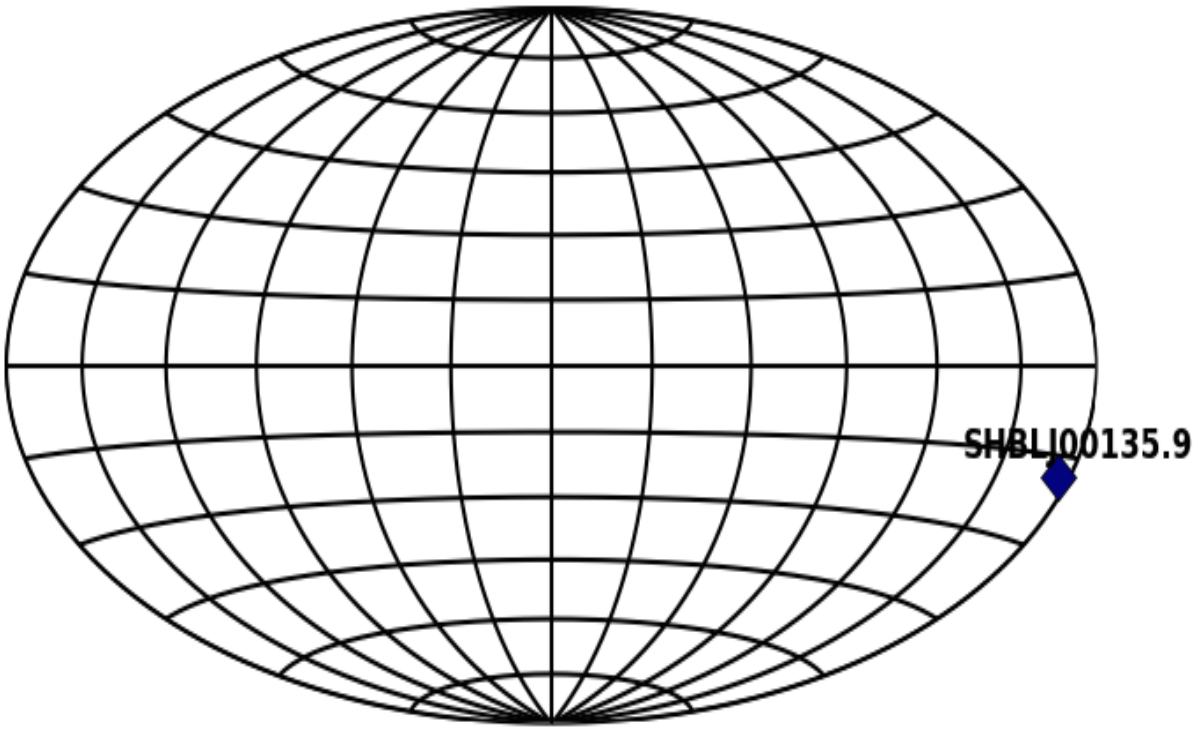

5.2 Program for Probability Density Functions

The probability density function for muon neutrino background was calculated using fortran 77 and the Newton-Cotes formula of integration for 10 points, applied to the event 37 considering also the prompt contribution. The code of the program is written below with the corresponding results.

```
CCCC PROGRAM TO GET THE PDFS
IMPLICIT DOUBLE PRECISION (A,B,C,F)
DIMENSION CC(2000),CP(2000)
DIMENSION CD(2000) ,BB(2000)
DIMENSION FF(2000)
OPEN(1,FILE='ev37back2.dat',STATUS='UNKNOWN')
OPEN(2,FILE='dev37back2.dat',STATUS='UNKNOWN')
31 FORMAT(1X,ES12.4,10X,ES12.4)
32 FORMAT(1X,ES12.4,10X,ES12.4,10X,ES12.4)
33 FORMAT(1X,A12,10X,A12,10X,A12)
CCC Points
n=43
do 1 j=1,n
CC(j)=10**(2.0+(j-1)*(1/6.))
1 continue
CCC Reference interval
fofo=CC(7)-CC(6)
CCC write(*,*)fofo

do 2 j=1,6
CP(j)=fintegration1(CC(j),CC(j+1))*
c(((CC(j+1)-CC(j))/fofo)**(-0.0))
2 continue

do 3 j=7,12
CP(j)=fintegration2(CC(j),CC(j+1))*
c(((CC(j+1)-CC(j))/fofo)**(-0.0))
```

```
3 continue
CCC ************************************

do 4 j=13,18
CP(j)=fintegration3(CC(j),CC(j+1))*
c(((CC(j+1)-CC(j))/fofo)**(-0.0))
4 continue

do 5 j=19,24
CP(j)=fintegration3(CC(j),CC(j+1))*
c(((CC(j+1)-CC(j))/fofo)**(-0.0))
5 continue

do 6 j=25,30
CP(j)=fintegration4(CC(j),CC(j+1))*
c(((CC(j+1)-CC(j))/fofo)**(-0.0))
6 continue

do 7 j=31,36
CP(j)=fintegration4(CC(j),CC(j+1))*
c(((CC(j+1)-CC(j))/fofo)**(-0.0))
7 continue

do 8 j=36,n-1
CP(j)=fintegration4(CC(j),CC(j+1))*
c(((CC(j+1)-CC(j))/fofo)**(-0.0))
8 continue

Ctot=0.0

do 9 j=1,n-1
Ctot=Ctot+CP(j)
9 continue
```

```
CCC write(*,*) Ctot

do 10 j=1,n-1
CD(j)=(CP(j)/Ctot)
Write(1,31) CC(j),CD(j)
Write(1,31) CC(j+1),CD(j)
10 continue

ccc=0.0
do 11 j=1,n-1
ccc=ccc+CD(j)
11 continue

write(1,*) ccc

Write(2,33) 'Emin(GeV)','Emax((GeV)',
c'Probability'

do 12 j=1,n-1
Write(2,32)CC(j),CC(j+1),CD(j)
12 continue
write(2,*) ccc

END



CCC FUNCTION integration **********************

Function fintegration1(A,B)

IMPLICIT DOUBLE PRECISION (F,X,Y,A,B)
DIMENSION X(40),Y(40)
```

```
CC C Numerical integration with 10 nodes

do 1 j=1,10
X(j)=((B-A)/9.)*(j-1)+A
1 continue

Y(1)=2857.
Y(2)=15741.
Y(3)=1080.
Y(4)=19344.
Y(5)=5778.
Y(6)=5778.
Y(7)=19344.
Y(8)=1080.
Y(9)=1574.
Y(10)=2857.
bob=(9./89600.)*((B-A)/9.)

Ala1=0.0

DO 2 j=1,10
Ala1=Ala1+(bob)*a1(X(j))*flux(X(j))*Y(j)
2 CONTINUE

fintegration1=Ala1

return
end

CCC ******************************************

Function fintegration2(A,B)

IMPLICIT DOUBLE PRECISION (F,X,Y,A,B)
```

```
DIMENSION X(40),Y(40)

CCCC Numerical integration with 10 nodes

do 1 j=1,10
X(j)=((B-A)/9.)*(j-1)+A
1 continue

Y(1)=2857.
Y(2)=15741.
Y(3)=1080.
Y(4)=19344.
Y(5)=5778.
Y(6)=5778.
Y(7)=19344.
Y(8)=1080.
Y(9)=15741.
Y(10)=2857.

bob=(9./89600.)*((B-A)/9.)

Ala2=0.0

DO 2 j=1,10
Ala2=Ala2+(bob)*a2(X(j))
c*flux(X(j))*Y(j)
2 CONTINUE

fintegration2=Ala2

return
end

CCC **********************************
```

```
Function fintegration3(A,B)

IMPLICIT DOUBLE PRECISION (F,X,Y,A,B)
DIMENSION X(40),Y(40)

CC C Numerical integration with 10 nodes

do 1 j=1,10
X(j)=((B-A)/9.)*(j-1)+A
1 continue

Y(1)=2857.
Y(2)=15741.
Y(3)=1080.
Y(4)=19344.
Y(5)=5778.
Y(6)=5778.
Y(7)=19344.
Y(8)=1080.
Y(9)=1574.
Y(10)=2857.

bob=(9./89600.)*((B-A)/9.)

Ala3=0.0

DO 2 j=1,10
Ala3=Ala3+(bob)*a3(X(j))*flux(X(j))*Y(j)
2 CONTINUE

fintegration3=Ala3

return
```

```
end

CCC ***********************************

Function fintegration4(A,B)

IMPLICIT DOUBLE PRECISION (F,X,Y,A,B)
DIMENSION X(40),Y(40)

CC C Numerical integration with 10 nodes

do 1 j=1,10
X(j)=((B-A)/9.)*(j-1)+A
1 continue

Y(1)=2857.
Y(2)=15741.
Y(3)=1080.
Y(4)=19344.
Y(5)=5778.
Y(6)=5778.
Y(7)=19344.
Y(8)=1080.
Y(9)=1574.
Y(10)=2857.

bob=(9./89600.)*((B-A)/9.)

Ala4=0.0

DO 2 j=1,10
Ala4=Ala4+(bob)*a4(X(j))*flux(X(j))*Y(j)
2 CONTINUE
```

```
fintegration4=Ala4

return
end

CCC ****************************************

CCCC Functions for the effective areas

Function a1(d)
implicit double precision (a,b,c,d,e)
a=1.0E-3
e=99.0
b=2.5
c=1E-3
a1=a*((d/e)**b)-c
return
end

CCC ****************************************

Function a2(d)
implicit double precision (a,b,c,d,e)
a=7.5E-5
e=1.0
b=1.29
c=0.225
a2=a*((d/e)**b)-c
return
end

CCC ****************************************

Function a3(d)
```

```
implicit double precision (a,b,c,d,e)
a=9.3E-3
e=0.01
b=0.59
c=21
a3=a*((d/e)**b)-c
return
end

CCC ****************************************

Function a4(d)
implicit double precision (a,b,c,d,e)
a=160
e=0.0001
b=0.11
c=1500
a4=a*((d/e)**b)-c
return
end

CCC ****************************************

CCCC Function for the flux for neutrino muons

Function flux(d)
implicit double precision (f,a,b,c,d,e)

Pi=3.141592654
bebe=cos((Pi/180)*(20.7))

flux=(d**(-2.7))*0.018*
c((1.0/(1.+(2.77*d*bebe/115.)))
c+((0.367)/(1+(1.18*d*bebe/850.)))
```

```
c+((1.4E-3)/(1+(0.14*d*bebe/5.0E7))))
return

end
```

5.2.1 Table of Results

The first and second columns are the minimum and maximum values of the energy range that we calculated for the background muon neutrino PDF . The last column is the value of the probability.

Emin(GeV)	Emax(GeV)	Probability
1.0000E+02	1.4678E+02	2.4565E-02
1.4678E+02	2.1544E+02	6.1756E-02
2.1544E+02	3.1623E+02	8.5433E-02
3.1623E+02	4.6416E+02	1.0309E-01
4.6416E+02	6.8129E+02	1.1750E-01
6.8129E+02	1.0000E+03	1.2920E-01
1.0000E+03	1.4678E+03	1.4832E-01
1.4678E+03	2.1544E+03	1.1475E-01
2.1544E+03	3.1623E+03	8.0097E-02
3.1623E+03	4.6416E+03	5.2691E-02
4.6416E+03	6.8129E+03	3.3417E-02
6.8129E+03	1.0000E+04	2.0724E-02
1.0000E+04	1.4678E+04	1.2368E-02
1.4678E+04	2.1544E+04	7.4479E-03
2.1544E+04	3.1623E+04	4.1000E-03
3.1623E+04	4.6416E+04	2.1619E-03
4.6416E+04	6.8129E+04	1.1197E-03
6.8129E+04	1.0000E+05	5.7919E-04
1.0000E+05	1.4678E+05	3.0296E-04
1.4678E+05	2.1544E+05	1.6176E-04
2.1544E+05	3.1623E+05	8.8715E-05

3.1623E+05	4.6416E+05	5.0129E-05
4.6416E+05	6.8129E+05	2.9178E-05
6.8129E+05	1.0000E+06	1.7447E-05
1.0000E+06	1.4678E+06	1.1396E-05
1.4678E+06	2.1544E+06	6.5153E-06
2.1544E+06	3.1623E+06	3.7275E-06
3.1623E+06	4.6416E+06	2.1311E-06
4.6416E+06	6.8129E+06	1.2156E-06
6.8129E+06	1.0000E+07	6.9078E-07
1.0000E+07	1.4678E+07	3.9050E-07
1.4678E+07	2.1544E+07	2.1924E-07
2.1544E+07	3.1623E+07	1.2200E-07
3.1623E+07	4.6416E+07	6.7128E-08
4.6416E+07	6.8129E+07	3.6401E-08
6.8129E+07	1.0000E+08	1.9375E-08
1.0000E+08	1.4678E+08	1.0075E-08
1.4678E+08	2.1544E+08	5.0917E-09
2.1544E+08	3.1623E+08	2.4890E-09
3.1623E+08	4.6416E+08	1.1728E-09
4.6416E+08	6.8129E+08	5.3190E-10
6.8129E+08	1.0000E+09	2.3247E-10

Bibliography

[1] V. F. Hess. Phy. Z. **13**, 1084(1912).

[2] J. J. Beatty and S. Westerhoff, Ann. Rev. Nucl. Part. Sci. **59**, 319 (2009). doi:10.1146/annurev.nucl.58.110707.171154

[3] G. T. Zatsepin and V. A. Kuzmin. Soviet J. Exp. Theor. Phys. **4**, 78(1966).

[4] T. K. Gaisser, "Cosmic rays and particle physics," Cambridge, UK: Univ. Pr. (1990).

[5] A. M. Hillas Ann. Rev. Astron. Astrophys. **22**, 425 (1984).

[6] Schmidt, M. *et al.* Modern Cosmology in Retro- spect, p. 347. Cambridge University Press, Cambridge (1990)

[7] G. Fossati, L. Maraschi, A. Celotti, A. Comastri and G. Ghisellini, Mon. Not. Roy. Astron. Soc. **299** (1998) 433 [arXiv:astro-ph/9804103].

[8] G. Ghisellini, A. Celotti, G. Fossati, L. Maraschi and A. Comastri, Mon. Not. Roy. Astron. Soc. **301**, 451 (1998); G. Fossati, L. Maraschi, A. Celotti, A. Comastri and G. Ghisellini, Mon. Not. Roy. Astron. Soc. **299**, 433 (1998); M. Chiaberge, A. Capetti and A. Celotti, Mon. Not. Roy. Astron. Soc. **324**, L33 (2001).

[9] A. A. Abdo *et al.* [Fermi LAT Collaboration], Astrophys. J. **719**, 1433-1444 (2010). [arXiv:1006.5463 [astro-ph.HE]].

[10] P. Roustazadeh and M. Böttcher, Astrophys. J. **728**, 134 (2011).

[11] https://icecube.wisc.edu

[12] J. F. Beacom, N. F. Bell, D. Hooper, S. Pakvasa and T. J. Weiler, Phys. Rev. D **68**, 093005 (2003)

[13] I. Frank and I. Tamm, Doklady Akad. Nauk SSSR, **14**, 107(1937).

[14] H. Krawczynski, S. B. Hughes, D. Horan, F. Aharonian, M. F. Aller, H. Aller, P. Boltwood and J. Buckley *et al.*, Astrophys. J. **601**, 151 (2004) [astro-ph/0310158].

[15] M. Blazejowski, G. Blaylock, I. H. Bond, S. M. Bradbury, J. H. Buckley, D. A. Carter-Lewis, O. Celik and P. Cogan *et al.*, Astrophys. J. **630**, 130 (2005) [astro-ph/0505325].

[16] A. M. Atoyan *et al.*, Astron. Astrophys. **383**, 864 (2002) doi:10.1051/0004-6361:20011732 [astro-ph/0112177].

[17] A. Reimer, M. Bottcher and S. Postnikov, Astrophys. J. **630**, 186 (2005) doi:10.1086/431948 [astro-ph/0505233].

[18] F. Halzen and D. Hooper, Astropart. Phys. **23**, 537 (2005) doi:10.1016/j.astropartphys.2005.03.007 [astro-ph/0502449].

[19] S. Adrian-Martinez, I. A. Samarai, A. Albert, M. Andre, M. Anghinolfi, G. Anton, S. Anvar and M. Ardid et al., arXiv:1111.3473 [astro-ph.HE].

[20] S. Sahu, A. F. O. Oliveros and J. C. Sanabria, Phys. Rev. D **87**, 103015 (2013) [arXiv:1305.4985 [hep-ph]].

[21] S. Sahu, B. Zhang and N. Fraija, Phys. Rev. D **85**, 043012 (2012).

[22] F. Aharonian *et al.* [HEGRA Collaboration], Astron. Astrophys. **406**, L9 (2003) [astro-ph/0305275].

[23] D. Giannios, D. A. Uzdensky and M. C. Begelman, Mon. Not. Roy. Astron. Soc. **395** (2009) L29 [arXiv:astro-ph/9807317]. arXiv:0901.1877 [astro-ph.HE].

[24] D. Giannios, D. A. Uzdensky and M. C. Begelman, Mon. Not. Roy. Astron. Soc. **402** (2010) 1649 arXiv:0907.5005 [astro-ph.HE].

[25] M. M. Reynoso, G. E. Romero and M. C. Medina, Astron. Astrophys. **545**, A125 (2012) [arXiv:1208.5284 [astro-ph.HE]].

[26] P. Desiati and T. K. Gaisser, Phys. Rev. Lett. **105**, 121102 (2010).

[27] Eadie, W. T., Drijard, D., James, F. E., Roos, M., and Sadoulet, B., Statistical Methods in Experimental Physics, Amsterdam: North-Holland, 1971.

[28] Kendall, M. G. and Stuart, A., The advanced Theory of Statistics, Charles Griffin and Co. Ltd, 1968.

[29] J. K. Becker, Phys. Rept. **458**, 173 (2008) doi:10.1016/j.physrep.2007.10.006 [arXiv:0710.1557 [astro-ph]].

[30] J. A. Aguilar [IceCube Collaboration], Nucl. Phys. Proc. Suppl. **237-238**, 250 (2013) doi:10.1016/j.nuclphysbps.2013.04.100 [arXiv:1301.6504 [astro-ph.HE]].

[31] M. G. Aartsen *et al.* [IceCube Collaboration], Phys. Rev. Lett. **111**, 021103 (2013).

[32] M. G. Aartsen *et al.* [IceCube Collaboration], Science **342**, 1242856 (2013).

[33] M. G. Aartsen *et al.* [IceCube Collaboration], Phys. Rev. Lett. **113**, 101101 (2014).

[34] E. Waxman and J. N. Bahcall, Phys. Rev. D **59**, 023002 (1999).

[35] S. Razzaque, Phys. Rev. D **88**, 081302 (2013); M. Ahlers and K. Murase, Phys. Rev. D **90**, 023010 (2014); C. Lunardini, S. Razzaque, K. T. Theodoseau and L. Yang, Phys. Rev. D **90**, 023016 (2014); A. M. Taylor, S. Gabici and F. Aharonian, Phys. Rev. D **89**, 103003 (2014).

[36] K. Murase and K. Ioka, Phys. Rev. Lett. **111**, no. 12, 121102 (2013); K. Murase, K. Ioka, S. Nagataki and T. Nakamura, Astrophys. J. **651**, L5 (2006);

[37] K. Murase, Y. Inoue and C. D. Dermer, Phys. Rev. D **90**, no. 2, 023007 (2014); C. D. Dermer, K. Murase and Y. Inoue, JHEAp **3-4**, 29 (2014); W. Winter, Phys. Rev. D **88**, 083007 (2013); F. W. Stecker, Phys. Rev. D **88**, no. 4, 047301 (2013).

[38] F. Krauß, M. Kadler, K. Mannheim, R. Schulz, J. Trüstedt, J. Wilms, R. Ojha and E. Ros *et al.*, Astron. Astrophys. **566**, L7 (2014); F. Tavecchio, G. Ghisellini and D. Guetta, arXiv:1407.0907 [astro-ph.HE].

[39] P. Padovani and E. Resconi, Mon. Not. Roy. Astron. Soc. **443**, 474 (2014).

[40] K. Murase, M. Ahlers and B. C. Lacki, Phys. Rev. D **88**, no. 12, 121301 (2013); X. C. Chang and X. Y. Wang, Astrophys. J. **793**, no. 2, 131 (2014).

[41] A. Neronov, D. V. Semikoz and C. Tchernin, Phys. Rev. D **89**, 103002 (2014).

[42] L. A. Anchordoqui, V. Barger, I. Cholis, H. Goldberg, D. Hooper, A. Kusenko, J. G. Learned and D. Marfatia *et al.*, Journal of High Energy Astrophysics **1-2**, 1 (2014).

[43] C. Y. Chen, P. S. B. Dev and A. Soni, Phys. Rev. D **89**, 033012 (2014); K. Murase and J. F. Beacom, JCAP **1210**, 043 (2012); A. Esmaili and P. D. Serpico, JCAP **1311**, 054 (2013); A. Esmaili and Y. Farzan, JCAP **1212**, 014 (2012); P. Baerwald, M. Bustamante and W. Winter, JCAP **1210**, 020 (2012); S. Pakvasa, A. Joshipura and S. Mohanty, Phys. Rev. Lett. **110**, 171802 (2013).

[44] S. Sahu and L. S. Miranda, Eur. Phys. J. C **75**, no. 6, 273 (2015).

[45] C. D. Dermer and R. Schlickeiser, Astrophys. J. **416**, 458 (1993).

[46] M. Kachelriess, S. Ostapchenko and R. Tomas, New J. Phys. **11**, 065017 (2009); M. Honda, Astrophys. J. **706**, 1517 (2009).

[47] See the website: http://tevcat.uchicago.edu/.

[48] S. Adrian-Martinez *et al.* [ANTARES Collaboration], JCAP **1512**, no. 12, 014 (2015) doi:10.1088/1475-7516/2015/12/014 [arXiv:1506.07354 [astro-ph.HE]].

[49] M. Punch, C. W. Akerlof, M. F. Cawley, M. Chantell, D. J. Fegan, S. Fennell, J. A. Gaidos and J. Hagan *et al.*, Nature **358**, 477 (1992).

[50] A. A. Abdo *et al.* [MAGIC Collaboration], Astrophys. J. **736**, 131 (2011).

[51] R. Moharana and S. Razzaque, JCAP **1508**, no. 08, 014 (2015).

[52] F. Aharonian [HESS Collaboration], Astron. Astrophys. **481** , L103 (2008).

[53] J. Albert *et al.* [MAGIC Collaboration], Astrophys. J. **667**, L21 (2007).

[54] F. Aharonian *et al.* [H.E.S.S. Collaboration], Astron. Astrophys. **455**, 461 (2006).

[55] A. Abramowski *et al.* [HESS Collaboration], Astron. Astrophys. **554**, A72 (2013).

[56] A. Abramowski *et al.* [H.E.S.S. Collaboration], Astron. Astrophys. **533**, A110 (2011).

[57] J. Aleksic *et al.* [MAGIC Collaboration], Astrophys. J. **748**, 46 (2012).

[58] R. U. Abbasi *et al.* [Telescope Array Collaboration], Astrophys. J. **790**, L21 (2014).

[59] K. Fang, T. Fujii, T. Linden and A. V. Olinto, Astrophys. J. **794**, 126 (2014).

[60] The Pierre Auger Collaboration, Science **318**, 938 (2007).

[61] A. Abramowski *et al.* [HESS Collaboration], arXiv:1306.3186 [astro-ph.HE].

[62] S. Sahu, L. S. Miranda and S. Rajpoot, arXiv:1501.00973 [astro-ph.HE].

[63] S. Sahu and E. Palacios, Eur. Phys. J. C **75**, no. 2, 52 (2015) [arXiv:1310.1381 [astro-ph.HE]].

[64] L. Costamante and G. Ghisellini, Astron. Astrophys. **384**, 56 (2002) [astro-ph/0112201].

[65] K. Katarzynski, Astron. Astrophys. **537**, A47 (2012) [arXiv:1110.5993 [astro-ph.CO]].

[66] V. A. Acciari, E. Aliu, T. Arlen, T. Aune, M. Bautista, M. Beilicke, W. Benbow and M. Bottcher *et al.*, Astrophys. J. **715**, L49 (2010) [arXiv:1005.0041 [astro-ph.HE]].

[67] L. S. Miranda, A. R. de León and S. Sahu, Eur. Phys. J. C **76**, no. 7, 402 (2016) doi:10.1140/epjc/s10052-016-4247-x [arXiv:1510.00048 [astro-ph.HE]].

[68] F. James, "Statistical methods in experimental physics," Hackensack, USA: World Scientific (2006) 345 p.

[69] J. Braun, J. Dumm, F. De Palma, C. Finley, A. Karle and T. Montaruli, Astropart. Phys. **29**, 299 (2008).

[70] R. Enberg, M. H. Reno and I. Sarcevic, Phys. Rev. D **79**, 053006 (2009).

[71] T. Neunhoffer, Astropart. Phys. **25**, 220 (2006).

[72] M. Dutka, PhD Thesis, Publication Number: AAT 3626575; ISBN: 9781321015799.

[73] F. Tavecchio *et al.*, Astrophys. J. **575**, 137 (2002).

[74] G. Ghisellini, F. Tavecchio, L. Foschini, G. Bonnoli and G. Tagliaferri, Mon. Not. Roy. Astron. Soc. **432**, 66 (2013).

[75] O. Hervet, C. Boisson and H. Sol, arXiv:1605.02272 [astro-ph.HE].

[76] G. Ghisellini and F. Tavecchio, Mon. Not. Roy. Astron. Soc. **448**, no. 2, 1060 (2015).

[77] T. Savolainen, D. C. Homan, T. Hovatta, M. Kadler, Y. Y. Kovalev, M. L. Lister, E. Ros and J. A. Zensus, Astron. Astrophys. **512**, A24 (2010).

[78] J. D. Finke, S. Razzaque and C. D. Dermer, Astrophys. J. **712**, 238 (2010) [arXiv:0905.1115 [astro-ph.HE]].

[79] A. Dominguez, J. R. Primack, D. J. Rosario, F. Prada, R. C. Gilmore, S. M. Faber, D. C. Koo and R. S. Somerville *et al.*, Mon. Not. Roy. Astron. Soc. **410**, 2556 (2011) [arXiv:1007.1459 [astro-ph.CO]].

[80] Y. Inoue, S. Inoue, M. A. R. Kobayashi, R. Makiya, Y. Niino and T. Totani, Astrophys. J. **768**, 197 (2013) [arXiv:1212.1683 [astro-ph.CO]].

[81] B. Bartoli *et al.* [ARGO-YBJ Collaboration], Astrophys. J. **758**, 2 (2012) [arXiv:1209.0534 [astro-ph.HE]].